The NeuroDisc: A Wireless Neural Recorder Leveraging Ultra-Low-Power Backscatter Communication

James D. Rosenthal

A dissertation
submitted in partial fulfillment of the
requirements for the degree of

Doctor of Philosophy

University of Washington

2021

Reading Committee:

Matthew S. Reynolds, Chair

Joshua R. Smith

Chet T. Moritz

Program Authorized to Offer Degree:
Electrical & Computer Engineering

University of Washington

Abstract

The NeuroDisc: A Wireless Neural Recorder Leveraging Ultra-Low-Power Backscatter Communication

James D. Rosenthal

Chair of the Supervisory Committee:
Professor Matthew S. Reynolds
Department of Electrical & Computer Engineering

Minimally-invasive tools for researching and treating neural disorders increasingly rely on high data rate, ultra-low-power wireless communication. This dissertation explores the use of backscatter communication to reduce the power consumption of wireless uplinks streaming high resolution neural telemetry. We present the development of the NeuroDisc, a custom wireless neural recorder leveraging a wireless backscatter uplink to obtain data rates of tens of megabits per second (Mbps) at orders of magnitude lower power consumption compared to commercially available alternatives, such as WiFi and Bluetooth. The design, analysis, and experimental validation of three different modulation techniques for backscatter communication are reported: (1) a 25 Mbps, 12.4 pJ/bit differential quadrature phase-shift keying (DQPSK) backscatter uplink for high rate telemetry; (2) a 1.0 Mbps, 198 pJ/bit Bluetooth Low Energy-compatible single sideband (SSB) frequency-shift keying (FSK) uplink for compatibility with off-the-shelf Bluetooth devices such as smartphones and tablets; and (3) a 1.25 Mbps, 160 pJ/bit all-digital orthogonal frequency division multiplexing (OFDM) backscatter uplink with the potential to improve reliability in multipath environments. Using the 25 Mbps DQPSK backscatter uplink, we validate the end-to-end system through *in vivo* neural recordings from the primary motor cortex of an anesthetized pigtail macaque. In the context of wirelessly recording from non-human primates (NHP) using the NeuroDisc, we investigate the dense multipath interference exhibited in a standard metal NHP cage and propose a novel method using digitally-controlled mode stirring to improve the *in situ* reliability of low-power wireless communication. These developments advance the state-of-the-art in low power wireless communication and lay the ground work for future innovation in ultra-miniaturized, battery-free prosthetics for bioelectronic medicine.

TABLE OF CONTENTS

LIST OF FIGURES

LIST OF TABLES

DEDICATION

To Sally and Oma.

ACKNOWLEDGMENTS

Outdoor adventures are often rated using the fun scale wherein three types of fun exist. An activity that is *Type I Fun* is fun the entire time, like hanging out with friends, skiing at a resort on a powder day, or plugging in a circuit and having it work the first time. Progressing to *Type II Fun*, an activity begins to lack any feeling of joy in the moment. However, after the activity has passed, you may look back fondly and even say "that was not so bad!." Examples include slogging through miles of trail to reach a gorgeous sunset, running a marathon, or spending long nights debugging a circuit and finally having it work. The last step on the scale, *Type III Fun*, is actually not fun at all, like enduring a heavy thunderstorm midway in the mountains, spending hours bushwacking through dense brush with lots of ticks and never finding your intended trail, or getting grilled by a professor during a presentation. Even in retrospect, your palms might still get sweaty thinking about the experience. An important lesson for me in graduate school was that the people around me are arguably the biggest factor in determining where an adventure will fall on the fun scale. I owe a huge *thank you* to my friends and colleagues who heavily skewed my experience in the Ph.D. program towards *Type I*.

First and foremost, I would like to thank my advisor, Professor Matt Reynolds. Throughout my Ph.D. I was well-supported, with access to world-class equipment, mentorship, and opportunities. I will always be grateful for our discussions that provided me a broader context for the technical and societal impacts of my research. It has been a pleasure to work with a researcher who is so knowledgeable, passionate, and kind. I sincerely hope this will not be our last opportunity to collaborate.

For helping to improve my research, I would like to thank my dissertation committee, Professors Chet Moritz, Joshua Smith, Eb Fetz, and Greg Durgin. Your work has inspired me throughout my Ph.D., and I am extremely grateful for your critical feedback and mentorship throughout the Ph.D. program.

Behind each page of this dissertation are dozens of hours of designing, building, breaking, debugging, analyzing, writing, and rewriting. I could not have completed that work without the tremendous mentorship, support, and inspiration of my lab mates and friends. Thank you so much Eleftherios Kampianakis, Apoorva Sharma, Alex Hoang, Xiaojie Fu, Andreas Pedroß-Engel, Claire Watts, Tyler Petrie, Sara Reyes, Anissa Dadkhah, Alexandra Pike, Thang Phu, and Tanya Ipek. Thank you as well to friends and collaborators in the ECE department: Hashem Mohammed, Momona Yamagami, Mareldi Ahumada, Jordan Drew, Bora Banjanin, Greg Moore, Laura Arjona, Anand Sekar, and many others. I am grateful for the fresh perspectives offered as well by friends and mentors outside of ECE, including

Professor Afroditi Psarra, Professor Thomas Deuel, James Wenlock, Gabrielle Benabdallah, and Matt Busch. Thank you Andrew, Sarah, Conor, Barbara, Billy, Ryan, Michael, Lulu, Jenny, and Semy for all the laughs. Thank you Charlie and Taylor for consistently showing up–who knew it was possible to actually make friends at orientation?

Connecting with younger students in the community through teaching and outreach provided me significant inspiration through my Ph.D. The students excitement, curiosity, and creativity for STEM forced me to dive deeper into my technical field and think critically about how researchers can contribute to their community. Thank you to Professor Scott Hauck, Professor Tamara Bonaci, Professor Matt Reynolds, Dr. David Wolczyk, and Penny Hinke for the teaching opportunities, and to the many dozens of students who put up with me. I am grateful as well to the UW College of Engineering, Professor Denise Wilson, Professor Eve Riskin, the UW STARS Program, and UW STEM Upward Bound for the unique outreach opportunities and the tremendous service they provide to our community.

Completing the graduate program would not have been possible without the support of the UW ECE program and its staff. Thank you to everyone who has contributed to the department, with a special thanks to Brenda Larson.

Lastly, thank you to my family, Noor, and Coda. Any day spent with you is *Type I*.

Chapter 1

INTRODUCTION

1.1 Dissertation Overview

The U.S. National Academy of Engineering (NAE) and the American Institute for Biological and Medical Engineering have identified the development of personalized, networked healthcare as a critical goal for improving equity in the United States [1]. Of the many types of disorders that could benefit from personalized medicine, neurological disorders are of particular interest given the essential role of the nervous system in movement and cognition. With many unknowns remaining about both healthy and pathological states in the nervous system, the NAE emphasized *reverse engineering the brain* as a key step towards achieving this goal. Developing translational medical therapies for neural disorders could have a profound impact on improving economic and social opportunity for all people, but doing so will require the seamless integration of devices with the brain.

Emerging bioelectronic medical devices, such as the brain-computer interfaces (BCIs) shown conceptually in Fig. 1.1a, provide new treatment options for sensorimotor and cognitive disorders. By measuring neural signals in the brain and/or spinal cord, these systems can analyze patterns in the dynamics of neuronal activity and generate control signals for therapeutic or assistive devices to improve quality of life (Fig. 1.2). For example, early clinical trials on spinal cord stimulation have partly restored motor function after spinal cord injury [4, 5], and deep brain stimulators have helped alleviate symptoms from obsessive compulsive disorder [6]. Despite these successes, the electrophysiological mechanisms behind the treatments remain poorly understood. Current bioelectronic devices remain invasive and unwieldy, creating a barrier to real-time, closed-loop monitoring of the electrophysiological markers involved in the stabilization and regeneration of neural pathways. This gap has led prominent funding bodies like the European Commission [7] and the U.S. Defense Advanced Research Projects Agency (DARPA) [8] to call for new devices that can aid in seamlessly diagnosing and monitoring brain function.

For neurotechnology to be integrated with the brain, the size, weight, and power (SWaP) of the electronics must be minimized. Neural recording systems are currently limited by their biocompatibility with surrounding tissue and their severely constrained power budgets, which must allocate adequate power for complex functionality while remaining on the order of milliwatts or less to avoid damaging tissue [9, 10]. As a result of these challenges, current real-time neural prosthetics typically operate with tethered instrumentation in systematically constrained environments [3, 11] (Fig. 1.2). Tethered interfaces facilitate the transfer of power and data to external systems that can decode the neural

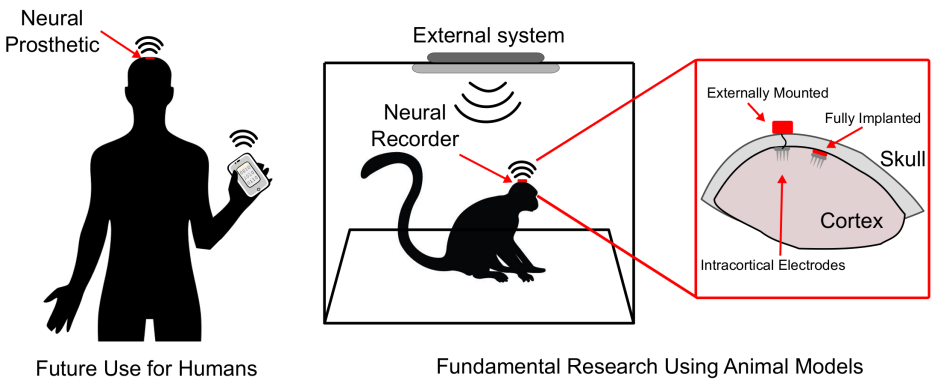

(a)

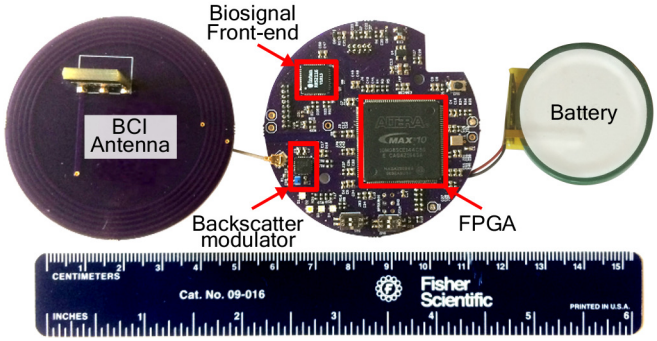

(b)

Figure 1.1: (a) Depiction of wireless neural recording applications for healthcare in humans (left) and fundamental neuroscience research in animal models (right). (b) We developed the NeuroDisc as a wireless neural recorder for use with non-human primates. The system was designed as an externally mounted neural recorder, though the results from this research are applicable to future implantable, battery-free wireless neural recorders.

signals to study brain dynamics, actuate external prostheses, and/or deliver neural stimulation. However, tethers also reduce mobility, increase the risk of infection, and can produce misleading correlations in the recorded data [12]. Wireless power transfer (WPT) and wireless data uplinks obviate the needs for tethers, but the high power consumption of conventional wireless electronics (e.g. WiFi) renders them incompatible with implant SWaP requirements. As a result, state-of-the-art systems have heretofore been limited by shorter operational durations, reduced uplink throughput [13], or elimination of a real-time wireless uplink [12].

Wireless communication is ubiquitous this day in age, yet implementing high rate wireless communication within the constraints of a neural prosthetic remains challenging. Why is current wireless technology insufficient? The primary issue is that modern wireless gadgets, like smartphones and laptops, are designed under drastically different size, weight, and power (SWaP) constraints than neurotechnology. Smartphones, for example, are required to transmit

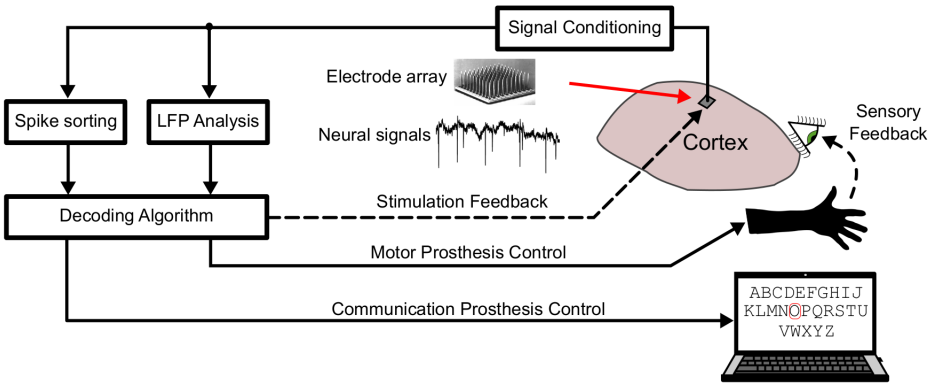

(a)

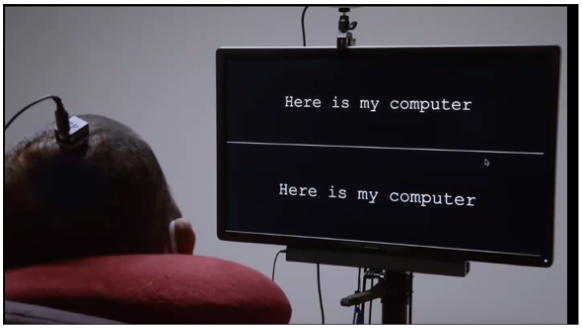

(b)

Figure 1.2: Brain-computer interfaces (BCIs) measure and process neural signals: (a) Generalized architecture for neural prosthetics (adapted from [2]). (b) BCI enabling a patient with locked-in syndrome to write sentences based on neural activity [3].

cellular data, connect to WiFi, and perform complex processing for 8-10 hours before they are recharged and set aside for the night. To carry out these functions, phones can be on the order of 100 cm^3 while carrying a nearly 7 Watt-hour battery that occupies nearly two-thirds of the phone's volume. In contrast, an implanted neural prosthetic providing stimulation for induced plasticity would need to be on the order of 1 cm^3 and stream comparable amounts of data non-stop, day and night, ideally for multiple days or weeks. The size and weight of the implant must be minimized to reduce a patient's foreign body response, and the power consumption must be kept to $<$10 mW/cm^2 to reduce the risk of damaging nearby tissues [14, 15]. Even in the multi-billion dollar industry of cellphones, where SWaP is critical, the circuit chips for WiFi and LTE radios are still on the order of 1 cm^2 in area and consume nearly 1 W of power each, drastically exceeding the safe SWaP and thermal envelope.

Backscatter communication provides an alternative to the high power consumption and large size of conventional wireless uplinks. Backscatter radios offer megabit per second (Mbps) data rates while consuming microwatts of power,

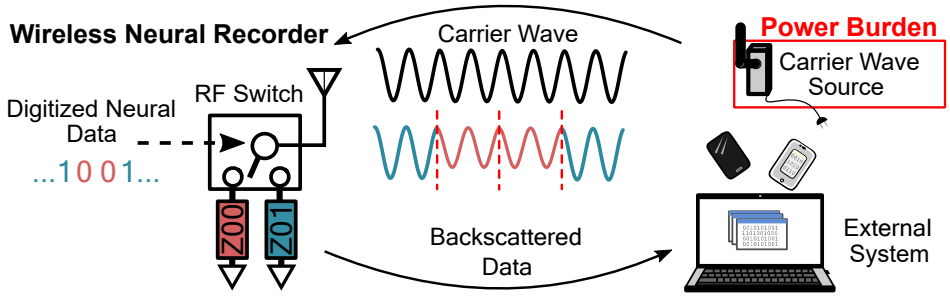

Figure 1.3: Overview of backscatter communication. The power burden of carrier wave generation and amplification is removed from the energy-constrained neural recording device.

yielding per-bit energy efficiencies on the order of pJ/bit, a 50-1000X improvement versus conventional radios [16]. Backscatter communication achieves significant energy savings by reflecting an externally generated radio frequency (RF) carrier wave carrier wave rather than generating the RF carrier wave locally. The power-hungry RF carrier wave generator and RF amplifier can thus be removed from the energy constrained device, as shown in Fig. 1.3, and instead allocated to an external system with a less constrained power budget. By changing the impedance presented to its antenna, for example using an RF switch, a backscatter-based device can deliberately reflect electromagnetic waves while modulating their amplitude and phase. These reflected waves can then be received and decoded using conventional radio technology.

The energy savings of backscatter communication have enabled novel wireless sensing modalities for energy-constrained applications. For example, backscatter communication has been used to telemeter neural data from dragonflies in flight using a battery-free neural recorder [17] and to enable a battery-free wireless camera [18]. These benefits make backscatter communication an appealing choice for research and clinical applications.

In this dissertation, we demonstrate how energy efficient backscatter communication can be designed for high rate wireless neural recorders. We present the *NeuroDisc* wireless neural recorder (Fig. 1.1b) that can measure up to 16 channels of high resolution neural signals *in vivo* while continually streaming samples at 25 Mbps and 12.4 pJ/bit with backscatter communication. For deployment in freely-moving non-human primate (NHP) experiments, we provide measurements of the channel transfer function (CTF) within a metal NHP home cage and demonstrate uplink viability across the 915 MHz and 2.4 GHz industrial, scientific, and medical (ISM) bands. In order to overcome multipath in the CTF that could lead to data drops, we demonstrate two novel mitigation techniques: (1) electronic mode stirring using parasitic antenna arrays within the cage, and (2) fully-digital orthogonal frequency domain multiplexing (OFDM) modulation for backscatter communication.

1.2 Neural Prosthetic Technologies

Portions of this section have been adapted from the author's written contributions to [16, 19]

Neural prosthetics have emerged thanks to decades of advancements in methods for *in vitro* and *in vivo* neural recording. Several methods for neural recording have emerged due to the complex anatomy and functioning of the brain. Examples of neural measurement techniques include electrophysiological recording to measure electrical signals generated by neurons [20], two-photon microscopy to measure cellular structures labelled with fluorescent proteins [21], and functional magnetic resonance imaging (f-MRI) to measure blood flow throughout the brain [22]. Each measurement technique has trade-offs in spatial resolution, temporal resolution, invasiveness, and portability [23]. Electrophysiological recording is a promising method for neural prosthetics given its very high temporal and spatial resolution. Furthermore, thanks to existing industrial processes for manufacturing silicon devices, electrophysiological recording lends itself to miniaturization, high volume manufacturing, and low cost.

Within the modality of electrophysiological recording, several measurement techniques exist with varying degrees of accuracy and invasiveness. These techniques focus on measuring the electric fields generated by ionic channels in neurons during action potentials (APs) or "spikes." By placing a conductive probe within or near a neuron and measuring the potential relative to a reference electrode, high fidelity signals representing neural activity can be obtained. Alternatively, the electric field from groups of neurons, known as neural ensemble activity, is strong enough that it can also be measured by electrodes on the surface of the brain (electrocorticogrpahy or ECoG) or on the surface of the scalp (electroencephalography or EEG). Generally the spatial resolution is commensurate to the invasiveness of the technique, with intracortical and ECoG electrodes providing high resolution but requiring invasive surgery and EEG providing lower resolution without the need for surgical implantation.

By measuring the temporal and spectral electrical activity of neurons, electrophysiological recordings have improved our understanding of neuronal dynamics [20]. Using this information, engineers and neuroscientists have been able to relate the rate at which neurons activate–known as the firing rate–to intended limb movement parameters [3, 11, 12, 24–26], enabling the development brain-computer interfaces (BCIs) that operate prostheses based on neuronal firing rates and neural ensemble activity, as shown in Fig. 1.2. These BCIs can provide assistance to people with sensorimotor disorders like paralysis [27, 28], Parkinson's [29], ALS [3], as well as cognitive disorders like obsessive compulsive disorder (OCD) [6]. Improving the performance of such devices has thus become an active area of research in academia and industry [30].

In order to measure neural dynamics with high temporal and spatial resolution, neural interfaces need to transmit large volumes of data. A complete axion potential typically lasts 1 msec, and in order to measure the complete depolarization and repolarization dynamics, sample rates ≥ 20 kHz per neural channel are needed. When measured outside of a neuron, the AP amplitudes can be on the order of 10's of μVolts, typically requiring analog-to-digital converter

(ADC) resolutions $\geq$10 bits, e.g. [31]. While theoretically the firing rate of a single neuron could be used to control a one-dimensional BCI (e.g. volume of a computer), multiple neurons are required to control higher complexity systems, like robotic arms. Recording from multiple sites in the brain is also advantageous for fundamental neuroscience to analyze how different areas of the brain exchange information.

Recording neural activity with high temporal and spatial resolution generates significant volumes of data. If we consider collecting 32 channels of neural data with 16-bit voltage resolution and a sampling rate of 20 kSamples/sec (kSps) per channel, the total data volume is more than 10 Mbits of biological data per second. This number easily grows to more than 20 Mbits/sec (Mbps) with the addition of data packet structure, error correction coding, and housekeeping information such as timestamps. Data compression techniques can be used to reduce the required data rate, however, the required algorithms pose additional constraints in computational time and power consumption.

Since it is difficult to achieve wireless data rates $>$2 Mbps using commercial off-the-shelf electronics while remaining within the necessary SWaP envelope, electrophysiology experiments often rely on controlled, cabled test environments where a subject's movements are constrained. Systematic control of the test environment reduces noise in neural recordings, enables precise measurement of the behavioral tasks, and prevents injury to the person or animal and damage to the wired equipment. There are several drawbacks to cabled setups, however. Firstly cables are a vector for infection for surrounding tissue. The cabling must pass through the skin and the protective dura mater of the brain, leaving the subject vulnerable to bacterial infections. Secondly, the cabling requires mechanical stabilization to avoid injuring the subject and damaging the measurement equipment. Mechanical stabilization is often achieved by restricting the subject's movement, which causes stress and discomfort for the subject. Under these conditions, a subject can only be expected to perform tasks for a limited amount of time before physical and mental fatigue degrade their performance. Additionally, restricting motor function has been found to affect the quality of the measured neural data. Unnatural correlations between motor parameters and neural signals, referred to as stereotypes, have been observed during constrained experiments [12], making it difficult to generalize findings. Ultimately, humans and animals live and thrive in a natural and freely moving state. In order to develop an unbiased understanding of how neural activity gives rise to high-level functionality over long durations, neural recording must be performed wirelessly.

To reduce the effects of tethers, dozens of wireless BCIs have been developed for wireless neural recording in free-moving animals, e.g. [32–35] as recent examples of the state-of-the-art. Researchers at the University of Washington in [32] developed a wireless BCI called the NeuroChip-2 for recording and stimulation in NHPs. While this device can be used for neural recording experiments of nearly 48 hours duration, the potential for recording neural data for $>$48 hours is limited because data must be saved locally to an SD card; there is no high-rate wireless uplink to offload data, so once the memory is full, the experiment must be terminated. Further, SD cards require more than 600 mW of power during write and read operations [36], which can easily dominate the power budget of the BCI, and their size and user interface restrict prohibit their use in fully implantable devices. Other wireless BCIs use WiFi [37],

BLE [35], or custom wireless protocols on integrated circuits [33] to uplink data, but the power budget of these BCIs is still dominated by the communication system. These conventional radios have undesirably high power consumption, which leads to poor battery life and the potential for tissue heating due to the combination of DC power dissipation and high specific absorption rates (SAR) [38, 39].

1.3 Wireless Backscatter Communication for High-Rate, Energy-Efficient Telemetry

Energy efficient, high data rate wireless backscatter communication could solve the complex SWaP tradeoffs of neural recorders. These uplinks could provide the data to an external, non-power-constrained computing device to analyze the recorded neural activity, as shown in Fig. 1.1a. For the case of bi-directional BCIs that provide neural recording and neural stimulation, such an external device could also determine a stimulation response using signal processing techniques that are infeasible on a size- and power-constrained neural recording device [15].

Backscatter communication obtains its energy efficiency by redistributing power-hungry elements in a wireless link to a power-rich external system. Unlike conventional radios, backscatter-based uplinks do not require RF amplifiers and oscillators to generate a communication carrier wave. The carrier wave is instead provided by an external transceiver having access to e.g. mains power or a large external battery. As shown in Fig 1.3, a backscatter-based device can communicate data by applying a time-varying impedance to its antenna, which modulates the amplitude and phase of the incident carrier wave. In this case, the backscatter-based device only needs to provide enough power to actuate an RF switch or transistor, which is typically consumes microwatts rather than milliwatts. The modulated signal is then scattered by the device's antenna and received by an external system that could be a custom receiver or a commodity device, depending on the frequencies used, the modulation scheme, and the protocol. This modality allows for small-form factor systems with high data rates (>96 Mbps) [40] at orders of magnitude lower power consumption compared to BLE and WiFi (IEEE 802.11n) [41]. Technology such as ultra-wide band (UWB) radio [42] is a potential alternative to backscatter communication, but backscatter communication is an attractive choice for BCIs due to its simplicity and lower overall power consumption compared with UWB and other alternatives. Furthermore, backscatter has the potential for compatibility with existing protocols like WiFi and Bluetooth, reducing the overall cost and complexity of the system.

The improved energy efficiency of backscatter communication comes at the cost of a less favorable link budget compared to conventional radios. Because the externally-generated carrier wave travels a round trip from the external system to the backscatter radio and back, the RF path loss changes as $1/r^4$ for a backscatter system, rather than the usual $1/r^2$ for conventional radios, where r is the free-space distance between the external system and the BCI antenna [43, 44]. Given the round-trip nature of the backscatter link budget, multipath interference can significantly reduce the reliability of backscatter radios. For experiments conducted inside the cage of a freely moving animal, the multipath environment could result in dropped data. Careful attention to the communication channel and the link

budget design are therefore required to ensure reliable communication.

1.4 The NeuroDisc Wireless Neural Recorder

In this dissertation, we present the development of the *NeuroDisc* wireless neural recorder, which leverages a backscatter communication uplink to attain high data rates while expending orders of magnitude lower power consumption relative to commercial wireless standards. The NeuroDisc uniquely synthesizes previous advancements in low-power backscatter communication and biological sensing to reduce the power burden of wireless uplinks on neural recorders.

What differentiates the NeuroDisc from other wireless neural recorders is an FGPA-based reconfigurable backscatter uplink that enables the use of several different ultra-low-power communication modes from a single hardware platform: a 25 Mbps differential quadrature phase-shift keying (DQPSK) uplink using a custom protocol [16] can transmit large volumes of data, as needed for broadband neural recording; a single-sideband (SSB) BLE compatible frequency-shift keying (FSK) uplink [45, 46] that facilitates integration of the NeuroDisc with existing wireless infrastructure; and an orthogonal frequency division multiplex (OFDM) backscatter uplink [47] that enables greater resilience to multipath fading observed in animal cage environments. To measure neural signals, the NeuroDisc uses a low-power Intan RHS2116 electrophysiology interface that can sample 16 channels at 20 kSps with 16-bit resolution, allowing recording and uplink of low frequency local field potentials and high frequency neural spikes [48]. The RHS2116 also provides stimulation capability, enabling the NeuroDisc to eventually be used for both neural recording and stimulation experiments. A comparison of state-of-the-art neural recorders including the NeuroDisc is shown in Table 1.1 and a comparison of wireless uplink efficiencies between backscatter and conventional wireless devices in Fig. 1.4.

1.5 Dissertation Organization

The remainder of this dissertation is organized as follows: Chapter 2 is adapted from [16] and presents the development and validation of a 25 Mbps, 12.4 pJ/bit DQPSK uplink for the NeuroDisc that enables measurement of broadband neural data, including low frequency local field potentials and high frequency neural spikes. Chapter 3 is adapted from [46] and presents the analysis and development of a 1.0 Mbps, 198 pJ/bit BLE compatible SSB modulation uplink for the NeuroDisc, enabling compatibility between the NeuroDisc and unmodified BLE devices like smartphones and tablets. Included are analyses of how SSB backscatter modulation is affected by the non-idealities, e.g. component tolerance, in a design. Chapter 5 is adapted from [53] and provides the results of channel transfer function measurements and backscatter system performance tests in the 2.4 GHz ISM bands. The multipath interference observed by these measurements could disrupt communication from the NeuroDisc. We discuss two main techniques for mitigating this interference by modifying the environment with mode-stirring in Chapter 6, and by developing OFDM backscatter modulation in Chapter 7. Chapter 8 presents conclusions from this dissertation and identifies future areas of research for maturing and deploying wireless neural recorders with backscatter communication.

Table 1.1: Comparison of state-of-the-art wireless neural recorders

	Yin et al., 2014 [33]	*Schwarz et al., 2014 [49]*	*Muller et al., 2015 [34]*	*Ando et al., 2016 [50]*	*Teng et al., 2017 [51]*	*Xu et al., 2018 [52]*	*This work, NeuroDisc [16, 46, 47]*
Test Subject	NHP	NHP	Rat	Humans	-[a]	Rat	**NHP**
Custom ASIC	✓	✗	✓	✓	✓	✓	✗
BCI Size (mm)	52 x 44 x 30	-[a]	6.4 x 6.4 x 0.7 (IC)	53 x 31 x 47 (Transmitter)	1 x 1 (IC)	2.5 x 5.3 (IC)	**63 x 63 x 30**
ADC (bits)	12	12	15	12	-[a]	12	**16**
No. of Channels	100	512	64	4096	8	12	**Up to 16**
Sampling (kSps)	20	31	1	1	-[a]	40	**Up to 20**
Stimulation Capability	No	No	No	No	No	No	**Yes**
RF Comms Type	Active RF	Active RF	ASK Backscatter	Active RF	Active RF	Active RF	**DQPSK, SSB FSK, or OFDM Backscatter**
RF Comms Band	3.5 GHz	2.4 GHz	300 MHz	9 GHz	403 MHz	2.4 GHz	**915 MHz & 2.4 GHz**
Wireless Data Rate (Mbps)	48	1.33	1	128	8	10	**Up to 25**
Uplink Distance (m)	5	10	0.013	5	-[a]	-[a]	**Up to 6**[c]
Analog Comms Power (mW)	>30[a]	33.9[b]	0.0024	561	5.6	396	**≤0.309**[d]
Analog Comms Energy Efficiency (pJ/bit)	>180 (high-rate mode) - 750 (low rate mode)[a]	25,488	2.4	4383	700	39,600	**12.4-198**[e]

[a]Exact value not reported. [b]TX power consumption of the nRF24L01+ at 0 dBm transmit power.

[c]SSB FSK modulation at 1 Mbps data rate in the 2.4 GHz ISM band.

[d] Measured static+dynamic power of the backscatter modulator for DQPSK modulation at 25 Mbps.

[e]12.4 pJ/bit for DQPSK modulation at 2 Mbps. 160 pJ/bit for SSB OFDM modulation at 1.25 Mbps.

198 pJ/bit for SSB FSK modulation at 1.0 Mbps.

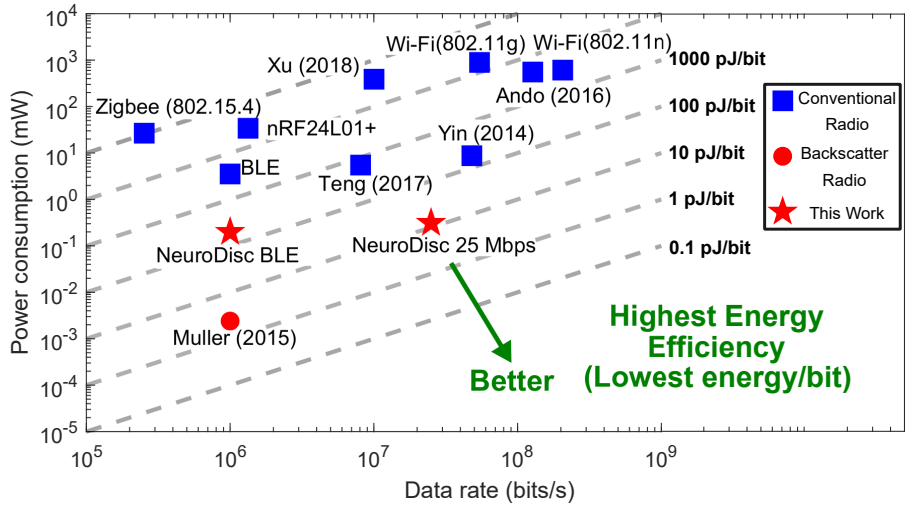

Figure 1.4: Comparison of the wireless uplink efficiency of state-of-the-art wireless neural recorders and common wireless standards.

1.6 Original Contributions

This work makes the following original contributions that we believe advance the current state-of-the-art in low-power wireless sensing and neural recording systems:

- The first far-field, wireless backscatter uplink >10 Mbps on a neural recorder [16, 54],
- The first DQPSK backscatter uplink for a wireless neural recorder [16],
- The first fully-digital BLE backscatter uplink [45],
- The first demonstration and analysis of a SSB BLE backscatter uplink [46],
- The first demonstration of OFDM backscatter communication using fully-digital hardware [47],
- The first characterization of the channel transfer function (CTF) inside a typical NHP cage within the 2.4 GHz ISM band [53], and
- The first demonstration of electronic mode stirring using switched parasitic antennas to improve the 915 MHz and 2.4 GHz CTFs inside a metal cage.

1.7 List of Relevant Publications

Publications In Revision

1. **J. Rosenthal**, A. Pike, S. Reyes, and M.S. Reynolds, "Electronic Mode Stirring for Improved Backscatter Communication Link Margin in a Reverberant Cavity Animal Cage Environment," submitted to *IEEE Transactions on Antennas and Propagation* in Jan. 2021, in revision.

Peer-reviewed Journal Publications

4. **J. Rosenthal** and M.S. Reynolds, "Hardware-Efficient All-Digital Architectures for OFDM Backscatter Modulators," in *IEEE Transactions on Microwave Theory and Techniques*, vol. 69, no. 1, pp. 803-811, Jan. 2021.

3. **J. Rosenthal** and M. S. Reynolds, "A 1.0-Mb/s 198-pJ/bit Bluetooth Low-Energy Compatible Single Sideband Backscatter Uplink for the NeuroDisc Brain-Computer Interface," in *IEEE Transactions on Microwave Theory and Techniques*, vol. 67, no. 10, pp. 4015-4022, Oct. 2019.

2. **J. Rosenthal**, A. Sharma, E. Kampianakis and M. S. Reynolds, "A 25 Mbps, 12.4 pJ/bit DQPSK Backscatter Data Uplink for the NeuroDisc Brain Computer Interface," in *IEEE Transactions on Biomedical Circuits and Systems*, vol. 13, no. 5, pp. 858-867, Oct. 2019.

1. A. Sharma, E. Kampianakis, **J. Rosenthal**, A. Pike, A. Dadkhah and M. S. Reynolds, "Wideband UHF DQPSK Backscatter Communication in Reverberant Cavity Animal Cage Environments," in *IEEE Transactions on Antennas and Propagation*, vol. 67, no. 8, pp. 5002-5011, Aug. 2019.

Peer-reviewed Conference Publications

9. **J. Rosenthal** and M.S. Reynolds, "On-the-fly Adaptation of Backscatter Modulator Impedances Using Digitally-Tuned Capacitors," *2021 IEEE Topical Conference on Wireless Sensors and Sensor Networks (WiSNet)*, Virtual, 2021, pp. 5-7.

8. T. Petrie, **J. Rosenthal**, and M.S. Reynolds, "A Low-Cost 1 Mbps Frequency Shift Keying Backscatter Receiver and Carrier Wave Generator System for Wireless Neural Recording," *2020 IEEE International Conference on RFID (RFID)*, Virtual, 2020, pp. 1-5.

7. **J. Rosenthal** and M.S. Reynolds, "A Dual-Band Shared-Hardware 900 MHz 6.25 Mbps DQPSK and 2.4 GHz 1.0 Mbps Bluetooth Low Energy (BLE) Backscatter Uplink for Wireless Brain-Computer Interfaces," *IEEE Conference on RFID*, Virtual, 2020, pp. 1-6.

6. **J. Rosenthal** and M.S. Reynolds, "All-Digital Single Sideband (SSB) Bluetooth Low Energy (BLE) Backscatter with an Inductor-free, Digitally-Tuned Capacitance Modulator," *IEEE International Microwave Symposium*, Virtual, 2020, pp. 468-471.

5. L. Arjona, **J. Rosenthal**, J.R. Smith, and C.T. Moritz, "High Performance Flexible Protocol for Backscattered-based Neural Implants," in *2019 IEEE-APS Topical Conference on Antennas and Propagation in Wireless Communications (APWC)*, 2019, pp. 276-280.

4. **J. Rosenthal**, A. Pike and M. S. Reynolds, "A 1 Mbps 158 pJ/bit Bluetooth Low Energy (BLE) Compatible Backscatter Communication Uplink for Wireless Neural Recording in an Animal Cage Environment," *2019 IEEE International Conference on RFID (RFID)*, Phoenix, AZ, USA, 2019, pp. 1-6.

3. **J. Rosenthal** and M. S. Reynolds, "A 158 pJ/bit 1.0 Mbps Bluetooth Low Energy (BLE) Compatible Backscatter Communication System for Wireless Sensing," *2019 IEEE Topical Conference on Wireless Sensors and Sensor Networks (WiSNet)*, Orlando, FL, USA, 2019, pp. 1-3.

2. A. Dadkhah, **J. Rosenthal**, and M. S. Reynolds, "ZeroScatter: Zero-Added-Component Backscatter Communication Using Existing Digital I/O Pins," *2019 IEEE Topical Conference on Wireless Sensors and Sensor Networks (WiSNet)*, Orlando, FL, USA, 2019, pp. 1-3.

1. **J. Rosenthal**, E. Kampianakis, A. Sharma and M. S. Reynolds, "A 6.25 Mbps, 12.4 pJ/bit DQPSK Backscatter Wireless Uplink for the NeuroDisc Brain-Computer Interface," *2018 IEEE Biomedical Circuits and Systems Conference (BioCAS)*, Cleveland, OH, 2018, pp. 1-4.

Chapter 2

BACKSCATTER COMMUNICATION WITH HIGHER-ORDER MODULATION FOR STREAMING NEURAL TELEMETRY

Key point: Higher-order modulation schemes, such as quadrature phase-shift keying, can be practically implemented in a backscatter communication system to efficiently increase data rates. We present a 25 Mbps DQPSK backsatter uplink implemented on the NeuroDisc with an RF modulator efficiency of 12.4 pJ/bit. We validate the system by recording and uplinking 16 simultaneous channels recorded *in vivo* from the primary motor cortex of an anesthetized non-human primate (NHP).

This section is based on the work presented in [16, 54].

2.1 Introduction

The NeuroDisc is a wireless brain-computer interface (BCI) designed for neural recording experiments on NHPs. (Fig. 2.1). For this work, a differential quadrature phase shift keying (DQPSK) backscatter modulation scheme was designed to transmit two bits per symbol, yielding a data rate of 25 Mbps. Previous BCIs using backscatter communication have used amplitude shift keying (ASK) [34] at 1 Mbps and binary phase shift keying (BPSK) at 5 Mbps [17] which transmit data with a spectral efficiency of one bit per symbol. While higher spectral efficiency backscatter modulators have been demonstrated using quadrature amplitude modulation (QAM) [40], and a 32-QAM backscatter integrated circuit with a 2.5 Mbps data throughput and 45.2 pJ/bit energy efficiency was presented in [55], neither of those modulators were validated in a complete system. The NeuroDisc's all-digital backscatter modulator consumes only 309 μW and has an energy efficiency of 12.4 pJ/bit, which is orders of magnitude lower than commercially available transmitters.

This chapter presents new innovations that expand the bandwidth of the complete RF signal chain to enable an energy efficient 25 Mbps DQPSK backscatter uplink. Section 2.2 provides an overview of the NeuroDisc system design, including the BCI antenna, the Comms FPGA, the DQPSK backscatter modulator, and the custom full-duplex receiver. Section 2.3 presents our experimental results with the NeuroDisc that include a characterization of the 25 Mbps DQPSK backscatter uplink, a comparison of the NeuroDisc to an existing neural recording system [56], and 16-channels of *in vivo* recordings from a pigtail macaque. Section 2.4 concludes with a discussion of the results, conclusions, and future work.

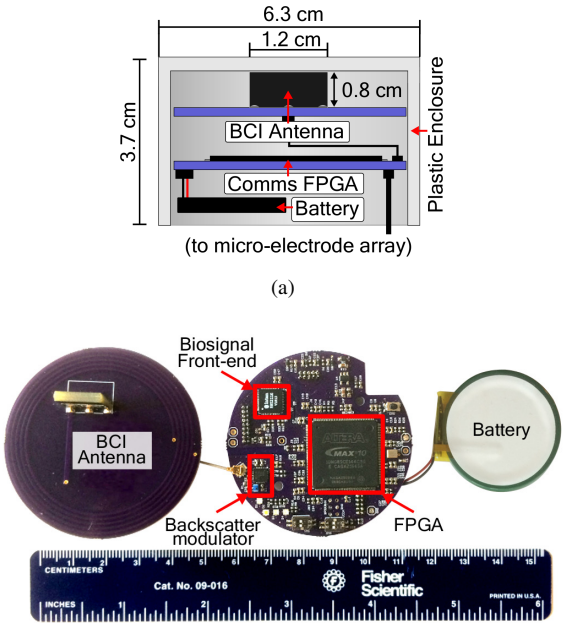

Figure 2.1: (a) Drawing of the NeuroDisc in its plastic case. (b) Photo of the three main components that comprise the NeuroDisc: the BCI antenna, the Comms FPGA, and the battery.

2.2 System Design

What differentiates the NeuroDisc from other wireless BCIs is its 25 Mbps DQPSK backscatter uplink. The NeuroDisc is comprised of a wide-band BCI Antenna for the 915 MHz ISM band, a Comms FPGA circuit board for command and data handling functions, and a single-cell 3.7V, 500 mAh lithium-ion battery to power the device. The total power consumption of the NeuroDisc is 160 mW, however, only 309 μW are used for wireless communication. Nearly 90% of the total power consumption is due to the static power consumption of the particular FPGA , which was chosen to ease development of the backscatter uplink. This power draw could be significantly reduced by changing the FPGA to another device (such as the very low power Igloo Nano series from Microsemi), lowering the supply voltage, and by porting the digital design to an integrated circuit solution.

The NeuroDisc provides a low-power electrophysiology interface that can sample 16 channels at 20 kSps with 16-bit resolution, thus enabling recording of broadband neural signals. Data is then uplinked to a custom full-duplex UHF backscatter receiver that provides an external carrier wave as well as complete receiver chain that receives, demodulates, decodes, and reconstructs recordings. An overview of the NeuroDisc signal chain is shown in Fig. 2.2.

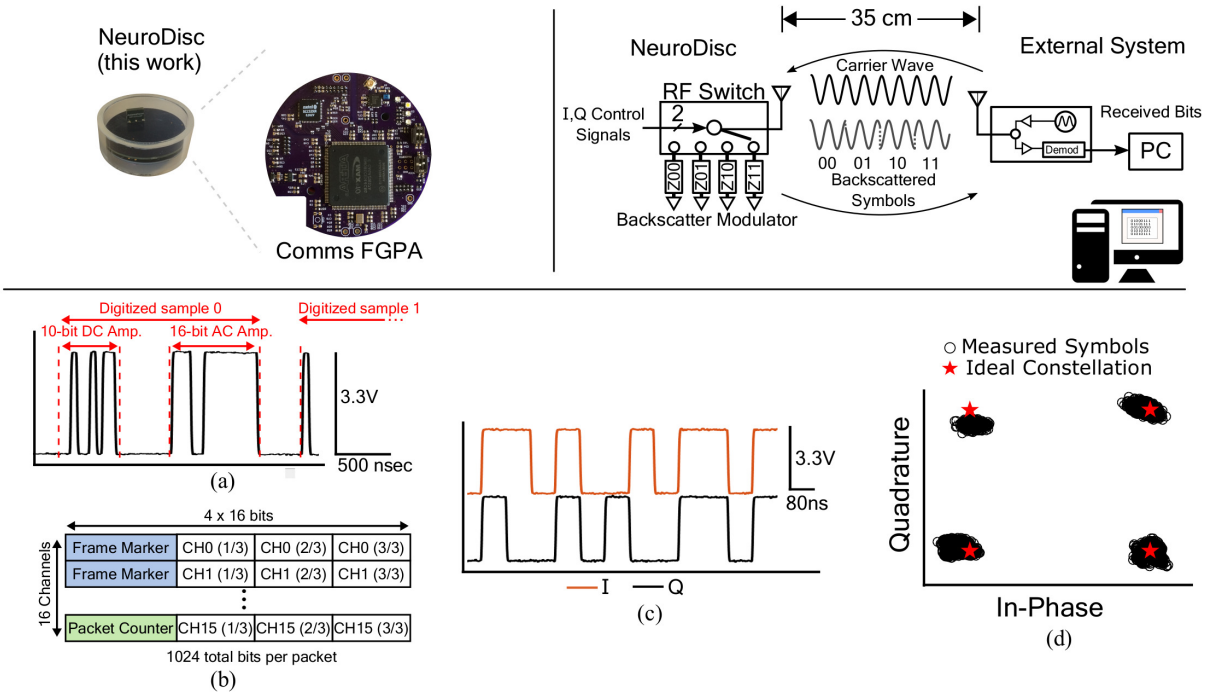

Figure 2.2: An overview of the signal chain for NeuroDisc's 25 Mbps backscatter uplink. (a) Digital samples are collected by the FPGA over an SPI bus. (b) Samples are assembled in a 1,024-bit packet after application of the error correction code. A packet counter is added to detect dropped packets. (c) The packet is encoded into DQPSK symbols and output from two GPIO pins on the FGPA. These signals control the backscatter modulator, determining to which impedance the BCI antenna is connected. (d) The DQPSK constellation can be measured at the receiver and decoded into symbols.

2.2.1 BCI Antenna Design

The NeuroDisc uses the semi-custom BCI Antenna shown in Fig. 2.1 and 2.3 for data uplink to the external system in the 915 MHz industrial, scientific, and medical (ISM) band. The antenna was designed, simulated, and tested by Apoorva Sharma, and further detailed information can be found in her dissertation [57]. In previous work [54], the NeuroDisc's maximum wireless data rate was restricted to 6.25 Mbps due to a -10 dB antenna return-loss bandwidth of 1 MHz. The BCI antenna presented in this work was designed to have a wider bandwidth of 12.5 MHz to support higher data rates. It incorporates a Linx Technologies (Merlin, OR) Ant-916-USP antenna element (Fig. 2.4) on a custom two-layer printed circuit board (PCB) with a 55 mm outer diameter using a 1.6 mm-thick FR–4 substrate with 30 µm thick copper. This specific antenna element was chosen for this application due to its low cost, compact form factor of 12.7 mm x 9.2 mm x 2.8 mm (width x length x height) and its wide bandwidth. As shown in Fig. 2.4 the

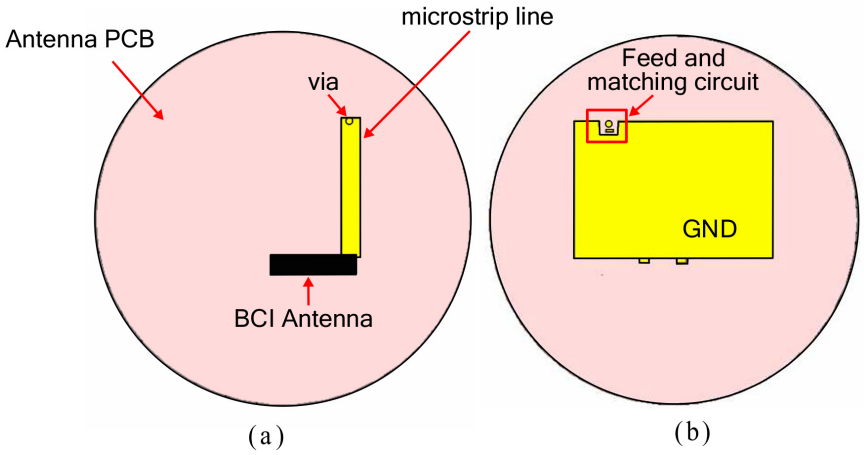

Figure 2.3: Layout of the 915 MHz antenna [57]. (a) Top view (b) Bottom view.

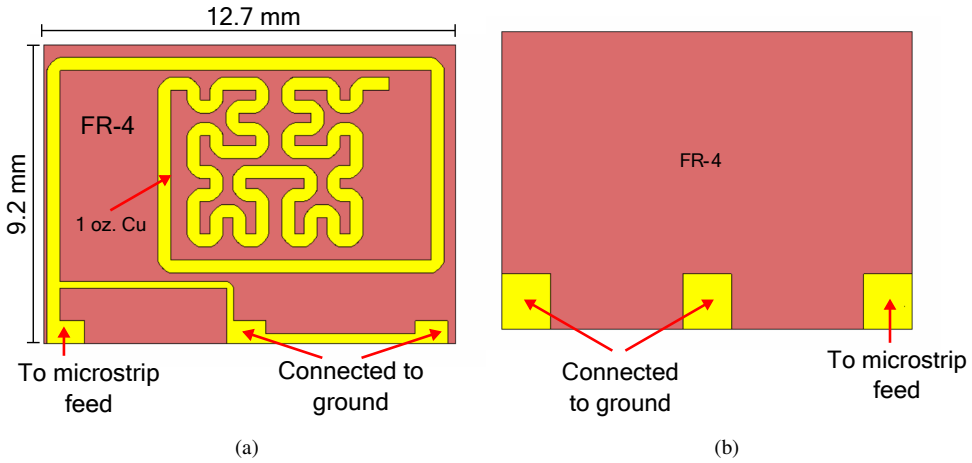

Figure 2.4: Schematic diagram of the commercial off-the-shelf antenna element (BCI antenna) [57]. (a) Front View (b) Back View.

antenna element is fed on the top side of the PCB with three connection pads, where one pad is connected to a 50 Ω microstrip feed line and the other two connect to a 30 mm x 20 mm rectangular ground plane on the bottom of the PCB. Included on the bottom of the PCB are a UMC coaxial connector and a passive UHF matching network consisting of a series 8.2 nH inductor and a shunt 0.3 pF capacitor.

The return-loss ($|S_{11}|$ dB) of the BCI antenna was simulated by Apoorva Sharma in CST Microwave Studio [58] and measured on an Agilent Technologies N5222A network analyzer to determine the antenna's bandwidth. The

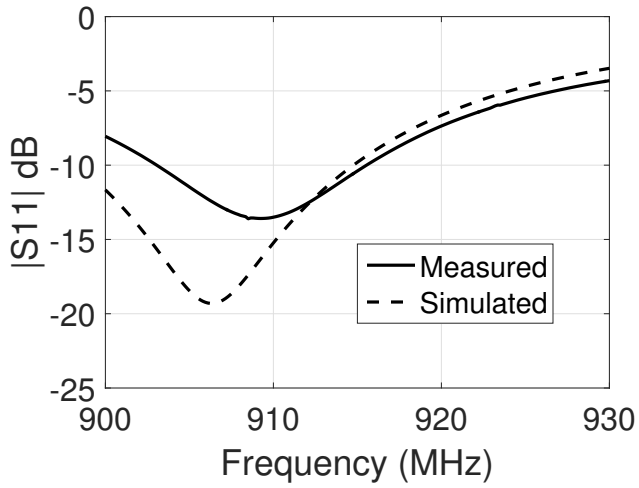

Figure 2.5: $|S_{11}|$ of the antenna matched well between the measured antenna and simulations. The antenna exhibited a measured -10 dB bandwidth of 12.5 MHz with a center frequency of 909 MHz [57].

simulated and measured results are plotted in Fig. 2.5 and show comparable -10 dB return-loss bandwidths, with the simulation being between 898.2 MHz to 914.7 MHz (16.5 MHz) and the measured being between 903 to 915.5 MHz (12.5 MHz). The gain pattern and surface currents were also simulated, showing a realized gain of -13.6 dBi and surface currents concentrated on the BCI antenna (Fig. 2.6).

2.2.2 Comms FPGA Design

The Comms FPGA board provides command and data handling functionality to the NeuroDisc. It can be split into three main subsytems on the board: a biosignal front-end, an FPGA, and a backscatter modulator (Fig. 2.1). Analog signals are measured at the biosignal amplifier and digitized. The samples are then passed over a digital serial-peripheral interface (SPI) bus to the FPGA, where they are then processed, packetized, and encoded into control signals for the backscatter modulator. An overview of the signal chain is presented in Fig 2.2.

The biosignal front-end leverages an Intan Technologies [48] RHS2116 integrated circuit (IC). The IC provides 16 independent amplifier channels and an on-chip 16-bit analog-to-digital converter (ADC) to sample each channel in a round-robin fashion at up to 20 kSps. The IC is controlled via a 32-bit SPI bus with a 12.5 MHz clock frequency.

The NeuroDisc's digital logic was implemented in Verilog on an Intel MAX10 FPGA [59] running from a 50 MHz clock. The main logic modules are shown in Fig. 2.7 and consist of an SPI Master, Error Correction Coding (ECC), a Packet Manager, and a DQPSK Encoder implemented as a finite state machine (FSM). The SPI Master provides a full-duplex interface for commanding the biosignal front-end and receiving digitized samples. Each sample is 32 bits

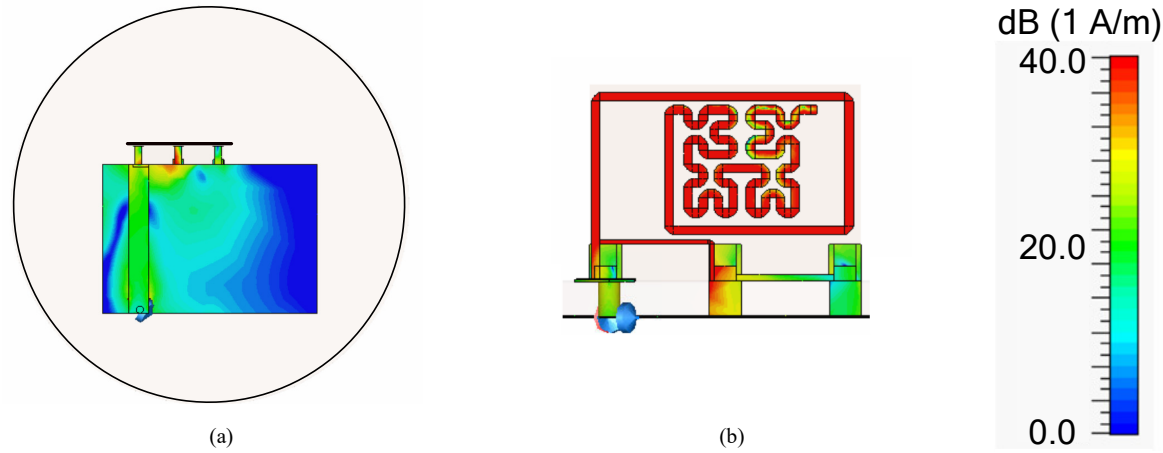

(a) (b)

Figure 2.6: Simulated surface currents on the antenna [57]. (a) Top view showing the microstrip line (top layer) and GND plane (bottom layer) (b) Side view of the antenna element.

Table 2.1: DQPSK modulator impedances

	Ideal Impedance States		Actual Impedance States
Z	**L/C Value**	ρ	**L/C**
Z_{00}	1.74 pF	0.5 - j0.5	1.5 pF
Z_{01}	17.39 nH	0.5 + j0.5	20 nH
Z_{10}	8.7 pF	-0.5 - j0.5	8.4 pF
Z_{11}	3.48 nH	-0.5 + j0.5	3.3 nH

long, containing 16 bits from the high-gain AC amplifier, 10-bits from the low-gain DC amplifier, and five '0' bits for padding (Fig. 2.2(a)). This sample is passed to the ECC module where a Hamming(16,11) ECC is applied. The benefit of using this ECC block is that it provides single error correction and dual error detection at the receiver, allowing for correction of many random independent bit errors that might occur [60]. After application of the ECC, data is passed to the Packet Manager module where the first 15 channels are concatenated with a 16-bit frame marker and the last channel is concatenated with a 16-bit packet counter in order to detect dropped packets. This process forms the 1,024-bit packet shown in Fig. 2.2(b). Once the packet has been generated, it is encoded as DQPSK symbols in the DQPSK Modulator FSM module.

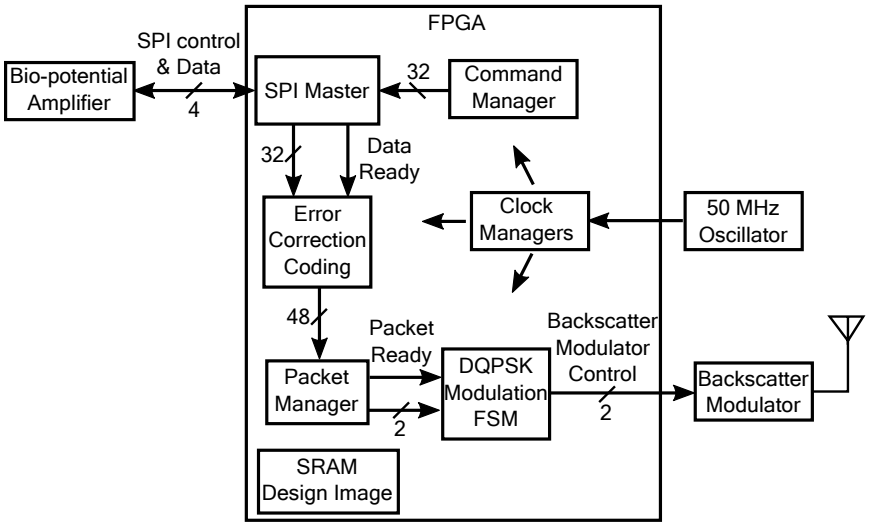

Figure 2.7: Block diagram of the digital logic on the FPGA.

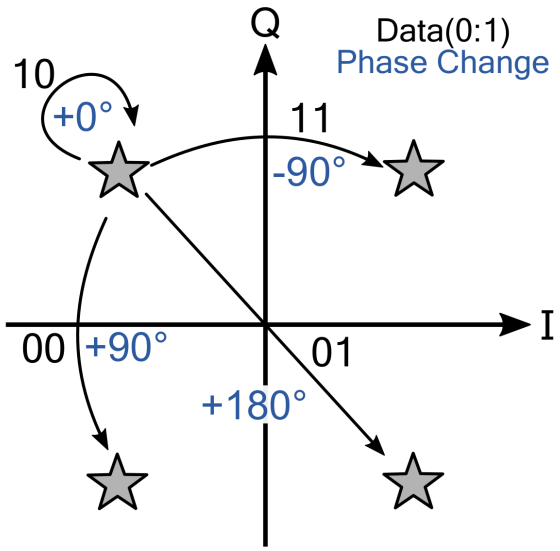

Figure 2.8: State diagram depicting how data bits are mapped to DQPSK symbols. DQPSK symbols are encoded in the transitions between constellation points rather the absolute phase of constellation points.

2.2.3 DQPSK Backscatter Modulator Design

The NeuroDisc uses DQPSK backscatter modulation to uplink data to the external system. DQPSK backscatter modulation requires four unique reflection states which can be visualized as four symbols in the complex plane with equal

amplitudes and offset in phase by 90°, as shown in Fig 2.8. In contrast to QPSK modulation which encodes data in the absolute phase of the symbol, DQPSK modulation encodes data in the phase transitions between constellation points. For example, if one begins in the top left corner of the constellation of Fig. 2.8 and wishes to transmit the data sequence '00', DQPSK modulation says they must move +90° to the next constellation point in the bottom left corner; if the next data sequence to transmit were '01', they would then transition +180° to the top right of the constellation, etc.

DQPSK modulation can be implemented for backscatter communication by designing a set of reflection coefficients for the antenna whose amplitude and phase match the desired constellation. Several methodologies have been investigated for altering an antenna's impedance for backscatter modulation, including the use of RF switches [61], transistors as switches [41, 62] or variable impedances [63], and digital I/O pins switching between their input and output states [64]. This work uses the switched impedance methodology of [61], which showed how arbitrary M-ary QAM backscatter constellations could be designed using RF switches with discrete impedances.

Since DQPSK requires four constellation points, four load impedances, $Z_1 ... Z_4$, are needed. These load impedances can be determined by specifying the desired complex power wave reflection coefficients [65], $\rho_1 ... \rho_4$, for each modulation state where

$$\rho_i = \frac{Z_i - Z_{\text{a}}^*}{Z_i + Z_{\text{a}}} \tag{2.1}$$

and Z_i represents the ith load impedance, Z_{a} is the input impedance of the antenna and $(\cdot)^*$ is the complex-conjugate operator.

We start by specifying the i-th ideal modulation state in the constellation by its in-phase and quadrature components, (I_i, Q_i), where $\sqrt{|I_i|^2 + |Q_i|^2} \leq 1$ since passive load impedances are used. The complex reflection coefficients are:

$$\rho_i = I_i + jQ_i, \tag{2.2}$$

which can be used with (2.1) to calculate the load impedances.

The ideal impedance values were calculated as shown in Fig. 2.9 and Table 2.1. Actual impedance values differ due to component variations, parasitic impedances, and impedance mismatches on the printed circuit board and the antenna. For backscatter constellations, the worst-case differential radar cross section (RCS) [66] will determine the minimum received power and thus the bit error rate (BER). The differential RCS, $\Delta\sigma$, can be expressed as

$$\Delta\sigma = \frac{\lambda^2 G_{\text{ND}}^2}{4\pi} \min_{i,j \text{ for } i \neq j} |\rho_i^* - \rho_j^*|^2, \tag{2.3}$$

where λ is the wavelength, G_{ND} is the gain of the NeuroDisc's antenna, and i and j are the i-th and j-th modulation states. As higher-order constellations such as 8-PSK or 16-QAM are used, the relative distance between constellation points is reduced, resulting in a higher BER relative to DQPSK for a given power level.

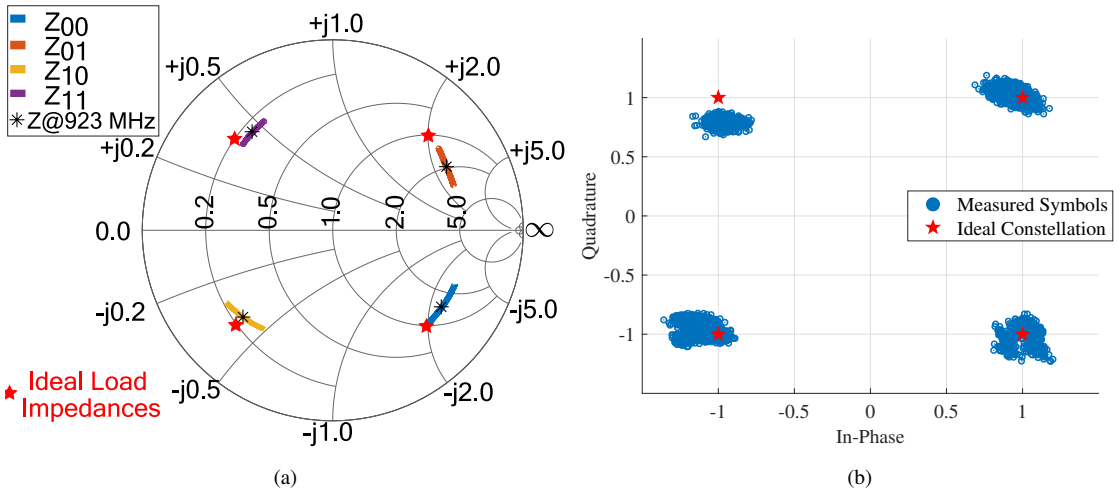

Figure 2.9: (a) Impedance measurements of the DQPSK backscatter modulator states across the 900 MHz ISM band (b) Recorded symbol constellation over 5,000 symbol periods with a calculated EVM of 9.69%.

The backscatter modulator uses an Analog Devices ADG904 SP4T RF switch to connect the antenna to the impedances found in the previous step. Data is encoded as DQPSK symbols in the DQPSK Modulator FSM module on the FPGA (Fig. 2.7). These symbols are then output from the FPGA as two parallel digital signals that control the state of the RF switch, and thus control the reflection coefficient of the BCI Antenna. As shown in Fig. 2.2(c) one control signal corresponds to the I component and the other to the Q component. Since the I and Q control signals are digital, they can actuate the RF switch into the four desired states. The energy consumption per bit of transmitted data was measured for the ADG904 RF switch. The switch was supplied with +3.3 V by a Keithley source-meter, and an Agilent 33500B Waveform Generator drove both control inputs of the switch at a symbol frequency of 12.5 MHz, yielding a bit rate of 25 Mbps. The total static and dynamic current of the RF switch was 93.6 µA at 3.3 V, yielding a power consumption of 309 µW.

2.2.4 Full-duplex Receiver Design

The backscattered DQPSK signals are demodulated using a semi-custom receiver design shown in Fig. 2.10. The receiver was designed by Eleftherios Kampianakis, and advances the design from [19] to accommodate the higher data-rate requirements. We utilize the USRP B210, a low cost commercial off-the-shelf software defined radio (SDR) to transmit the CW signal at 909 MHz and to convert the backscattered RF signals that are modulated at 25 Mbps to I/Q base band signals by processing an instantaneous bandwidth of 40 MHz. The sampled I/Q symbols are sent via a USB3 bus to an Intel Core i7 PC having a 3.8 GHz clock rate and 16 GB of memory. A detailed description of the receiver and its performance can be found in the original publication [16] and Elefterhios Kampaianakis' Ph.D.

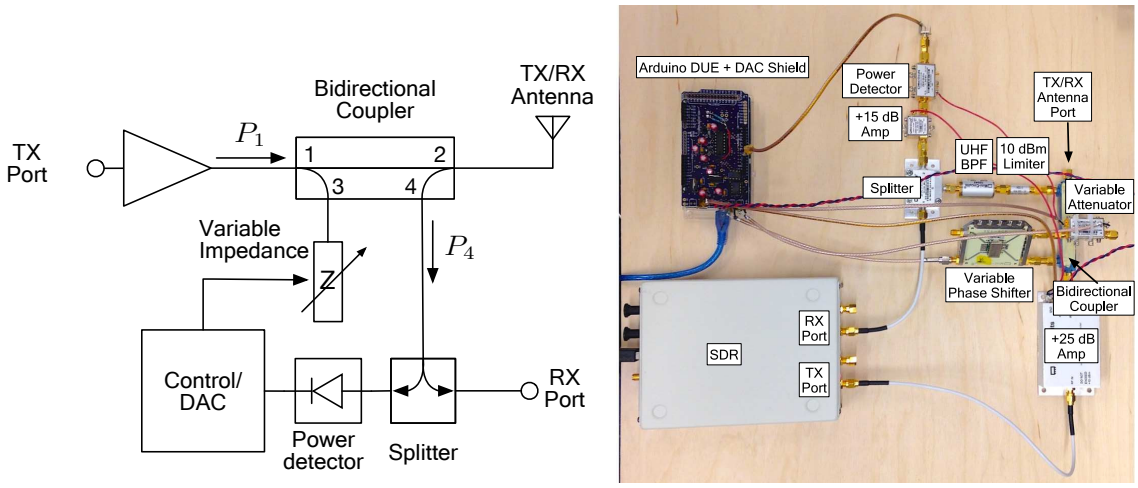

(a) (b)

Figure 2.10: (a) Block diagram of the RF interface and isolation circuitry. (b) Photo of the full-duplex DQPSK backscatter receiver, RF interface, and isolation circuitry [67].

dissertation [67].

2.3 Experimental Results

2.3.1 Error Vector Magnitude Measurement

The NeuroDisc's DQPSK backscatter constellation was evaluated by measuring the error vector magnitude (EVM) at the receiver. The EVM is a figure of merit for how well the measured constellation points align with the ideal DQPSK constellation points [68]:

$$\text{EVM} = 100 \cdot \sqrt{\frac{\frac{1}{N}\sum_{k=1}^{N} |\hat{S}_{k_{ideal}} - S_{k_{sample}}|^2}{\frac{1}{N}\sum_{k=1}^{N} |\hat{S}_{k_{ideal}}|}}, \tag{2.4}$$

where N is the total number of symbols transmitted, $S_{k_{sample}}$ is the normalized k-th demodulated symbol location in the I/Q plane, and $\hat{S}_{k_{ideal}}$ is the ideal normalized symbol position. To measure EVM, the NeuroDisc transmitted five thousand packets, translating to >5e6 bits. The EVM was calculated to be 9.69 % for the measured constellation shown in Fig. 2.9(b).

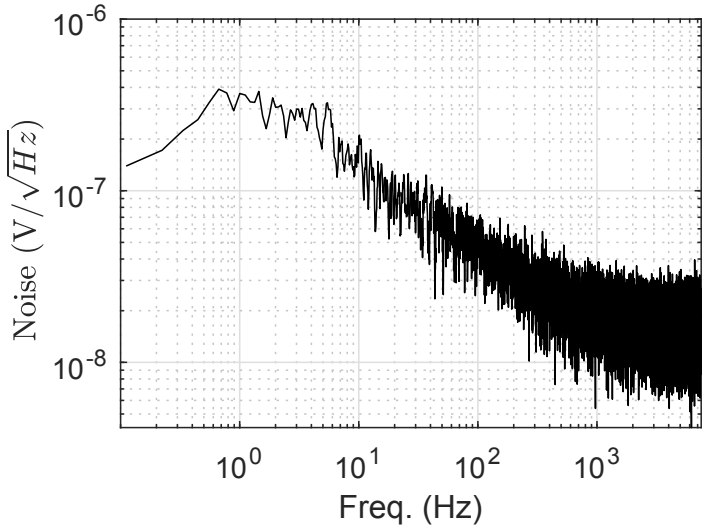

Figure 2.11: Measured input-referred noise spectral density of the NeuroDisc's biosignal front-end.

2.3.2 Characterization of Noise in the Biosignal Interface

Interference is a major concern with wireless neural recorders because sensitive biosignal interfaces are in close physical proximity to high-energy RF and digital signals. To address the risk of signal interference on the circuit board, we measured the input-referenced noise on NeuroDisc's biosignal amplifier. All sixteen measurement channels were grounded and the Comms FPGA was configured to operate nominally, as described in Section II. The NeuroDisc was placed in a Faraday cage to reduce 60 Hz interference from the mains power, and it was connected to the receiver via a UMC-to-SMA cable in order to uplink the data from inside the cage. The NeuroDisc's biosignal front-end was configured with a 20 kHz sampling rate and with a band-pass filter having cutoff frequencies of 1.6 Hz – 7.5 kHz. Ten seconds' worth of samples were collected. Analyzing the received data at the receiver, the measured input-referenced noise was found to be 2.35 μVrms, which shows good agreement with the 2.4 μVrms noise specified in the Intan RHS2116 datasheet, and further shows that the NeuroDisc RF and digital systems do not add significant noise to sensitive biosignal measurements. The measured noise power spectral density from this measurement is shown in Fig. 2.11.

2.3.3 Signal Chain Validation with Pre-Recorded Data

Once the backscatter uplink and biosignal interface had been characterized and shown to be functional, the complete signal chain of the NeuroDisc was validated, as shown in Fig 2.12. Pre-recorded broadband neural data with an amplitude <900 μV (Fig. 2.12(a)) was output from an Agilent 33500B arbitrary waveform generator and measured by

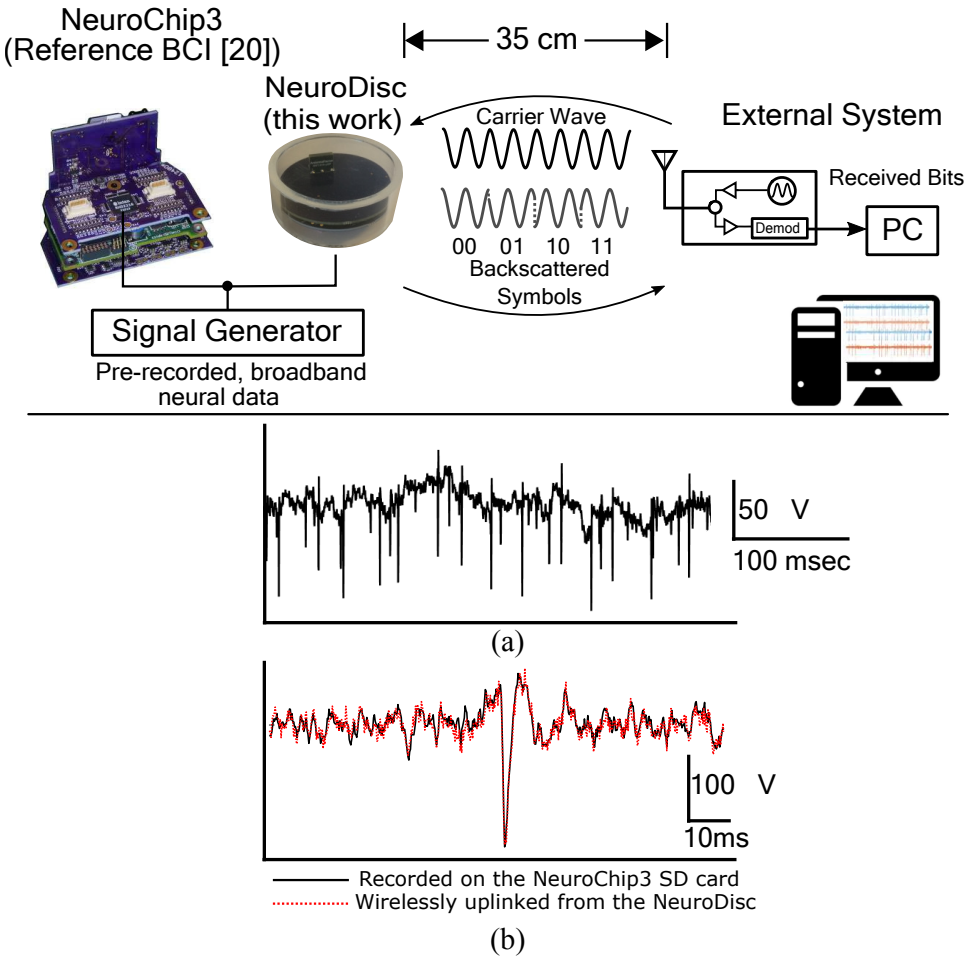

Figure 2.12: Performance of the NeuroDisc with the 25 Mbps backscatter uplink was compared to a reference BCI, the NeuroChip3 [56]. (a) Pre-recorded neural data containing LFP and neural spikes was output from a signal generator and measured by both BCIs. (b) Reconstructed data at the NeuroDisc's external system shows good agreement with samples recorded on the NeuroChip3's SD card.

the NeuroDisc (this work) as well as a reference BCI system (University of Washington Neurochip-3, a recent revision of the NeuroChip2 [32, 56]). The NeuroDisc wirelessly transferred data to the External System using the 25 Mbps backscatter uplink at a distance of 0.35 m, while the NeuroChip3 saved the recorded data to an on-board SD card. Both the NeuroDisc and the NeuroChip3 were configured to sample at 20 kHz while using a 1 Hz – 7.5 kHz band-pass filter and a 1.6 Hz digital high-pass filter. The data received from the NeuroDisc was then plotted over the data recorded by the NeuroChip3 as shown in Fig. 2.12(b) showing good agreement.

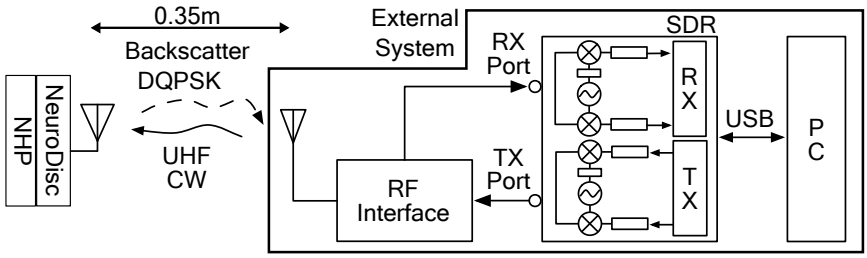

(a)

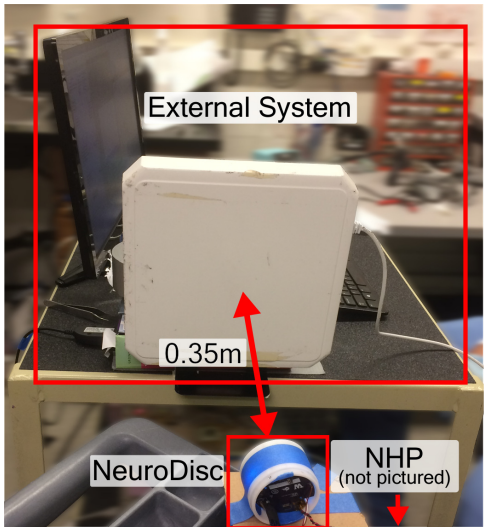

(b)

Figure 2.13: *In vivo* recordings were performed by connecting the NeuroDisc's biosignal front-end to a micro-electrode array previously implanted in the primary motor cortex of a pigtail macaque. (a) Block diagram. (b) Photo of the *in vivo* experimental setup (NHP not pictured due to site policy).

2.3.4 In Vivo Validation

In vivo measurements were performed to validate the NeuroDisc's biosignal interface and high-rate wireless backscatter uplink. Neural signals were recorded from an anesthetized pigtail macaque (*Macaca nemestrina*) who had a 96-channel Utah Array (Blackrock Microsystems) chronically implanted in the primary motor cortex (M1). The experiments were performed at the Washington National Primate Research Center in Seattle, WA, USA, and all experimental procedures were approved by the University of Washington (UW) Institutional Animal Care and Use Committee. Support was provided by personnel from the UW Department of Physiology and Biophysics.

The NHP and the NeuroDisc were on a plastic surgical table with clear line-of-sight to the External System antenna 0.35 m away, as shown in Fig. 2.13. All 16 recording channels of the NeuroDisc were connected to the monkey's

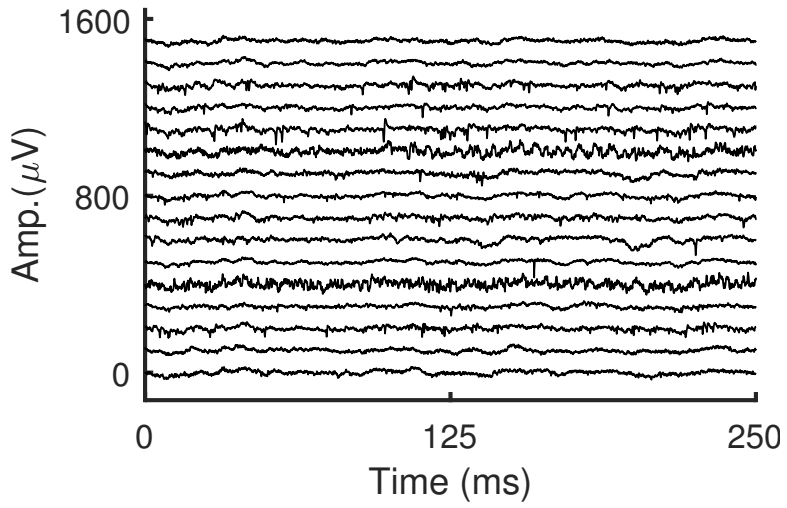

(a)

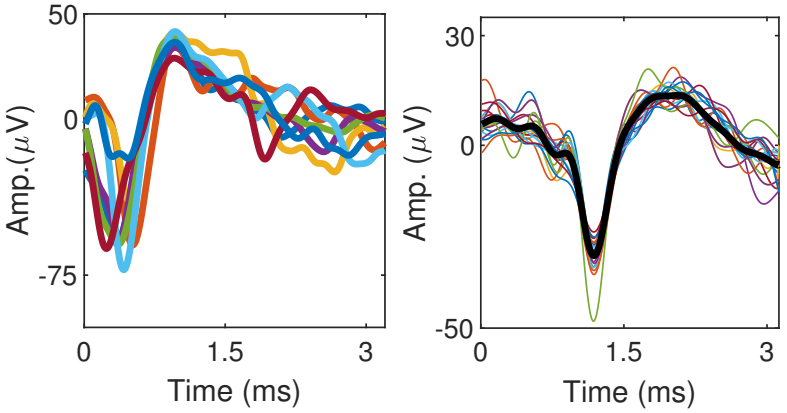

(b) (c)

Figure 2.14: *In vivo* data was uplinked to the external system. (a) Time series plot of all 16 channels of measured neural data. Offline spike sorting was then performed on the data based on [69] (b) Plot of five mean spike waveforms identified in one channel of the data. (c) Plot of the spikes identified within one cluster overlaid with the mean waveform.

implanted electrode via a 17 cm shielded cable. The NeuroDisc was pre-configured to record from all sixteen channels with a sampling rate of 20 kSps with 16-bit resolution per channel. The biosignal front-end was configured with a 1 Hz – 7.5 kHz band-pass filter and a 1.6 Hz digital high-pass filter to remove low-frequency offsets from the data.

Neural signals recorded by the NeuroDisc were uplinked to the External System using the 25 Mbps wireless backscatter uplink. The data was decoded and plotted offline using Matlab. A time-series plot of all sixteen channels is shown in Fig. 2.14(a). Low frequency fluctuations corresponding to local field potentials (LFPs) as well as higher frequency neural spikes can be observed in the data. Some channels exhibited higher noise (e.g. the fifth channel from the bottom in Fig. 2.14(a)) that could be attributed to neural cell loss or glial scarring due to the chronically implanted micro-electrode array. To validate that the neural recordings captured biologically relevant signals, spike sorting was applied to the data set using methods presented in [69]. Several neural spike families were identified in the data (Fig. 2.14(b) and (c)).

2.4 Chapter Conclusions

In this chapter, we introduce a 25 Mbps DQPSK wireless backscatter uplink for use with NeuroDisc brain-computer interface that demonstrates the viability of backscatter uplinks for wireless BCI applications.

Compared to commercial radio uplinks such as Bluetooth Low Energy or 802.11n WiFi with communication efficiencies >4 nJ/bit, the NeuroDisc's DQPSK backscatter uplink is more efficient with a measured energy efficiency of 12.4 pJ/bit. The 25 Mbps data rate of the backscatter uplink represents a 4X improvement compared to previous work in [54]. These improvements were enabled by the design of a wideband UHF antenna, an FPGA-based digital data acquisition system with an integrated DQPSK modulator, and full-duplex DQPSK backscatter receiver providing an average isolation of 89 dB. The system's complete signal chain was validated using pre-recorded neural data and *in vivo* neural recordings from a pigtail macaque.

Chapter 3

BLUETOOTH LOW ENERGY (BLE)-COMPATIBLE BACKSCATTER COMMUNICATION FOR NEURAL RECORDERS

Key point: One challenge that has restricted the widespread use of backscatter communications outside of RFID has been the cost and complexity of backscatter receiver equipment. To overcome this challenge, we present a fully-digital 1.0 Mbps Bluetooth Low Energy (BLE)-compatible uplink for the NeuroDisc with an RF modulator energy efficiency of 158-198 pJ/bit, building off the work in [41] and [70]. We demonstrate for the first time how dynamic sensor data collected by the NeuroDisc can be transmitted using BLE backscatter packets and received by various BLE-enable devices (e.g. smartphones, tablets, off-the-shelf chips) without any hardware or software modifications.
This section is based on the work of [45, 46].

3.1 Introduction

To reduce the burden of custom receivers, recent research has sought to integrate backscatter communications with existing wireless infrastructure. Bluetooth Low Energy (BLE)-compatible backscatter communications were developed in [41] to send static advertising packets to commodity BLE receivers (e.g. smartphones, tablets, computers) and to send dynamic sensor data in [45]. In [71], a system was developed that could backscatter IEEE 802.11 WiFi- or IEEE 802.15.4 Zigbee-compliant packets, and LoRA compatible packets in [72].

A consistent challenge with backscatter communication has been the spectral inefficiency and out-of-band emissions that arise from using digital square-wave pulses as the baseband modulating waveform. Researchers have investigated ways to improve spectral efficiency of backscatter modulation and thus facilitate the adoption of backscatter

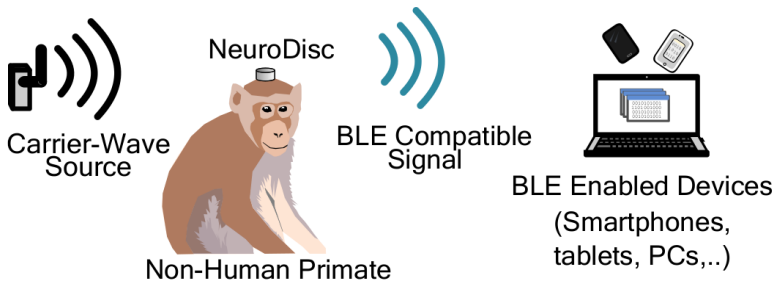

Figure 3.1: Conceptual sketch of the NeuroDisc BLE-compatible backscatter data uplink

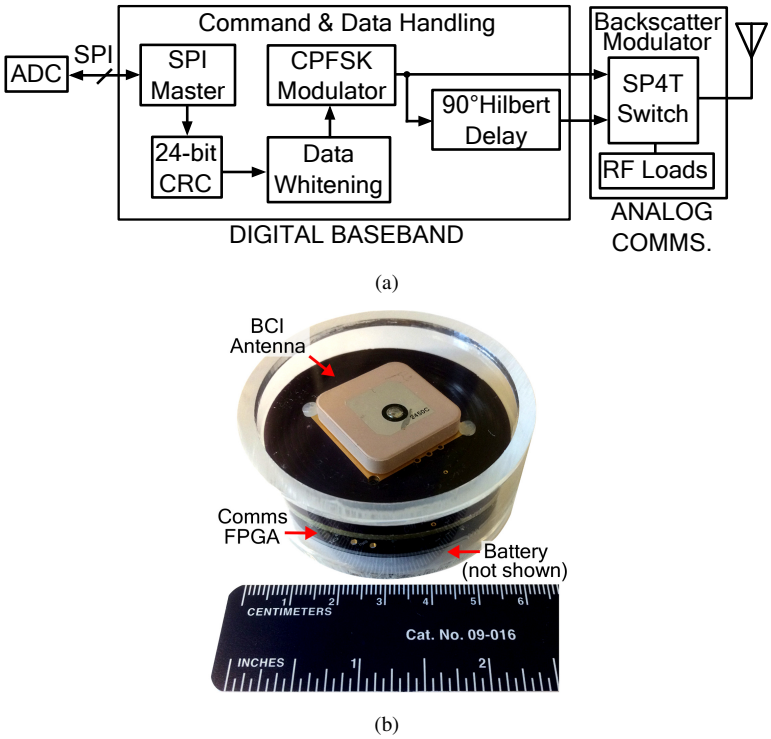

Figure 3.2: Overview of the NeuroDisc hardware architecture. (a) Block diagram of FPGA digital logic. (b) Photo of complete NeuroDisc package using a 2.4 GHz patch antenna.

systems. Pulse-shaping was explored in [63], however, that work required the use of energy-hungry analog biasing circuitry. Single sideband (SSB) backscatter modulation was demonstrated for WiFi and Zigbee packets in [71], however, an analysis of the theoretical vs. realizable performance of SSB backscatter was not presented.

In this chapter, we present the first demonstration and analysis of SSB BLE-compatible backscatter communication with a per-bit energy consumption 50X lower than commercial off-the-shelf BLE transmitters. The system was implemented on the NeuroDisc BCI [54] (Fig. 3.2) and expands on previous work in [45] that presented double sideband (DSB) BLE backscatter for wirelessly streaming sensor data. SSB modulation improves spectral efficiency [73–75] and reduces out-of-band emissions for regulatory compliance, for example, as specified by the U.S. Federal Communications Commission (FCC) (Fig. 3.3). This chapter adds to the state-of-the-art by providing a theoretical framework for SSB backscatter communication and an analysis of the effects of quadrature skew on sideband suppression resulting from imperfect reflection coefficients.

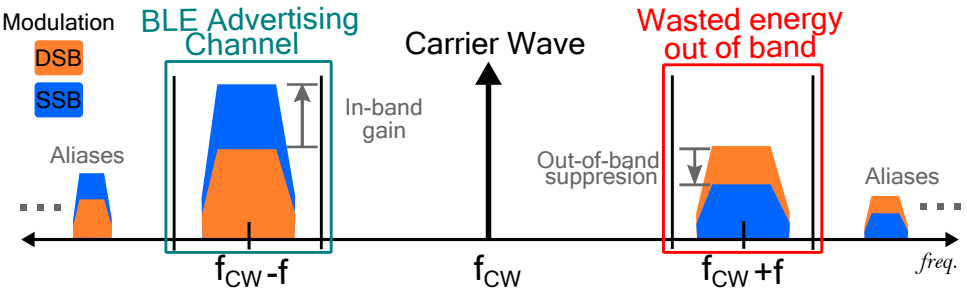

Figure 3.3: Conceptual sketch comparing single sideband and double sideband backscatter modulation. SSB backscatter modulation can improve the reflected power of the desired sideband image.

Table 3.1: Measured NeuroDisc power budget

	Current (mA)	**Power (mW)**	**% of total**
Intan RHS2116 IC	3.27	10.8	5.63 %
FPGA (static baseline)	53.11	175.3	91.35 %
FPGA (dynamic)	1.69	5.59	2.91 %
Backscatter Modulator	0.060	0.198	0.10 %
Total (static+dynamic)	58.13	191.89	

3.2 System Overview

The NeuroDisc comprises a multi-channel ADC to acquire sensor data, an Altera MAX10 FPGA, and a backscatter modulator to uplink data (Fig. 3.2). An Intan RHS2116 analog front-end is used for the bio-potential amplifier, and it provides a 16-channel, 16-bit resolution data acquisition system intended for bio-sensing applications [48]. Power is provided to the NeuroDisc by a single-cell 500 mAh lithium polymer battery. The power budget for the NeuroDisc is provided in Table 3.1.

The Altera MAX10 FPGA performs command and data handling for the NeuroDisc. It controls the multi-channel ADC via SPI to sample and digitize sensor data. BLE advertising packets are then formed by computing a 24-bit CRC and applying data whitening (Fig. 3.2(a)). These packets are modulated using continuous-phase frequency-shift keying (CPFSK) and serially output to the backscatter modulator of Fig. 3.4(a). The backscatter modulator is implemented with an Analog Devices ADG904 SP4T CMOS RF switch. Four distinct impedances are connected to the RF switch, and are chosen as described in Section 3.3.5 below.

3.3 SSB BLE Spectrum Design & Results

3.3.1 BLE Overview

The Bluetooth Core Specification v5.0 [76] defines the physical- and link-layer requirements for BLE-compatible advertising messages. BLE systems are required to operate in 2.4 GHz ISM band at 2.400-2.4835 GHz. The band allocates three channels that are 2 MHz wide for uni-directional advertising: CH37 at 2.402 GHz, CH38 at 2.426 GHz, and CH39 at 2.481 GHz. The BLE advertising packets have a configurable length between 80 and 376 bits. Each packet is composed of five required fields: a preamble, an Access Address (defined to be 0x8E89BED6 for advertising packets), a Protocol Data Unit (PDU) header, a PDU containing data, and a 24-bit CRC calculated using the previous fields. After the packet is constructed, a data whitening filter is applied.

For the NeuroDisc, all packets are generated in the FPGA. The PDU length is set to 152 bits to incorporate a 16-bit ADC sample and a 6-bit packet counter to detect dropped packets. These data are transmitted as ASCII symbols to render them easily readable on commodity BLE scanners (e.g. smartphones). All other fields are constructed per the BLE specification, resulting in a packet length of 232 bits.

3.3.2 BLE Modulation Parameters

BLE requires that a device modulate data using binary frequency-shift keying at a symbol rate of 1.0 Msymbols/s.

Data bits are encoded in the frequency deviation relative to channel's center frequency. A '1' is represented by a positive frequency shift and a '0' is represented by a negative frequency shift.

The subcarrier frequencies for BLE backscatter can be chosen by considering the BLE signal-to-interference ratio (SIR) requirement and the backscatter modulator's power consumption. SIR is the ratio of the BLE signal's power to the power of an undesired interfering signal. If the SIR is lower than the requirement (i.e. if the interference signal is too strong relative to the BLE signal), then the receiver may drop packets. A key trade-off is that as the external carrier-wave (CW) frequency is moved further from the advertising channel center frequency, it can emit at a higher power to achieve a farther range with less interference; however, the subcarrier modulating frequencies must be higher, which increases the power consumption of the backscatter modulator. The BLE specification requires that the receiver maintain a BER $\leq$0.1% for a minimum SIR of -27 dB for adjacent interference $\geq$ 3 MHz from a channel's center frequency. A systematic test of CW induced blocking of a BLE receiver was documented in [70]. In general, the trade-offs in power consumption and SIR will be dependent on the specific backscatter modulator, BLE receiver, and oscillators used in the design. Important considerations are the power consumption of the RF switch as a function of switching rate, the ON/OFF switching time of the RF switch which could limit the maximum switching frequency, and the actual packet error rate vs. SIR performance of the specific BLE receiver used.

3.3.3 Transmitting BLE Advertising Packets via Backscatter

BLE-compatible backscatter signals can be created via simultaneous phase-shift keying (PSK) and continuous phase frequency-shift keying (CPFSK) modulation processes. Frequency-shift keying communication systems often use a CFPSK modulation process to reduce undesired spectral sidelobes [74, 75]. In traditional active radio architectures, CPFSK is used to modulate a carrier wave, however, since a backscatter device does not generate its own carrier signal, CPFSK is instead used to actuate a PSK modulator that will in turn modulate an externally generated carrier incident upon the backscatter device. The PSK process occurs at the backscatter modulator by reflecting the incident carrier wave using switched impedances, while the CPFSK process is generated numerically inside the FPGA to create a digital CPFSK control signal modulated by baseband data from the advertising packet. The CPFSK control signal actuates the RF switch of the backscatter modulator, which connects the antenna to one of the RF loads shown in Fig. 3.4 and thus changes the reflection coefficient of the antenna.

To transmit a '1', the FPGA generates a CPFSK control signal at subcarrier frequency f_{sc1}, and to transmit a '0', it oscillates the signal at subcarrier frequency f_{sc0}. Thus the antenna's reflection coefficient will change as the CPFSK signal actuates the RF switch, resulting in PSK modulation of the incident CW signal.

3.3.4 DSB Bacskcatter Modulation

To perform DSB bacskcatter modulation, we use a CPFSK control signal to actuate an RF switch. The CPFSK control signal, $s(t)$, is a square wave whose frequency changes based on the current symbol, $b_n \in \{0, 1\}$, and whose phase varies based on the current and past symbols (i.e. s has memory). Over a single BLE data bit period, the CPFSK control signal can be expressed as

$$\begin{aligned} s(t) &= \Pi\Big(2\pi f t + \frac{\pi(-1)^{b_n+1}}{2T_\mathrm{b}}(t - nT_\mathrm{b}) + \phi_n\Big), \\ & nT_\mathrm{b} < t \leq (n+1)T_\mathrm{b} \end{aligned} \tag{3.1}$$

where $\Pi()$ is a square wave signal, the center frequency f is $f = \frac{f_{\mathrm{sc0}}+f_{\mathrm{sc1}}}{2}$, $\frac{\pi}{2T_\mathrm{b}}(-1)^{b_n+1}$ is the phase modulation term dependent on the current symbol, n is the bit number, T_b is the bit period (1.0 µsec for BLE), and ϕ_n is a residual phase term. For the phase of $s(t)$ to be continuous between symbols, $\phi_{n+1} = \frac{\pi}{2}(-1)^{b_n+1} + \phi_n$.

As the control signal switches states, the antenna is switched between different discrete loads, thus changing its reflection coefficient. For DSB modulation, two complex-valued reflection states are used:

$$\Gamma_{\mathrm{dsb}}\big(s(t)\big) = \begin{cases} \Gamma_0 = A_0 e^{j\phi_0}, & s(t) = 0 \\ \Gamma_1 = A_1 e^{j\phi_1}, & s(t) = 1 \end{cases} \tag{3.2}$$

with $|A_{0,1}| \leq 1$, $\phi_{0,1} = [0, 2\pi)$, and $\Gamma_1 \neq \Gamma_0$.

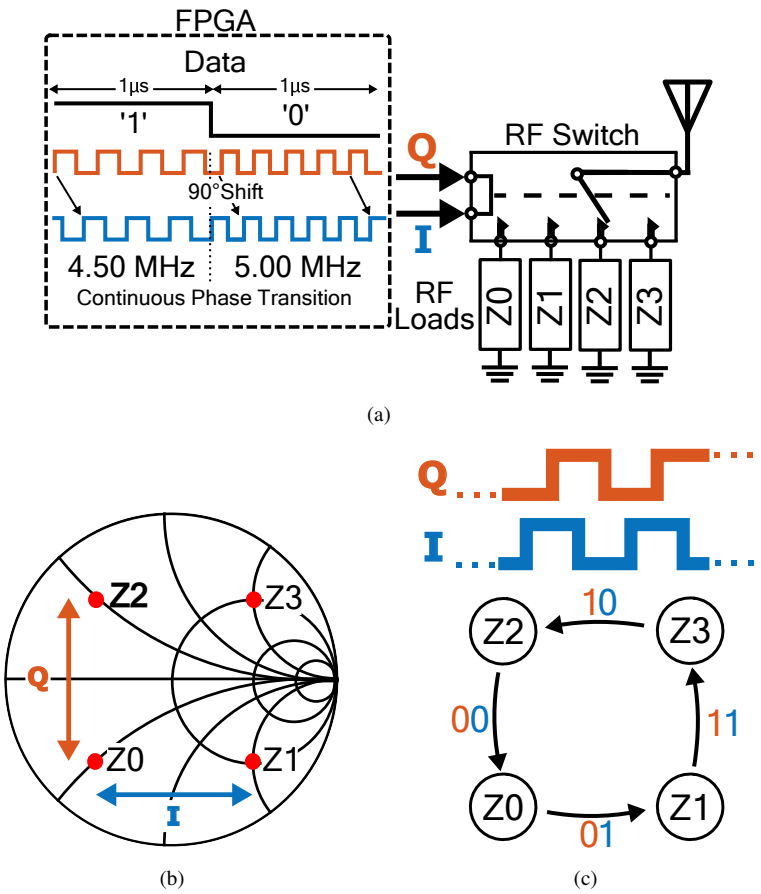

Figure 3.4: Implementation overview: (a) Method for SSB backscatter using in-phase (I) and quadrature (Q) control signals, (b) Smith chart view of the ideal reflection states, (c) State-machine depiction of the SSB modulation process

The modulated signal reflected from the NeuroDisc can be determined by the definition of the reflection coefficient [77]

$$V^{-}(t) = \Gamma_{\text{dsb}}\big(s(t)\big) \cdot V^{+}(t), \tag{3.3}$$

where V^{-} is the reflected signal and V^{+} is the incident CW signal. If we consider $V^{+}(t)$ as a single-tone sinusoidal CW, the reflected DSB signal becomes

$$V^{-}(t) = \Gamma_{\text{dsb}}\big(s(t)\big) \cdot \cos(2\pi f_{\text{cw}} t) \tag{3.4}$$

While the backscatter modulation described above can generate BLE-compatible signals, energy is wasted by generating USB and LSB images of equal magnitude about the carrier frequency, even though the receiver passband includes only one of the images [78]. This undesired sideband could also interfere with other nearby communication

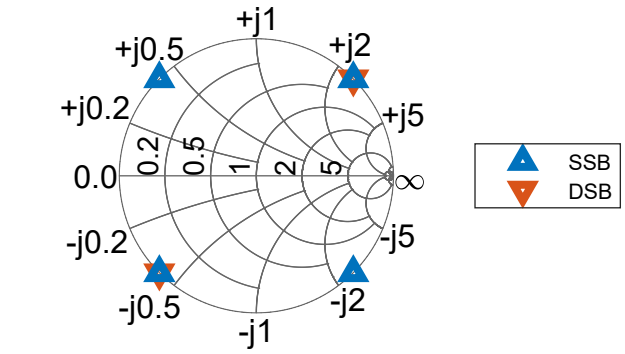

(a)

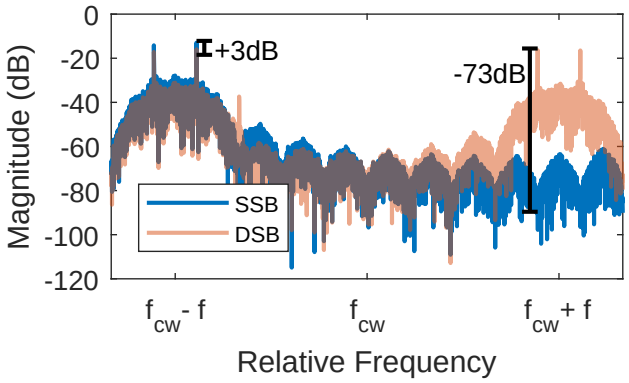

(b)

Figure 3.5: Simulation of SSB and DSB modulation using an ideal constellation, (a) Smith chart plot of the impedance constellation, (b) Simulated power spectral densities between SSB and DSB backscatter modulation

systems and violate RF emissions regulations. One way to recover the lost energy and reduce unwanted emissions is by implementing SSB modulation.

3.3.5 SSB Backscatter Modulation

In DSB modulation, the message signal is fully encoded in both of the sidebands, so recovering either the upper- or lower-sideband image is sufficient for decoding the message. SSB modulation enables more efficient use of bandwidth and power by encoding the message into just one of the sidebands, as shown in Fig. 3.3.

One method for achieving SSB modulation is to use the phasing method [73]. The SSB signal $x_{ssb}(t)$ can be seen as a special case of quadrature amplitude modulation, and it can be written as

$$x_{\text{ssb}}(t) = x(t) \cdot \cos\left(2\pi f_{\text{c}} t\right) \pm \hat{x}(t) \cdot \sin\left(2\pi f_{\text{c}} t\right), \tag{3.5}$$

where $x(t)$ is the message signal, $\hat{x}(t)$ is its Hilbert transform [75], f_{c} is the carrier frequency, and the plus-or-minus

determines which sideband is retained. The Hilbert transform can be seen as a linear filter that shifts the phase on an incoming signal by -90° across all frequencies (i.e. a time delay of a quarter-period when the input function is a baseband square-wave signal).

In the case of SSB BLE backscatter modulation, the backscattered signal is a function of the instantaneous reflection coefficient, so we can express the reflected SSB signal $V_{\text{ssb}}^{-}(t)$ as

$$V_{\text{ssb}}^{-}(t) = \Gamma_{\text{ssb}}\big(s(t), \hat{s}(t)\big) \cdot \cos\left(2\pi f_{\text{cw}} t\right) \tag{3.6}$$

where f_{cw} is the frequency of the externally-supplied CW.

Equation (3.6) can be shown to match the form of (3.5) by implementing time-dependent, complex-valued reflection coefficients. The reflection coefficient $\Gamma_{\text{ssb}}(t)$ can be designed such that its real and imaginary parts are determined by the CPFSK modulator control signal, $s(t)$, and its Hilbert transform $\hat{s}(t)$, respectively. Consider four complex reflection coefficients:

$$\Gamma_{ssb}\big(s(t)\big) = \begin{cases} \Gamma_0 = A_0 e^{j\phi_0}, & s(t) = 0, \hat{s}(t) = 0 \\ \Gamma_1 = A_1 e^{j\phi_1}, & s(t) = 0, \hat{s}(t) = 1 \\ \Gamma_2 = A_2 e^{j\phi_2}, & s(t) = 1, \hat{s}(t) = 0 \\ \Gamma_3 = A_3 e^{j\phi_3}, & s(t) = 1, \hat{s}(t) = 1 \end{cases} \tag{3.7}$$

with $|\Gamma_0| = |\Gamma_1| = |\Gamma_2| = |\Gamma_3|$ and the angles of the four states are as shown in the ideal constellation of Fig. 3.4(b). If we split the reflection coefficients of (3.7) into their real and imaginary parts such that $Ae^{j\phi} = \Gamma_{\text{I}} + j\Gamma_{\text{Q}}$, then we can express (3.6) as

$$\begin{aligned} V_{\text{ssb}}^{-}(t) &= \left[\Gamma_{\text{I}}\big(s(t)\big) + j\Gamma_{\text{Q}}\big(\hat{s}(t)\big)\right] \cdot \cos\left(2\pi f_{\text{cw}} t\right) \\ &= \Gamma_{\text{I}}\big(s(t)\big) \cdot \cos\left(2\pi f_{\text{cw}} t\right) - \\ &\qquad \Gamma_{\text{Q}}\big(\hat{s}(t)\big) \cdot \sin\left(2\pi f_{\text{cw}} t\right) \end{aligned} \tag{3.8}$$

where $\Gamma_i = \Gamma_{\text{I}} + j\Gamma_{\text{Q}}$ for $i \in \{0, 1, 2, 3\}$. To suppress the other sideband image, the subtraction in Eq. (3.8) can be changed to addition.

3.3.6 Simulation of SSB Backscatter Modulation

Simulations in MATLAB evaluated the performance of SSB backscatter modulation. The simulations had two goals: to validate whether SSB backscatter modulation would offer improved spectral performance compared to DSB backscatter, and to analyze how a non-ideal impedance constellation (i.e. quadrature skew) would affect opposite-sideband suppression. The simulations compared the power spectral densities generated by SSB and DSB backscatter modulation. The power spectral densities were computed for the transmission of one BLE advertising packet using DSB and SSB backscatter modulation as described in (3.4) and (3.6), respectively. The ideal constellation shown in Fig. 3.5(a)

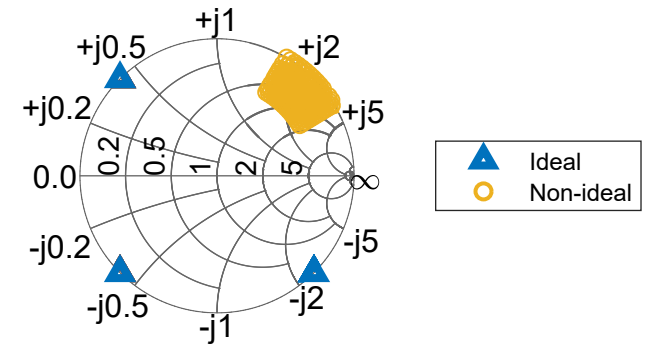

(a)

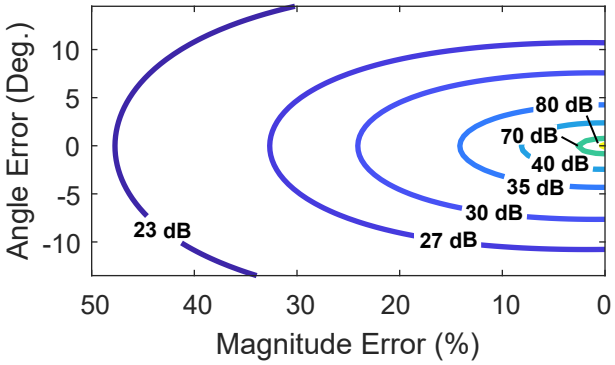

(b)

Figure 3.6: Simulation of SSB modulation using non-ideal constellation points. (a) Smith chart plot of the non-ideal constellation, (b) Contour plot of the SSB suppression ratio for one constellation point with magnitude and phase angle error. Less SSB suppression would be achieved for magnitude and phase errors in multiple constellation points.

was used. A comparison of the power spectral densities for each modulation scheme revealed that ideal SSB modulation yielded a 3 dB increase in power for the desired sideband image and >70 dB of sideband suppression for the undesired sideband image (Fig. 3.5). These simulation results match expectations that the power from the suppressed sideband would be constructively added to the desired sideband, doubling its in-band power. The opposite-sideband suppression ratio would ideally be infinite, however, the simulated result matches our intuition given numeric rounding errors.

The SSB simulations were repeated with non-ideal constellations to analyze how sideband suppression changed with component variations. One disadvantage of SSB backscatter modulation is that opposite-sideband suppression is limited by quadrature skew. Quadrature skew results from magnitude and phase errors in the realized impedance constellation. For the simulations, the magnitude and phase angle of one symbol in the constellation were altered by up

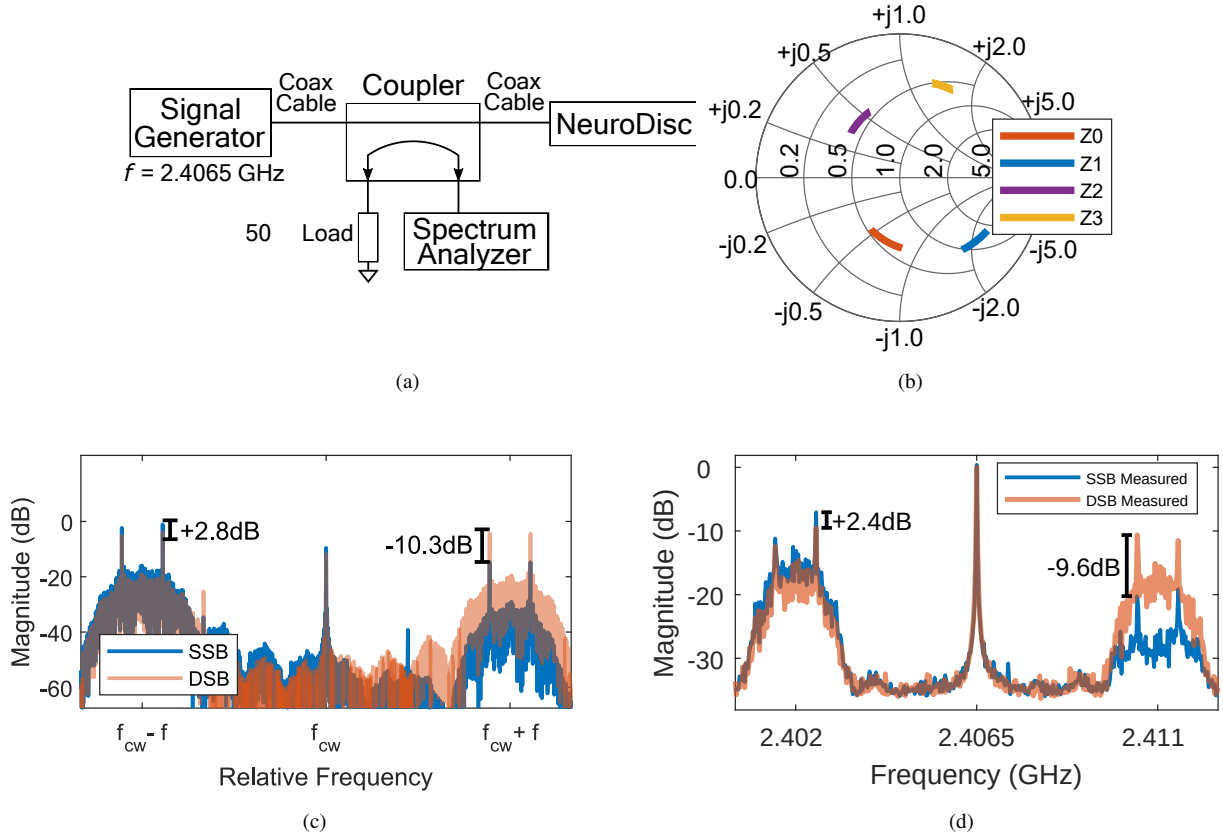

Figure 3.7: (a) Experimental setup for measuring the NeuroDisc's backscattered spectrum. (b) Measured NeuroDisc symbol impedances. (c) Comparison of the simulated DSB and SSB spectra using the measured symbol impedances. (d) Comparison of the measured DSB and SSB spectra.

to 50% magnitude and $\pm$ 15° phase relative to the ideal values (Fig. 3.6(a)). For each deviation, the SSB suppression ratio was calculated as the ratio of the power in the lower sideband image (i.e. the desired sideband) to the power in the upper sideband image (i.e the undesired sideband). From the results shown in Fig. 3.6(b) we see that small deviations significantly degrade the SSB suppression ratio, e.g. 0.5% error in magnitude or phase reduces SSB suppression by nearly 20 dB. Further, additional performance degradation would be witnessed if additional symbol impedances had magnitude and/or phase angle errors. These results emphasize the importance of precise component values and careful circuit layout to achieve optimal performance.

3.4 Link Budget

The free-space link budget for the NeuroDisc was derived following the approaches of [44] and [79]. We considered a bistatic dislocated configuration, because the NeuroDisc, the CW source, and BLE receiver are separate entities, as

Table 3.2: Link budget parameters used for the experimental validation

P_{T}	G_{ND}	G_{T}	G_{R}	λ
0.1 W (20 dBm)	2.2 dBi	2.2 dBi	2.2 dBi	0.1246 m
Z_{a}	Z_0	Z_1	Z_2	Z_3
50 + j 0 Ω	31 - j39 Ω	82 - j125 Ω	21 + j17 Ω	25 + j65 Ω

shown in Fig. 3.1. All antennas are assumed to be optimally aligned and matched. The backscattered power from the NeuroDisc, P_{ND}, can be calculated as

$$P_{\mathrm{ND}} = \frac{P_{\mathrm{T}} G_{\mathrm{T}} \Delta\sigma}{4\pi r_{\mathrm{t}}^2}, \tag{3.9}$$

where P_{T} is the power transmitted from the CW source, G_{T} is the gain of the CW source antenna, r_{t} is the distance between the CW source and the NeuroDisc antenna, and $\Delta\sigma$ is the differential radar cross-section (RCS) of the NeuroDisc. In [66], analytic expressions are provided to calculate the differential RCS of backscatter tags with two reflection states. For backscatter tags using more than two reflection states, we can modify the expressions to identify the worst-case differential RCS between any two reflection states, since this worst-case received power will determine the BER [75]. The differential RCS for the NeuroDisc with BLE bacskcatter can thus be expressed as

$$\Delta\sigma = \frac{\lambda^2 G_{\mathrm{ND}}^2}{4\pi} \min_{i,j \text{ for } i \neq j} |\Gamma_i^* - \Gamma_j^*|^2, \tag{3.10}$$

where λ is the free-space wavelength of the carrier wave, G_{ND} is the gain of the NeuroDisc antenna, and Γ_i^* and Γ_j^* are the reflection coefficients of the backscatter switch states. Considering RF impedances Z_i and Z_j with a resonant antenna impedance Z_{ant}, the reflection coefficients can be calculated:

$$\Gamma_{i,j}^* = \frac{Z_{\mathrm{ant}}^* - Z_{i,j}}{Z_{\mathrm{ant}} + Z_{i,j}}. \tag{3.11}$$

The backscatter power at the receiver is then

$$P_{\mathrm{R}} = \frac{P_{\mathrm{ND}} G_{\mathrm{R}} \lambda^2}{(4\pi)^2 r_{\mathrm{b}}^2} = \frac{P_{\mathrm{T}} G_{\mathrm{T}} \Delta\sigma G_{\mathrm{R}} \lambda^2}{(4\pi)^3 r_{\mathrm{t}}^2 r_{\mathrm{b}}^2} \tag{3.12}$$

by combining equations (3.9) and (3.12) and noting that G_{R} is the gain of the receiver and r_{b} is the distance between the NeuroDisc and the receiver antennas. The link budget parameters for testing the NeuroDisc are shown in Table 3.2.

3.5 Experimental Results

Experiments were performed to validate the SSB backscatter communication uplink. Range experiments measured the effective packet error rate (PER) at different distances. A cabled experiment measured the SSB backscattered spectrum

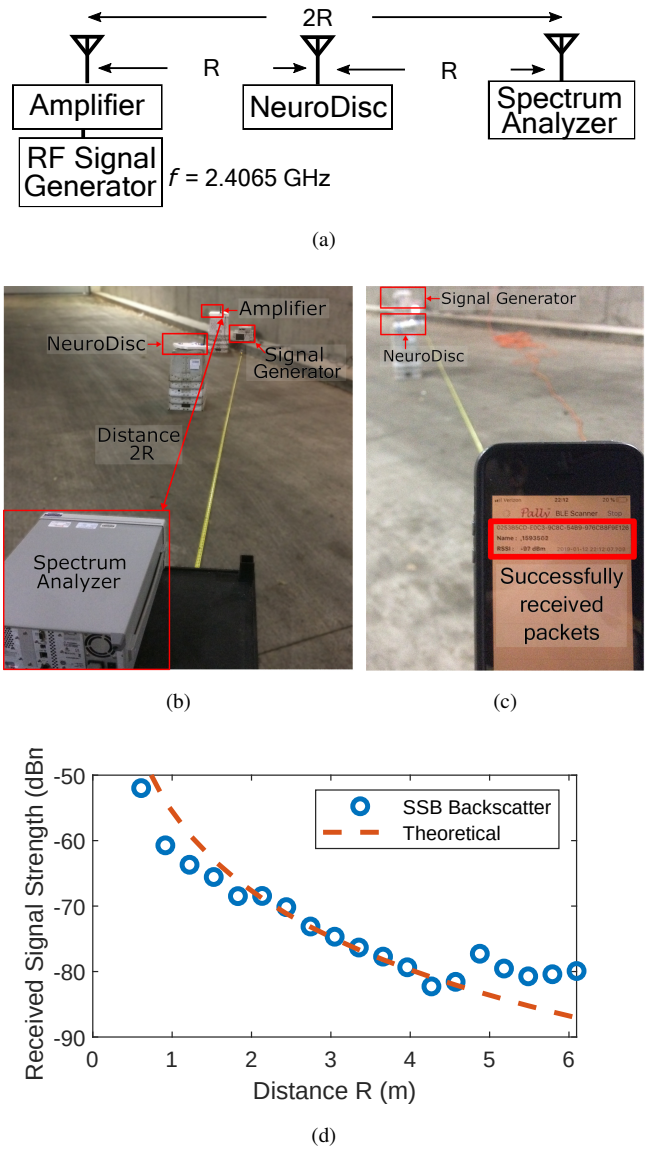

Figure 3.8: Experimental setup for measuring the received signal strength vs. distance. (a) Block diagram. (b) Photo. (c) BLE packets as received on a smartphone at a distance $R = 6$ m. (d) Measured received signal strength vs. distance.

from the NeuroDisc. A data integrity test compared wirelessly uplinked data from the NeuroDisc to the original data to validate the NeuroDisc's complete signal chain.

3.5.1 Measured Backscattered Spectrum

The backscattered spectrum from the NeuroDisc was measured using the setup shown in Fig. 3.7(a). The NeuroDisc was configured to send BLE advertising packets. An Agilent N5181A RF Signal Generator, an Agilent N9320B spectrum analyzer, and a MiniCircuits ZABDC20-252H-S+ coupler were used. The RF loads needed to create the constellation were determined based on methods presented in [40], with final component values chosen to be 0.6 nH, 6.8 nH, 3.3 pF, and 1.8 pF. The constellation shown in Fig.3.7(b) was measured using an Agilent N5222A vector network analyzer. For the DSB modulation measurement, impedances Z0 and Z2 were used. The measurement revealed disparities in the relative angles and magnitudes of the reflection coefficients, likely due to impedance mismatches between the 50Ω measurement equipment and the NeuroDisc circuit board layout. While these mismatches reduced the sideband suppression ratio, the simulated and measured spectra in Fig. 3.7(c) and (d) successfully demonstrate suppression of the undesired sideband at 2.411 GHz while increasing the power of the desired sideband at 2.402 GHz. The measured values show good agreement with the simulated spectra that were generated using measured symbol impedances. The increased power gain (7 dB instead of the the expected 3 dB) can be attributed to the average magnitude of the SSB symbol reflection coefficients being larger than the average distance of the DSB symbol reflection coefficients.

3.5.2 Modulator DC Power Consumption

To measure the modulator energy consumption, the RF switch was supplied with +3.3 V by a Keithley source-meter, and an Agilent 33500B Waveform Generator drove both control inputs of the switch at an average subcarrier rate of 4.75 MHz. The measured current was 60 μA, resulting in a total power consumption (static + dynamic) at the backscatter modulator of 198 μW. At a BLE data rate of 1 Mbps, this corresponds to an energy consumption of 198 pJ/bit.

3.5.3 Range Testing

We measured the received signal strength from the NeuroDisc with respect to distance in the bistatic setup shown in Fig. 3.8. Measurements were performed in an empty parking garage that provided adequate space for range testing and isolation from other 2.4 GHz transmitters (e.g. WiFi and Bluetooth devices) that could interfere. Prior to testing, we surveyed the spectrum between 2.4-2.5 GHz to verify that no other transmitters were present. A calibrated Agilent N9320B Spectrum Analyzer was used to measure the received signal strength with a 10 kHz bandwidth. An Agilent N5181A RF Signal Generator and a MiniCircuits ZRL-3500+ RF amplifier were used to generate a carrier at 2.4065 GHz with a total RF output power of +20 dBm. The CW source, the spectrum analyzer, and the NeuroDisc used L-COM HG2402RDRSF antennas with gains of 2.2 dBi.

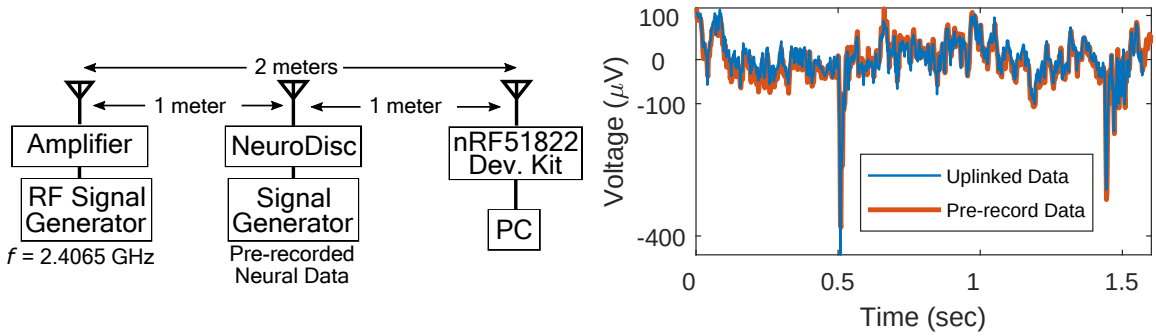

(a) (b)

Figure 3.9: (a) Setup for wirelessly uplinking pre-recorded neural test data. (b) Measured uplinked sensor data vs. re-recorded data.

3.5.4 Wireless Bio-Signal Uplink

To validate that biological signals could be captured and uplinked without distortion, we used the NeuroDisc to uplink low amplitude ($<$500 μV) pre-recorded neural data played back by an Agilent arbitrary waveform generator using the test setup shown in Fig. 3.9(a). Testing occurred in an ordinary office/lab environment. The same COTS BLE device from the range experiment was used to receive advertising packets from the NeuroDisc. An Agilent N5181A RF Signal Generator and a MiniCircuits ZRL-3500+ RF amplifier were used to generate a carrier at 2.4065 GHz with an RF output power of +20 dBm. Both the CW source and the nRF51822 used L-COM HG2402RDRSF antennas with a specified gain of 2.2 dBi. The NeuroDisc was configured to uplink packets at 500 Hz with one sensor sample per packet. The Intan chip was configured with a bandpass filter with a lower cutoff frequency of 0.1 Hz and an upper cutoff frequency of 200 Hz. Received packets were processed and plotted in MATLAB. The received biological data is plotted in Fig. 3.9(b) and shows that the original signal was uplinked through the NeuroDisc and captured by a COTS Nordic Semiconductor nRF51DK BLE evaluation board. The received signal was calculated to have 1.5% root mean square (RMS) error relative to the original pre-recorded data. The majority of the error can be attributed to differences in filtering between the Intan chip and the digital filters applied to the pre-recorded neural data.

3.6 Chapter Conclusions

In this chapter, we have demonstrated an energy efficient wireless uplink for the NeuroDisc brain-computer interface using single-sideband (SSB) Bluetooth Low Energy (BLE) backscatter communication. We presented a design methodology and simulations of SSB backscatter modulation using the phasing method and provided an analysis of how quadrature skew resulting from non-ideal impedance constellations results in reduced opposite-sideband suppression. These simulations were supported by measurements of the SSB backscattered spectrum in a cabled experiment

and over-the-air (OTA) validation of the backscattered link budget in range measurements. End-to-end OTA measurements were then performed with the NeuroDisc sampling pre-recorded neural data, uplinking to an unmodified Nordic Semiconductor nRF51DK BLE receiver.

Chapter 4

A DUAL-BAND, SHARED-HARDWARE BACKSCATTER UPLINK FOR NEURAL RECORDERS

Key point: To provide the benefits of both the high rate 915 MHz DQPSK uplink and the 2.4 GHz BLE-compatible 1.0 Mbps uplink, we demonstrate a time division multiplexed approach to simultaneous BLE and DQPSK operation that required no hardware modifications to the NeuroDisc. This chapter highlights the wideband performance of the NeuroDisc's RF switch-based modulator to stream telemetry in two unlicensed frequency bands. We demonstrate the flexibility of backscatter communication systems to operate across wide frequency bands with multiple protocols, an advantage that is often overlooked in the literature and which could provide additional flexibility to end users.
This section is based on work in [80].

4.1 Introduction

A trade-off when using backscatter communication is choosing whether to use a custom or standards-based communication approach. As shown in Chatper 2, custom modes offer greater flexibility and can be used to achieve high data rates with high per-bit energy efficiencies, but they require custom receivers that could be burdensome to end-users because of higher cost and complexity than fully-integrated single-chip receivers available for standards-based approaches. In contrast, standards-based approaches simplify the system by enabling compatibility with existing commercial-off-the-shelf (COTS) receivers [41, 46, 71]. As discussed in Chatper 3, BLE-compatible backscatter can be received by any of the billions of existing BLE-enabled devices, such as smartphones, tablets, and laptops [41, 46]. However, implementing a standards-based approach may reduce the data rate and/or energy efficiency of the backscatter uplink.

In this chapter, we present a dual-mode backscatter uplink that combines the benefits of a radio supporting both custom and standards-based uplinks. The system provides a custom 900 MHz differential quadrature phase-shift-keying (DQPSK) backscatter uplink with 6.25 Mbps throughput and a 2.4 GHz single sideband (SSB) BLE-compatible backscatter uplink with 1.0 Mbps data rate (Fig. 4.1a). A dual-band antenna enables operation in both frequency bands. Previous backscatter systems have been designed to operate in separate frequency bands for data and wireless power transfer, such as in [10], however, only one communication mode was used. Other works have demonstrated a backscatter system capable of transmitting two different standards-based protocols in the 2.4 GHz band [71] and a backscatter modulator that can operate in both the 900 MHz and 2.4 GHz bands [81]. However, to the author's knowledge, this work is the first to demonstrate a dual-band, dual-mode backscatter uplink that leverages a high-rate

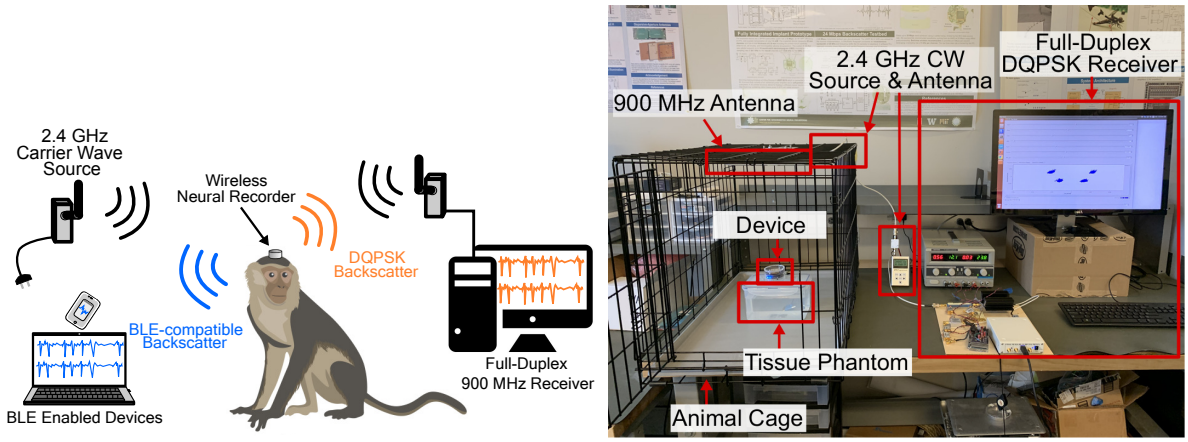

(a) (b)

Figure 4.1: Example deployment of a wireless neural recorder leveraging a dual-band backscatter data uplink.

custom protocol and a standards-based protocol.

The dual-mode backscatter uplink is a unique contribution to the literature on wireless BCIs by presenting an ultra-low power wireless system that meets the needs of multiple stakeholders involved in NHP research. For example, with the same piece of hardware researchers can use the high-rate DQPSK mode to retrieve data from electrophysiological experiments, while technicians can use the BLE mode to monitor the health and status of the NHPs' implanted electrodes by simply checking an app on their smart phones. A comparable system designed using commercially-available active radios would incur significant additional complexity in hardware and software. Each radio would each require their own power, data, and mechanical interfaces, and a significantly larger power budget would be needed to support two individual RF frequency synthesizers.

Table 4.1: Backscatter modulator impedances

	Impedance	**Γ**	
Z	L/C Value	900 MHz	2.4 GHz
Z_0	1.5 pF	-0.60 - j0.52	-0.05 + j0.45
Z_1	20 nH	0.01 - j0.75	0.36 - j0.40
Z_2	8.4 pF	-0.68 + j0.25	-0.26 - j0.55
Z_3	3.3 nH	0.55 + j0.26	-0.50 - j0.24

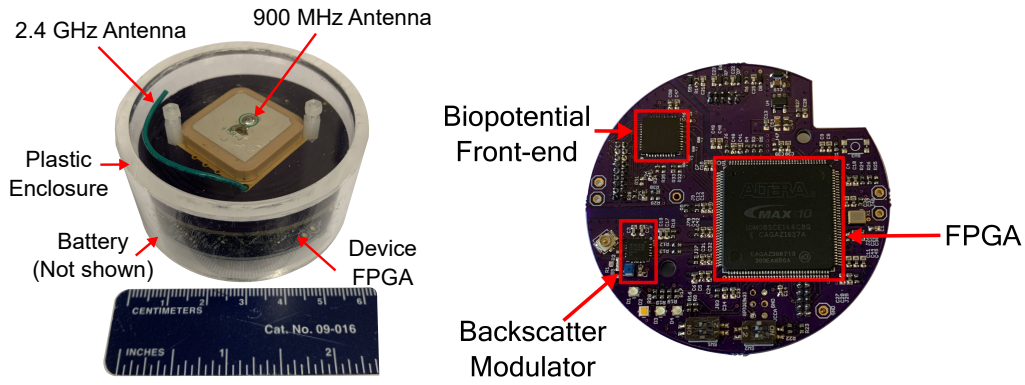

Figure 4.2: (a) Photo of the NeuroDisc stack in a plastic enclosure (b) Photo of the NeuroDisc FPGA printed circuit board. The same harware from Chapters 2 and 3 was used.

4.2 Dual-Mode NeuroDisc Overview

The dual-mode wireless backscatter uplink presented in this chapter was designed for the NeuroDisc brain-computer interface, an FPGA-based neural recorder that can measure microvolt-scale electrophysiological signals and wirelessly uplink data via a switched-impedance backscatter modulator. A photo of the complete NeuroDisc version used for this chapter is shown in Fig. 4.2a with a zoomed-in photo of the FPGA circuit board shown in Fig. 4.2b. The FPGA provides the high-speed digital logic required to sample and process multiple neural channels with high temporal resolution. The NeuroDiscs command and data handling functionality is implemented on an Altera MAX10 FPGA using approximately 5600 logic elements, internal non-volatile SRAM, and a 100 MHz clock, as shown in Fig. 4.3. The specific FPGA and oscillator were chosen to facilitate prototyping, and therefore are not the optimal choices for small size and low power consumption. Future revisions of the NeuroDisc could use a smaller FPGA and lower-power oscillator, such as a Lattice Semiconductor iCE40 FPGA. Eventually, the HDL code could be synthesized in an application-specific integrated circuit for further reduction of size and power consumption.

The NeuroDiscs biopotential front-end uses an Intan RHS2116 integrated circuit that enables recording from up to 16 electrophysiological channels with 16-bit resolution at up to 20 kSamples/s per channel. The backscatter modulator is comprised of an Analog Devices ADG904 single-pole-four-throw (SP4T) RF switch and four discrete reactive elements (two capacitors and two inductors) whose values are provided in Table 4.1. The RF switch connects to the NeuroDiscs antenna via a UMCC coaxial connector. Using an SP4T RF switch for the backscatter modulator enables the realization of two backscatter modulation schemes, quadrature phase-shift keying (QPSK) and single sideband (SSB) frequency-shift keying (FSK), without modification to the NeuroDisc hardware.

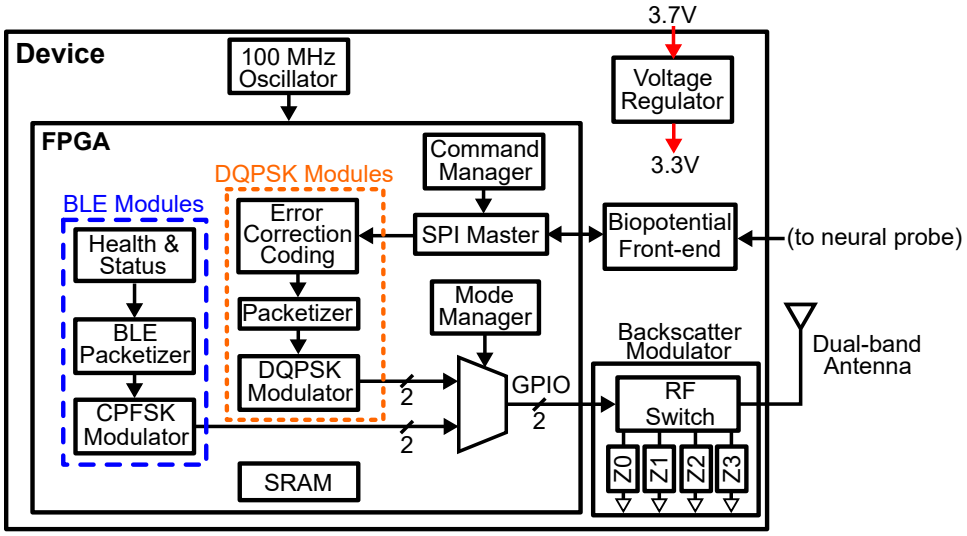

Figure 4.3: Block diagram of the FPGA-based digital logic

4.3 Dual-Protocol Backscatter Uplink

A dual-protocol, time-division-multiplexed backscatter uplink was implemented on the NeuroDisc, as shown in Fig. 4.4. The uplink is comprised of a custom 900 MHz 6.25 Mbps differential-QPSK (DQPSK) protocol and a 2.4 GHz 1.0 Mbps SSB Bluetooth Low Energy (BLE)-compatible protocol, both implemented using the Verilog hardware description language. A unique feature of this system is that both protocols share the same backscatter modulator and discrete impedances. By sharing the backscatter modulator, the size, weight, power consumption, and overall complexity of the circuit are reduced. If commercially-available active radios were used instead, the system would likely incur significant increases in cost, complexity, and power consumption. The power consumption of the RF switch was measured using a Keithley source-measure unit (SMU). During transmission of DQPSK packets, the power consumption is 77.5 μW, yielding a per-bit energy efficiency of 12.4 pJ/bit. During transmission of the BLE packets, the power consumption is 198 μW, yielding a per-bit energy efficiency of 198 pJ/bit.

4.3.1 DQPSK Mode Overview

The DQPSK mode is designed for operation in the 900 MHz North American industrial, scientific, and medical (ISM) band. DQPSK modulation was chosen because it enables two bits to be transmitted for every one symbol, increasing the data rate while reducing switching frequencies and power consumption. To implement DQPSK modulation in a backscatter communication system, four load impedances can be selected to generate four unique, complex-valued reflection coefficients. Oscilloscope measurements of the DQPSK signals used to actuate the RF switch are shown in

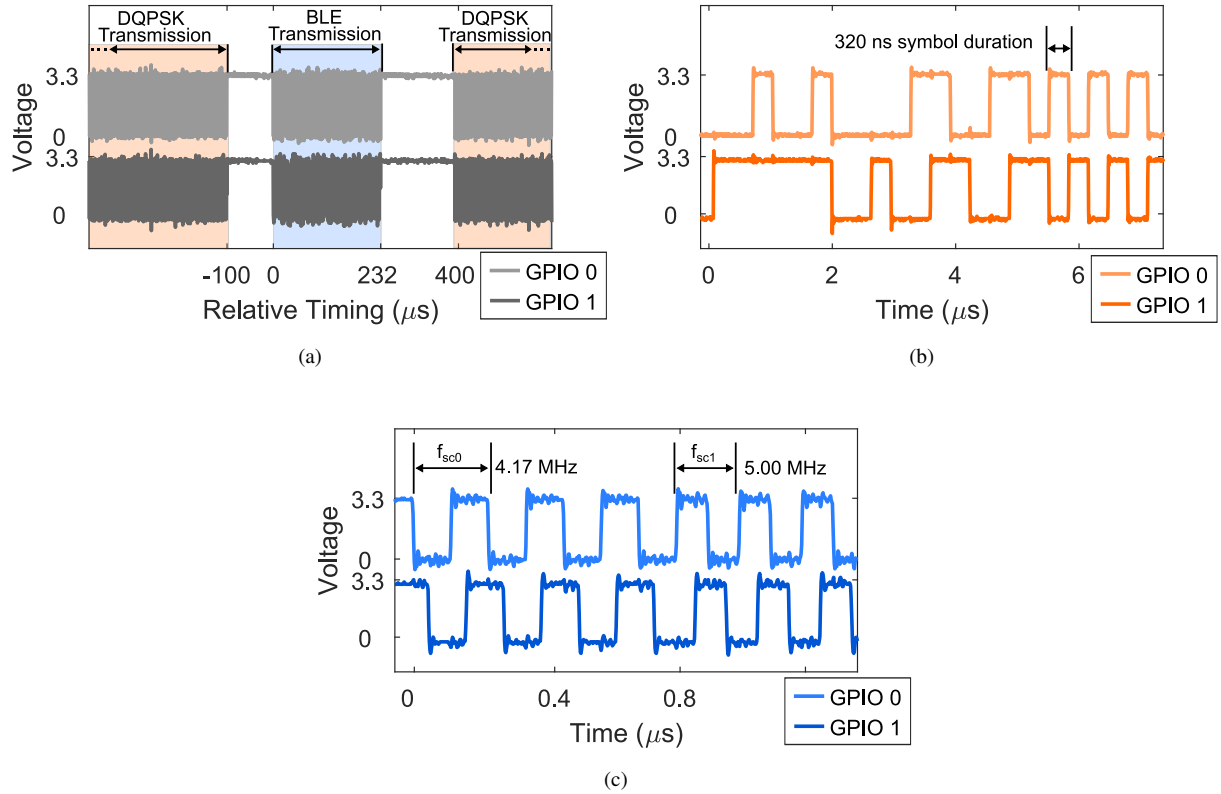

Figure 4.4: Oscilloscope measurements illustrate how the FPGA's backscatter modulator control signals, GPIO 0 and 1, are used to transmit DQPSK and BLE packets: (a) Plot showing how BLE packets are transmitted in-between DQPSK packets, (b) Zoomed-in plot of the DQPSK control signals showing a minimum symbol duration of 320 ns, yielding a symbol rate of 3.125 MSymbols/s, and (c) Zoomed-in plot of the BLE control signals showing the two subcarrier frequencies, f_{sc0} and f_{sc1}.

Fig. 4.4b, while additional details about implementing DQPSK backscatter modulation can be found in [16].

The DQPSK mode transmits data using a custom packet structure. One 1024-bit packet is transmitted every 800 μs at a symbol rate of 3.125 MSymbols/s (Fig. 4.4b). Each packet includes 528 bits of biological data from the biopotential front-end, and these bits are encoded with a Hamming(11,16) error correction code to form 48-bit frames (generally, one frame corresponds to one channel of measured biological data). A 16-bit frame marker precedes each 48-bit frame to facilitate processing at the receiver, yielding a total packet length of 1024 bits.

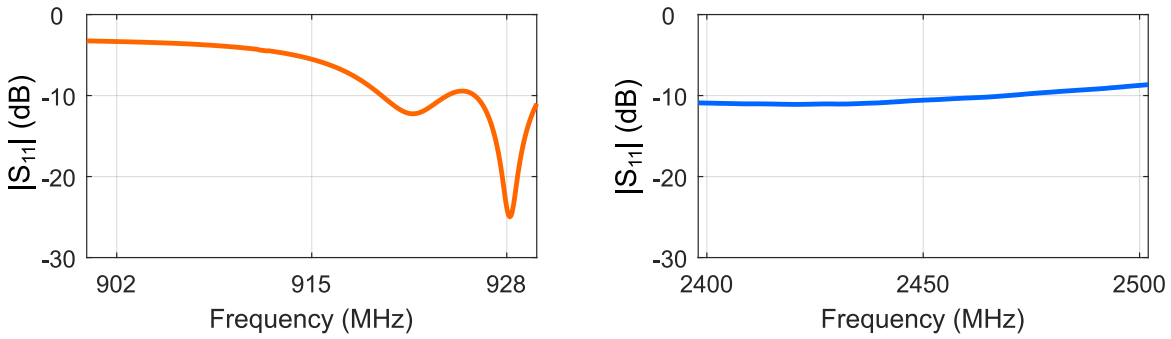

Figure 4.5: Vector network analyzer (VNA) measurement of S_{11} for the dual-band antenna in the (a) 900 MHz ISM band and (b) the 2.4 GHz ISM band.

4.3.2 BLE Mode Overview

The BLE backscatter uplink transmits BLE-compatible advertising packets in the 2.4 GHz ISM band. This mode generates a 1.0 Mbps frequency-shift keying (FSK) modulation process with a frequency deviation of 830 kHz in compliance with the BLE physical layer specification which requires a frequency deviation between 370 kHz and 1 MHz. FSK modulation is implemented on the NeuroDisc by switching between two or more load impedances at a frequency that is modulated by the data bits. Specifically two subcarrier frequencies, f_{sc0} = 4.17 MHz and f_{sc1} = 5.00 MHz, are used to transmit logic levels 0 and 1, respectively. On the NeuroDisc, these subcarrier frequencies are output on two GPIO pins and used to actuate the RF switch, as shown in Fig. 4.3. Oscilloscope measurements of the subcarrier signals are shown in Fig. 4.4c. To improve the in-channel signal strength and reduce out-of-channel emissions, the BLE backscatter uplink uses single sideband (SSB) modulation [46, 71]. The SSB modulation is implemented in the continuous-phase FSK (CPFSK) modulator block shown in Fig. 4.3. Additional details about implementing SSB BLE backscatter modulation can be found in [46].

The BLE mode transmits data using advertising packets. Advertising packets are used by BLE devices to broadcast data to nearby BLE receivers without requiring connection, making them well-suited for a unidirectional backscatter uplink. The NeuroDisc advertising packets carry 64 bits of payload data, yielding a total packet length of 232 bits when the required packet preamble, headers and cyclic redundancy check are included. The commercial BLE receivers we tested began dropping packets at packet rates over 500 packets/s since that exceeds the BLE specified advertising packet rate. Given this constraint, the NeuroDisc was configured to transmit single BLE advertising packets between DQPSK packet transmissions at a rate of 500 packets per second, yielding an effective throughput of 148 kbps via BLE.

4.3.3 Time-Division Multiplexing

Time-division multiplexing was used to achieve high overall data rates, high reliability, and low power consumption. The BLE protocol is designed around a time-division multiple access approach using a randomized ALOHA approach for advertising packets. Given the relatively long intervals between BLE packets (¿2 ms) and the relatively short duration of BLE packets (232 μs) configuring the BCI for time-division multiplexing was a logical choice for sharing a backscatter channel among two protocols. Oscilloscope plots of the backscatter modulator control signals in Fig. 4.4 illustrate how BLE packets are sent during gaps between DQPSK transmissions. Other channel access methods, such as frequency-division multiplexing, are discussed in Section V.

4.3.4 Dual-Band Antenna

The NeuroDiscs dual-protocol uplink requires an antenna that is resonant in both the 900 MHz and 2.4 GHz frequency bands. To meet this requirement, two different antennas were integrated into a single assembly. A 900 MHz commercial off-the-shelf ceramic patch antenna (Abracon APAE915R2540ABDB1-T) was mounted to a circular 5 cm-diameter printed circuit board (PCB). On the bottom layer of the PCB, the antenna feed pin connects to a UMCC coaxial connector via a balanced-unbalanced transformer. To achieve dual-band functionality, a 2.4 GHz monopole antenna was added to the antenna PCB by soldering a 6 cm-long piece of 24 AWG wire to the RF signal trace of the PCB. The return loss of the dual-band antenna was measured using an Agilent N5222A vector network analyzer, with the measurements plotted in Fig. 4.5. The antenna achieves a 10 dB return loss bandwidth of 6 MHz in the 900 MHz band with a center frequency of 928.2 MHz, and 70 MHz bandwidth in the 2.4 GHz band, with a center frequency of 2.435 GHz.

4.3.5 Impedance Constellation Design

To implement QPSK and SSB FSK backscatter communication, a system must be able to present at least four unique impedances to its antenna [16, 46]. Since the NeuroDisc uses an SP4T RF switch as its backscatter modulator, four discrete impedances outlined in Table 4.1 were chosen to generate four reflection coefficients in separate quadrants of the Smith chart with approximately the same magnitude. The components were initially selected for use in the 900 MHz ISM band, although as the vector network analyzer measurements in Fig. 4.6 show, the resulting reflection coefficients are suitable for use in the 2.4 GHz ISM band as well.

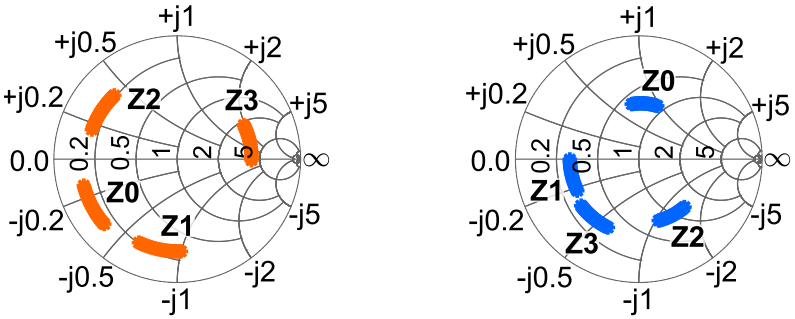

Figure 4.6: Smith chart showing the measured reflection coefficients of the backscatter modulator for (a) the 900 MHz ISM band and (b) the 2.4 GHz ISM band.

4.4 Measurements & Results

4.4.1 Cabled Measurements

The power spectrum of the DQPSK and SSB BLE backscatter uplinks were measured using the cabled setup shown in Fig. 4.7a. An RF signal generator was used as the CW source and an Agilent N9320B spectrum analyzer was used to make the measurement. Fig. 4.7b shows the spectrum of the custom DQPSK uplink. The asymmetry of the spectrum is a result of the transmitted data having structure, which could be removed with the application of a data whitening filter. Fig. 4.7c shows the spectrum of the SSB BLE backscatter uplink. The plot shows the lower sideband (LSB) approximately centered about f_{cw}-4.5 MHz and the upper sideband (USB) approximately centered about f_{cw}+4.5 MHz. The LSB was selected as the desired sideband, providing a measured gain of 2.8 dB in the LSB and an attenuation of 7.2 dB in the unwanted USB, yielding a total sideband rejection ratio of 10 dB.

4.4.2 Over-the-air Validation Measurements

Wireless, over-the-air validation measurements were performed using the test setup shown in Fig. 4.1b. Previous work in [19] and [53] found that 900 MHz DQPSK and 2.4 GHz BLE backscatter uplinks could successfully communicate to a receiver mounted on the top inner panel of the cage from nearly all locations inside a typical non-human primate cage. These works measured the channel transfer function for each frequency band at different locations and orientations and conducted packet error tests to verify the integrity of the wireless link. To maintain consistency with the measurements in [19, 53], an animal cage was used to house the NeuroDisc to approximate a non-human primate's home cage where wireless electrophysiology experiments would likely be performed. The NeuroDisc was similarly placed on a tissue

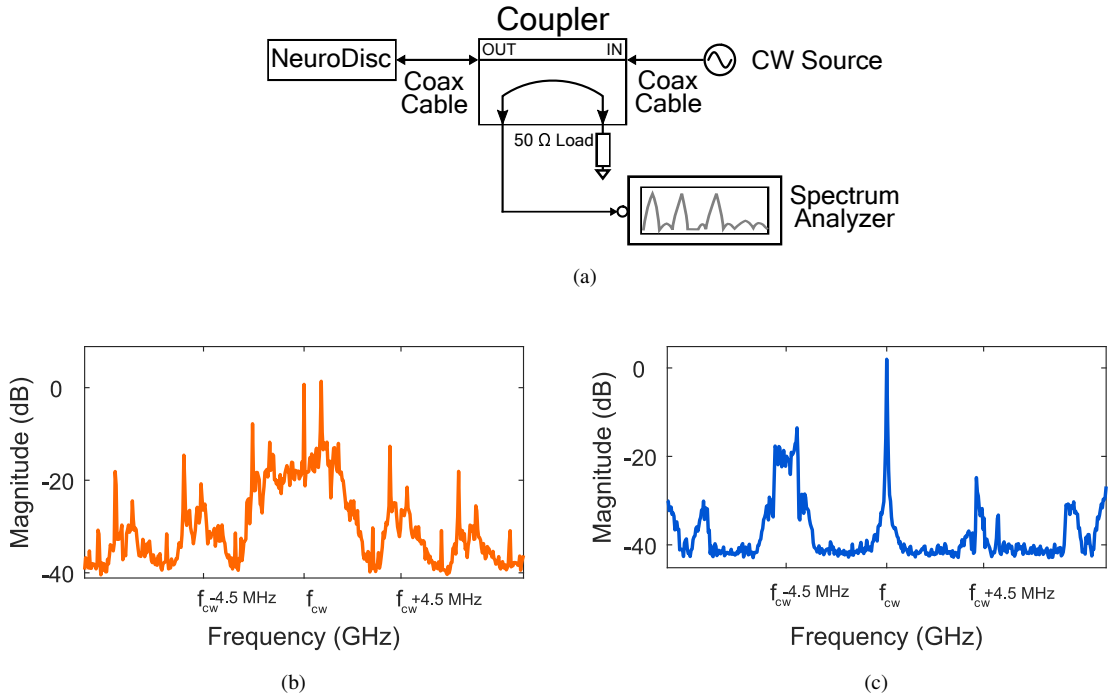

Figure 4.7: (a) Block diagram of cabled measurement setup (b) Plot of the measured spectrum for DQPSK packets (c) Plot of the measured spectrum for SSB BLE packets.

phantom comprised of a plastic container filled with approximately 1 liter of saline solution to account for the effects of a monkey on the antenna radiation pattern and the channel propagation characteristics. Mounted to the top, inner wall of the cage were a 900 MHz right-hand circularly polarized patch antenna (Laird Technologies) and a 2.4 GHz linearly polarized patch antenna (L-Com). The 900 MHz antenna was connected to a custom, software defined radio-based, full-duplex DQPSK receiver based on the design in [16]. The 2.4 GHz antenna was connected to an RF signal generator and RF amplifier to broadcast a CW carrier at 15 dBm.

To mimic the uplink of biological data, the DQPSK protocol was used to transmit a 20 kSamples/s sampled 180 Hz sine wave stored in the FPGA. The 180 Hz sine wave was chosen because it is in-band with respect to the desired neural data. A plot of the received data is shown in Fig. 4.8a. The SSB BLE protocol was then used transmit health and status data from the FPGA, in this case including an 8-digit packet counter, as shown in Fig. 4.8b. An unmodified iPhone, iPad, and Nordic Semiconductor nRF51822 BLE development board were then used to validate successful reception of the SSB BLE backscatter packets. Data from both protocols could be successfully received and decoded effectively simultaneously from the perspective of the user due to the tight interleaving of both communication modes. Because of the interleaved packet structure, the different symbol rates, and the different backscattered spectra, the two modes do not create apparent interference between each other.

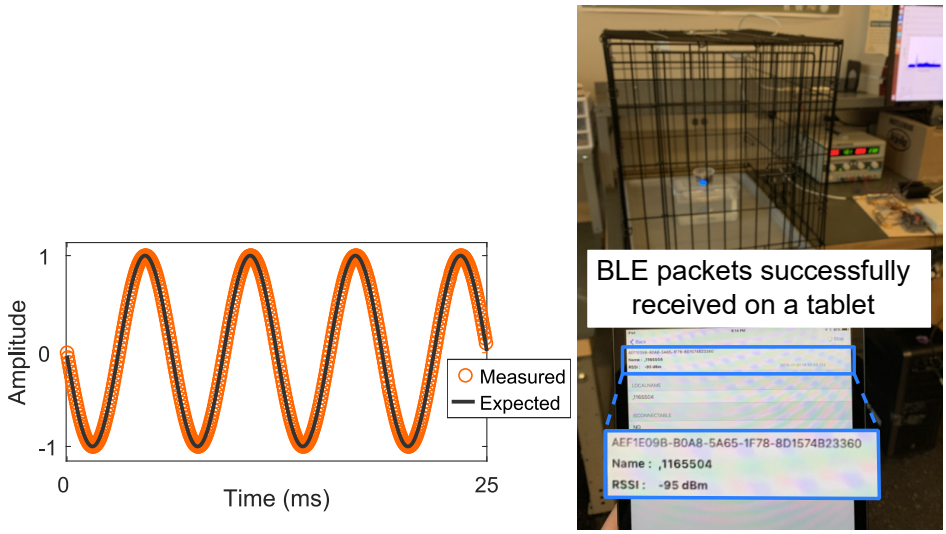

(a) (b)

Figure 4.8: Over-the-air validation experiment: (a) Plot of sine-wave test data received via the DQPSK uplink at 6.25 Mbps, and (b) Photo of BLE packets received on an Apple iPad at approximately 2 m from the animal cage.

4.5 Chapter Conclusions

This chapter presents a dual-band, dual-mode backscatter uplink leveraging shared hardware that combines a custom DQPSK mode at 900 MHz and a SSB BLE-compatible mode at 2.4 GHz. The DQPSK mode provides a data rate of 6.25 Mbps with a measured power consumption of 75 μW at the backscatter modulator, yielding a modulator efficiency of 12.4 pJ/bit. The SSB BLE-compatible mode provides a 1.0 Mbps data rate while consuming 198 μW at the backscatter modulator, yielding a modulator efficiency of 198 pJ/bit, which is >50X lower than most off-the-shelf BLE transmitters. The sideband rejection ratio was measured to be 10 dB, improving the in-channel signal strength and reducing out-of-channel emissions.

This system provides real-time neural data uplink across both the 900 MHz and 2.4 GHz ISM bands, which to the best of our knowledge is unique in the literature on wireless BCIs. The dual-band compatibility of the backscatter front-end provides end-users and researchers the ability to leverage frequency diversity depending on the communication channel, offering experimental flexibility that could be advantageous in commercial applications outside of neural engineering as well.

This work uses time-division multiplexing to switch between DQPSK and BLE transmissions. We believe that truly simultaneous transmission could be achieved with frequency-division multiple access by engineering the spectra of the DQPSK and CPFSK (BLE) modulations. Two methods could be considered: (1) The DQPSK symbol rate

could be modified to 1 MSymbol/s such that nulls in the spectrum occur at 1 MHz intervals. The CPFSK subcarrier frequencies could then be chosen so that they are still 1 MHz apart per the BLE specification while falling within the nulls of the DQPSK spectrum. The carrier wave generator for the CPFSK signal could be adjusted so that the backscatter signal aligns with one or more BLE advertising channel(s); and (2) the CPFSK subcarrier frequencies could be chosen such that they are far outside the DQPSK spectrum. This would require higher CPFSK subcarrier frequencies and a modest increase in power consumption at the backscatter modulator.

Chapter 5

PERFORMANCE OF BACKSCATTER COMMUNICATION SYSTEMS IN REVERBERANT CAVITY ANIMAL CAGE ENVIRONMENTS

Key point: When a radio transmitter is introduced into a metal cage, the radio waves reflect off the walls to form what is known as a reverberant cavity. The reflected waves constructively and destructively interfere at random locations in the cage, making it difficult to reliably transmit and receive radio signals. This chapter reveals that a metal non-human primate cage forms a reverberant cavity in the 2.4 GHz industrial, scientific, and medical (ISM) band. Despite the interference, we demonstrate that a 1.0 Mbps frequency shift keying (FSK) backscatter uplink can reliably uplink data throughout the cage volume with a worst-case packet error rate of 1.3%, translating to a bit error rate of 5.6×10^{-5}. This section is based on the work in [53], which built off previous experience characterizing and analyzing the channel transfer function of a cage presented in [19].

5.1 Introduction

While there is extensive literature on characterizing multipath channels in urban and indoor office environments, to the authors' knowledge, this was the first characterization of the channel transfer function (CTF) for the 2.4 GHz microwave ISM bands inside of a metal primate cage. Further, we demonstrated that under ideal conditions, backscatter communication systems can perform well inside of a metal primate cage despite the significant multipath inside the reverberant cage environment. This chapter presents test results of a backscatter data uplink system designed for the NeuroDisc BCI operating within an NHP cage and using a BLE-compatible backscatter uplink in the 2.4 GHz ISM band.

5.2 Overview of the CTF Measurements

5.2.1 Experimental Setup

The NHP cage depicted in Fig. 5.1 was used for the experiments in the 2.4 GHz ISM band. The cage is divided into two chambers (top and bottom) by a horizontal metal grating. Measurements were conducted in the lower chamber of the cage with dimensions of 93 cm $\times$ 93.4 cm $\times$ 77 cm (height $\times$ width $\times$ length). All the walls of the cage are made with a square metal mesh with a mean gap of 2.5 cm. The gap is approximately 5 times smaller than the shortest wavelength of 12 cm in the 2.4 GHz band. However, the cage is not a perfectly enclosed EM cavity, because one of the vertical walls of the cage contains a clear polycarbonate window with dimensions of 60.7 cm $\times$ 23.4 cm

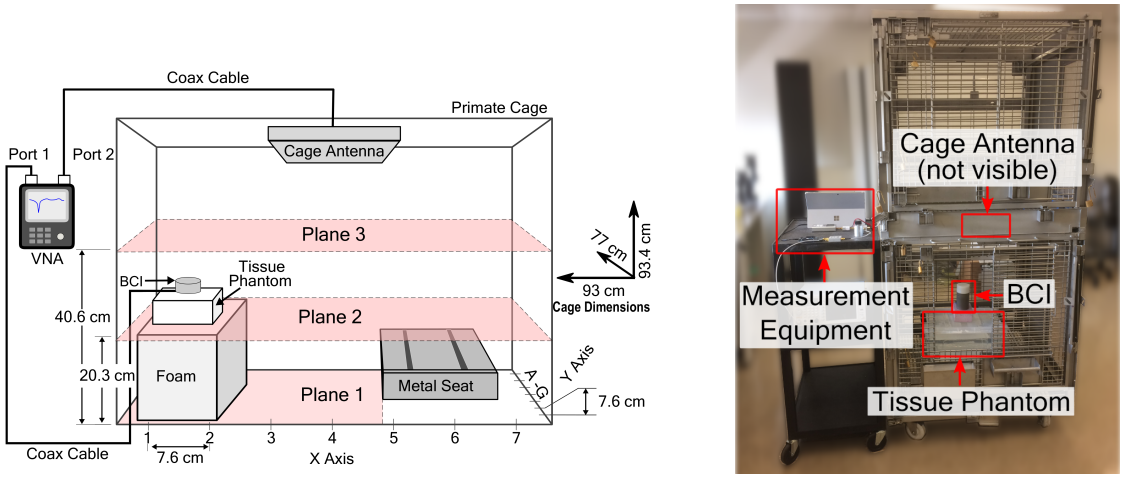

(a) (b)

Figure 5.1: (a) Block diagram. (b) Photo of the test setup used to characterize the wireless channel of the non-human primate cage for the 2.4 GHz ISM band.

(length $\times$ width) through which EM waves may propagate. Finally, the cage contains a metal seat for the NHPs with a width of 18 cm and a height of 15 cm.

A saline tissue phantom was used to simulate the body of a male macaque monkey weighing 7 kg on average; this species is frequently used in neural plasticity experiments [12]. The phantom consists of a plastic container with dimensions of 41.8 cm $\times$ 27.8 cm $\times$ 16.5 cm (length $\times$ width $\times$ height) and contains 7 L of saline solution with 0.91 g sodium chloride (NaCl) per liter of distilled water [10]. The BCI was placed on the top of the plastic container. The BCI antenna was connected to port 1 of a Keysight FieldFox vector network analyzer (VNA) with a coaxial cable, and the cage antenna was connected to port 2 of the VNA with another coaxial cable. We performed a two-port calibration of the coaxial cables and VNA prior to measurement. To further mitigate cable effects, we routed the cables away from the direct path between the antennas and perpendicular to the antenna plane as much as possible, routing the cable along the metal cage walls.

The antenna performance was measured at a total of 126 total locations across 3 measurement planes: 28 locations on Plane 1, 49 locations on Plane 2, and 49 locations on Plane 3. The grid spacing was 7.6 cm, with the x-axis labelled A through G and the y-axis labelled 1-7. The vertical spacing was 20.3 cm, labelled Measurement Plane 1, Plane 2, and Plane 3. An RF-transparent Styrofoam was used in order to raise the tissue phantom and BCI to the appropriate elevations of Measurement Plane 2 and 3. Columns 5-7 on the bottom measurement plane (Plane 1) were unusable due to the NHP bench height.

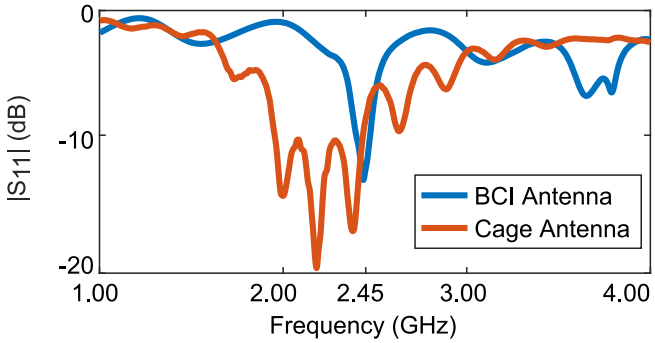

Figure 5.2: Measured return loss of the 2.4 GHz BCI antenna and the cage antenna, outside of the cage environment.

Antennas

The custom antenna used for this work was designed and simulated by Apoorva Sharma. Additional details and analysis can be found in her dissertation [57].

2.4 GHz Cage Antenna

The 2.4 GHz cage antenna was affixed on the inside of the mesh wall separating upper and lower chambers of the NHP, as shown in Fig. 5.1. An L-Com Inc. 2.4 GHz 8 dBi right-hand circularly polarized (RHCP) patch antenna selected for the cage antenna was connected to port 2 of the VNA. Circular polarization was employed to reduce polarization mismatch since an NHP may position itself in any orientation relative to the cage antenna. The cage antenna has overall dimensions of 2.3 cm $\times$ 11.6 cm $\times$ 11.6 cm (length $\times$ width $\times$ height).

2.4 GHz BCI Antenna

In our experiments, we used the NeuroDisc BCI which consists of a 2.4 GHz BCI antenna, backscatter modulator, communications FPGA, and battery within a plastic housing (Fig. 2.1a). The BCI antenna was a semi-custom design consisting of a circular, 5.5 cm diameter, two-layer FR-4 PCB with 1.6 mm dielectric thickness and 30μ copper trace thickness. The top side of the BCI antenna PCB contained a centered, circularly shaped ground plane and a Tagolas Inc. WLP.2450 ceramic patch element with dimensions 2.5 cm $\times$ 2.5 cm $\times$ 0.4 cm. The bottom side of the PCB contained a balun transformer and a UMC coaxial connector. The measured return loss of this antenna is plotted in Fig. 5.2.

5.3 CTF Measurement Results

The insertion loss and usable bandwidth data reveal a dense multipath environment inside the NHP cage. The results show that the widest bandwidth and minimum insertion losses occurred in the area directly underneath the receiving

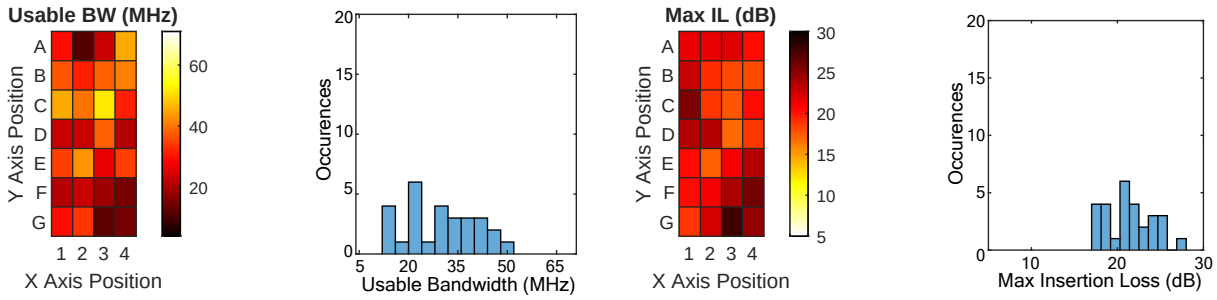

(a) (b) (c) (d)

Figure 5.3: 2.4 GHz ISM Band Experimental results at Measurement Plane 1. (a) Heatmap. (b) Histogram of usable bandwidth. (c) Heatmap. (D) Histogram of maximum insertion loss. In all heatmap images, darker colors indicate worse performance.

antenna, with the narrowest bandwidths and maximum losses near the outside corners.

5.3.1 2.4 GHz ISM Band Channel Transfer Function Measurements

The measured insertion loss and "usable bandwidth" (3 dB bandwidth) are presented in the heatmaps and histograms of Figs. 5.3, 5.4, and 5.5, as summarized in Table 5.1. The widest usable bandwidths and best case insertion loss occurred on Measurement Plane 3, and positions near the middle of the cage tended to have wider usable bandwidths and lower maximum insertion losses compared to positions at the edges of the cage. The minimum usable bandwidth across all 126 locations was 5.0 MHz, with means of 33 MHz, 30.6 MHz, and 28.7 MHz on Measurement Plane 1, 2, and 3, respectively. The maximum insertion loss across all 126 locations was 27.4 dB, with means of 19.4 dB, 17.0 dB, and 8.8 dB on Measurement Plane 1, 2, and 3, respectively.

5.3.2 Discussion of 2.4 GHz Channel Transfer Function Measurements

These measurements in the 2.4 GHz ISM band show approximately a 10 dB reduction in insertion loss compared to the the 915 MHz ISM band [19]. These measurements suggest that it is essential for system designers to consider the deep nulls that result when designing a communication system to operate inside of the cavity formed by an animal cage. For this work we chose to use BLE advertising packets that use 1 MHz bandwidth communication channels with frequency diversity provided by the three distinct advertising channels. In the case of BLE uplinks, deep nulls due to multipath interference can be mitigated by leveraging the frequency diversity between the three advertising channels prescribed by the BLE standard and/or dynamically changing the center frequency of the external carrier wave and the relative subcarrier frequency deviations. For other communication standards, channel equalization techniques could be employed at the cost of greater complexity and higher overall system power consumption.

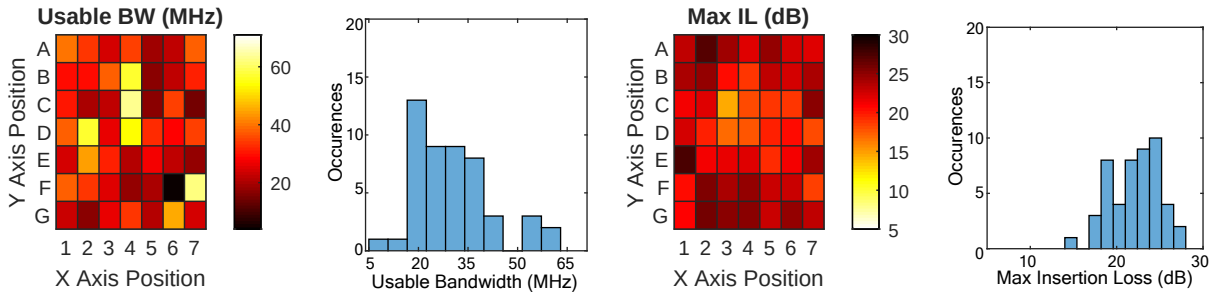

Figure 5.4: 2.4 GHz ISM Band Experimental results at Measurement Plane 2. (a) Heatmap. (b) Histogram of usable bandwidth. (c) Heatmap. (D) Histogram of maximum insertion loss. In all heatmap images, darker colors indicate worse performance.

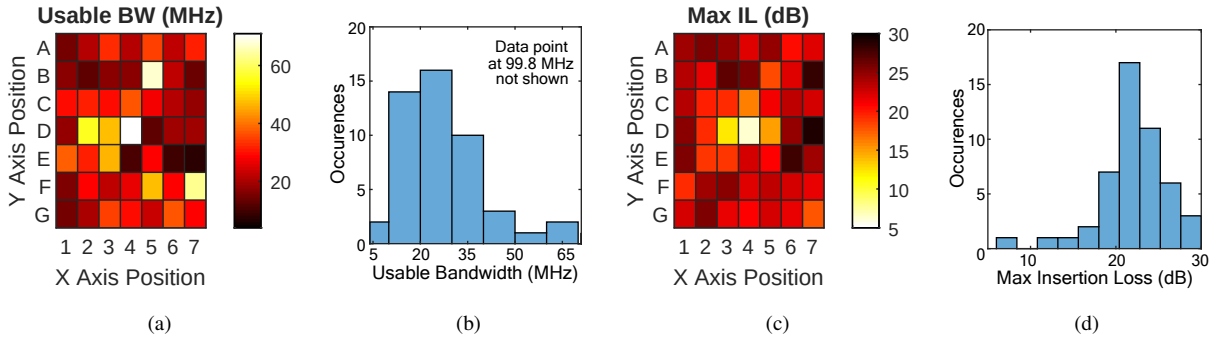

Figure 5.5: 2.4 GHz ISM Band Experimental results at Measurement Plane 3. (a) Heatmap. (b) Histogram of usable bandwidth. (c) Heatmap. (D) Histogram of maximum insertion loss. In all heatmap images, darker colors indicate worse performance.

5.4 Link Reliability Measurements within the Cage Environment

5.4.1 Link budget characterization

The round-trip link budget for this system can be described as follows

$$P_R = P_C + 2 \times S_{21} + M \tag{5.1}$$

where P_R is the received power at the cage-side antenna in dBm, P_C denotes the CW power from the cage antenna, and M is a modulation factor imposed by the symbol-dependent change in modulator impedance as seen by the NeuroDisc

Table 5.1: 2.4 GHz CTF measurements summary

	Measurement Plane		
	Plane 1	Plane 2	Plane 3
Minimum Usable BW (MHz)	12.1	5.0	8.1
Mean Usable BW (MHz)	33.3	30.6	28.7
Maximum Insertion Loss (dB)	26.0	27.4	27.4
Mean Insertion Loss (dB)	19.4	17.0	8.8

antenna (akin to the free-space differential radar cross-section), and is defined as $M = \frac{1}{4}|\Gamma_a - \Gamma_b|^2$, where $\Gamma_{a,b}$ is the reflection coefficient of the antenna for state A or state B [44, 82]. We calculated $M = -5$ dB. Based on these calculations and the specified sensitivity of the BLE receiver (-92 dBm), any insertion loss higher than 51 dB will result in a 100% PER.

5.4.2 PER measurements in the NHP cage

BLE Advertising Requirements

The BLE standard is well suited for unidirectional backscatter uplinks because the BLE protocol supports an "Advertising" mode where devices broadcast data packets without being required to receive. The physical-layer communication protocol is defined in the BLE v4.0 specification and requires that data be transmitted at 1.0 Msymbol/sec on one of three advertising channels (CH37 at 2.402 GHz, CH38 at 2.426 GHz, and CH39 at 2.480 GHz). Data bits are modulated using FSK modulation with frequency deviations between 185 kHz to 500 kHz. A binary 'one' is sent by shifting the FSK subcarrier above the channel's center frequency and a binary 'zero' by shifting the FSK subcarrier below the channel center. Data is formatted into advertising packets that include a 24-bit cyclic redundancy check (CRC) and channel-dependent data whitening, as specified in the BLE v4.0 specification and shown in Fig. 5.6.

BLE Receiver System

A BLE-compatible backscatter communication system was developed based on work presented in [45]. A Nordic Semiconductor nRF51822 Development Kit (DK) was used as the receiver. The nRF51822 is a commercially-available integrated system-on-chip for BLE applications. An SMA connector was soldered onto the nRF51822 DK to connect the cage antenna to the device; no other modifications were made to the hardware or firmware. The nRF51822 DK was programmed with Nordic Semiconductor's "nRF sniffer" BLE development firmware that allows the device to transfer data packets via USB to a PC running Wireshark, an open-source packet analyzer software package. Received BLE packets were then parsed and analyzed using Matlab 2018a software (MathWorks, Inc.). All hardware and software

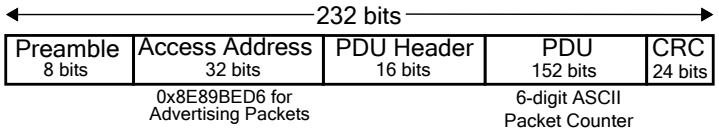

Figure 5.6: Overview of the BLE advertising packet structure with the custom packet counter.

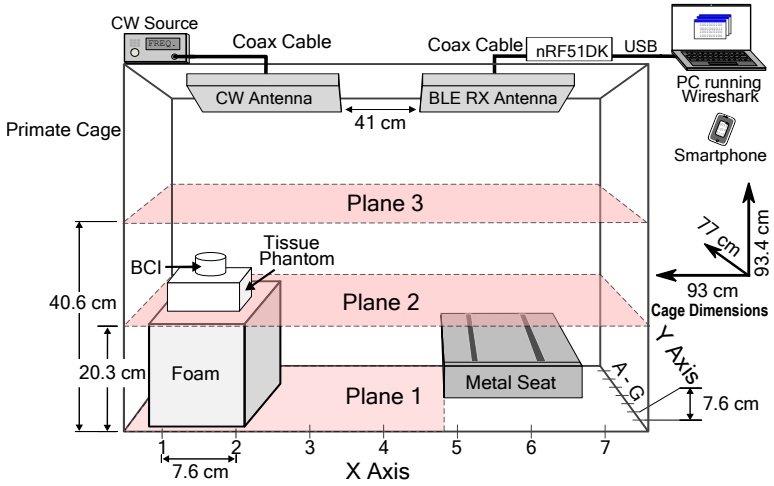

Figure 5.7: Block diagram of the test setup used to characterize the wireless BLE backscatter uplink inside the NHP cage.

Table 5.2: Summary of the packet error rate (PER) measurements

	Measurement Plane		
	Plane 1	Plane 2	Plane 3
Best-Case PER	0.32% (CH39)	0.27% (CH39)	0.33% (CH39)
Worst-Case PER	1.29% (CH37)	1.03% (CH37)	1.05% (CH37)
Mean PER	0.69%	0.60%	0.69%

used for the receiver could be implemented using a commodity BLE receivers (e.g. smartphones, tablets, laptops) and open-source software platforms (e.g. Android SDK). No hardware or firmware modifications are required because the backscatter signals are fully BLE compatible.

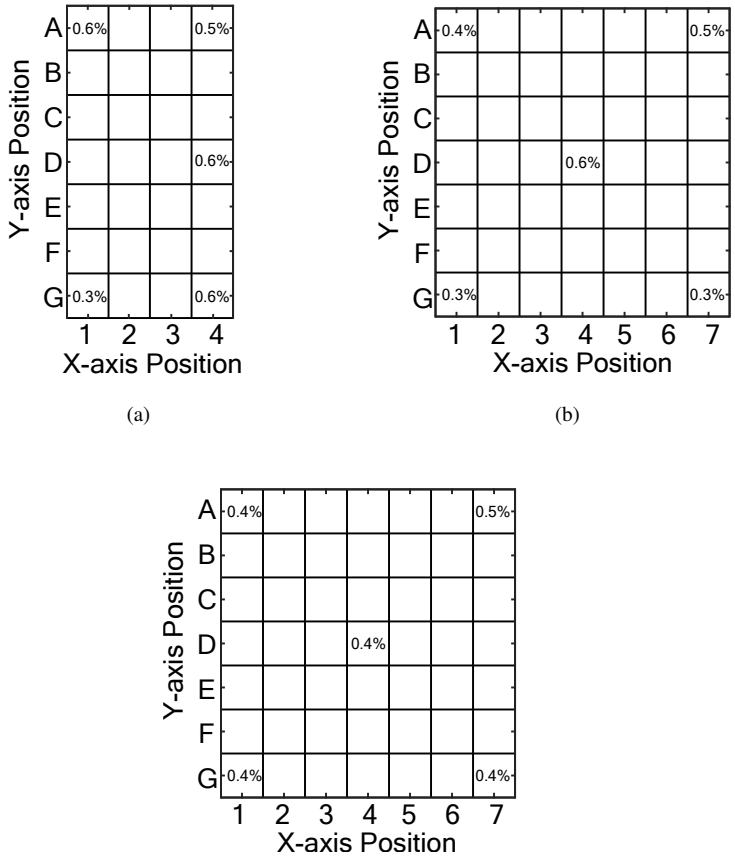

Figure 5.8: Mean BLE packet error rate (PER) measurements across all three channels for (a) Measurement Plane 1, (b) Plane 2, and (c) Plane 3 inside the NHP cage. At each measurement location, $\geq$5800 packets were transmitted, corresponding to a minimum of 1.35×10^6 bits. Measurements from all planes indicate a worst-case PER of $<$1.3 %.

Experimental Setup

A bistatic BLE backscatter system was set up around the NHP cage to evaluate the backscatter uplink performance, as shown in Fig. 5.7. A carrier wave (CW) source antenna and a BLE receiver (BLE RX) antenna were mounted to the center of the top of the cage, separated by 41 cm. Identical L-Com 2.4 GHz 8 dBi RHCP antennas were used for both the CW source and the BLE RX. The CW antenna was connected to an RF Explorer signal generator (Seeed Studio Co. Ltd.) and a PE1516 amplifier (Pasternack Enterprises, Inc.) that supplied a total CW power of +15 dBm. The NeuroDisc BCI with a BLE-compatible backscatter uplink FPGA code was then moved to various measurement locations within the cage. The NeuroDisc device was configured to transmit a packet counter on each

of the three advertising channels allocated by the BLE 4.0 specification. Packet error rate (PER) was then estimated by dividing the number of dropped packets by the total number of packets transmitted, as indicated by the packet counter (Fig. 5.6). A minimum of 5800 packets were collected for each test, providing more than 1.34×10^6 bits per measurement location. Any packet that failed a CRC check was marked as a packet error.

To evaluate the PER performance, five points were chosen on each measurement plane, and PER was measured on each of the three BLE advertising channels, for 45 total measurements. Due to the metal seat inside the cage, PER measurements were made at locations B2, F2, B4, D4, and F4 for Measurement Plane 1 while PER measurements were made at locations B2, F2, D4, B6, and F6 for Measurement Planes 2 and 3 (Fig. 5.7).

Experimental Results

The PER performance of the BLE-compatible backscatter uplink is summarized in Fig. 5.8 and in Table 5.2. We found Channel 39 to have the lowest PER across all testing locations; Channels 38 and 39 had less than 1% PER across all testing locations, ranging from a best case of 0.27% to a worst case of 0.92% with a mean PER of 0.58%. Channel 37 had the highest PER with a best case of 0.46%, a worst case of 1.29%, and mean of 0.80%.

Across all three advertising channels, the best- to worst-case PERs were 0.32% to 1.29%, 0.27% to 1.03%, and 0.33% to 1.05% for Measurement Planes 1, 2, and 3 respectively. Mean PERs were 0.69%, 0.60%, and 0.69% for Planes 1, 2, and 3 respectively. The NHP cage appeared to function as a chaotic cavity with no obvious pattern to where the best- and worst-case scenarios occurred. Additionally, because the wire mesh cage did not form a complete Faraday cage, we observed that an unmodified smartphone could receive the backscattered packets from outside the cage at a distance of 2-3 meters, as shown in Fig. 5.9. The low PER values match our expectations given that the insertion loss at all points was well below the calculated threshold of 51 dB. The reason for a non-zero PER may be due to interference in the 2.4 GHz ISM band from Wi-Fi and/or other BLE traffic. The experiments were performed in a laboratory environment on a university campus where Wi-Fi signals are always present and there can be dozens of BLE devices on at a single time, e.g. PCs, keyboards, computer mice, etc.

5.4.3 Discussion of Communication Link Integrity Measurements

A PER of $<1.3\%$ across all measurement locations and all channels inside the cage demonstrate the viability of using ultra-low-power BLE-compatible backscatter to uplink biotelemetry from freely moving animals in an unconstrained cage environment. If we assume that each packet error results from a single bit error, and that each error is independent, we can calculate the effective bit-error rate (BER) as

$$\text{BER} = 1 - (1 - \text{PER})^{\frac{1}{n}}, \tag{5.2}$$

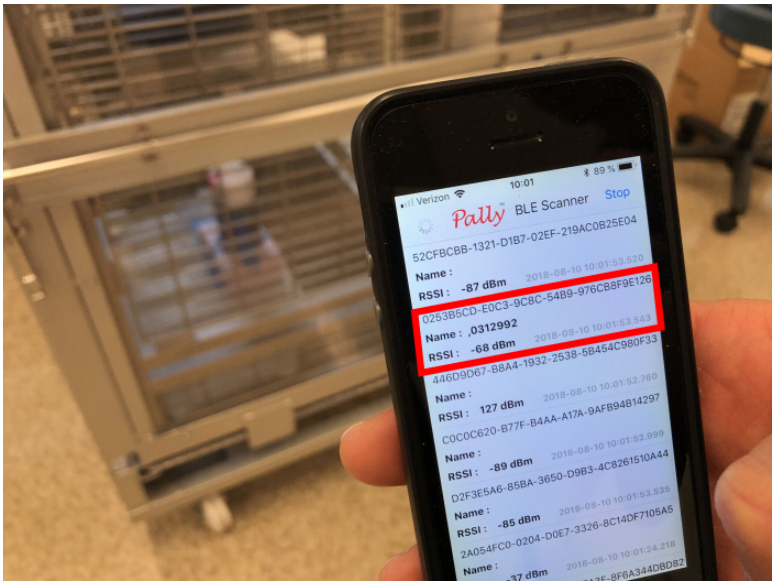

Figure 5.9: Photo of backscattered BLE advertising packets received by an unmodified smartphone outside of the cage.

where n is the number of bits per packet, in this case 232. From Eq. 5.2 we find the worst-case measured PER yields an effective BER of 5.6×10^{-5} which meets the BLE v4.0 specification requirement of BER $\leq 10^{-3}$.

5.5 Chapter Conclusions

This chapter provided measurements of the 2.4 GHz channel transfer function inside the reverberant cavity environment of a metal NHP home cage. Measurements taken in 3 measurement planes using a calibrated VNA indicate a mean insertion loss of 15.1 dB and a mean usable bandwidth of 30.9 MHz, suggesting that there is a larger usable bandwidth and less insertion loss at the 2.4 GHz ISM band inside of the cage than at the 915 MHz ISM band, as reported in [19].

Chapter 6

SWITCHED IMPEDANCE MODE STIRRING FOR REVERBERANT CAVITY ANIMAL CAGE ENVIRONMENTS

Key point: To reduce the effects of multipath interference on backscatter uplinks inside a metal non-human primate (NHP) cage, low-profile switched parasitic antennas (SPAs) can be mounted within the cage to alter the electromagnetic boundary conditions. Using this technique, the average power ratio between a BCI antenna and a ceiling-mounted cage antenna can be increased, creating a more favorable communication channel. This chapter presents experimental results showing that the use of SPAs improved the worst-case two-way insertion loss inside a metal NHP cage by up to 60.20 dB in the 915 MHz band and by up to 35.62 dB in the 2.4 GHz band. These reductions in insertion loss increase the channel link margin and the overall channel capacity for wireless uplinks.

This work has been submitted to *IEEE Transactions on Antennas and Propagation* and is currently under revision.

6.1 Introduction

The improved energy efficiency of backscatter communication comes at the cost of a less favorable link budget compared to conventional radios. Because the externally-generated carrier wave travels a round trip from the external system to the backscatter radio and back, the RF power at the receiver changes as $1/r^4$ for a backscatter system, rather than the usual $1/r^2$ for conventional radios, where r is the free-space distance between the external system and the BCI antenna [43, 44]. Given the round-trip nature of the backscatter link budget, multipath inside the cage can significantly reduce the reliability of backscatter radios. Previous characterizations of the 915 MHz [19] and 2.4 GHz ISM bands [53] (Chapter 5 within NHP cages indicate that the metal walls form a reverberant cavity that exhibits deep nulls throughout the cage volume . These findings suggest that additional measures are needed to alleviate deep nulls in the channel transfer function (CTF).

Two main approaches have been explored to reduce or overcome multipath interference in a cage. In [83], a custom RF-transparent NHP cage was built and validated with simulations, measurements, and *in vivo* wireless measurements. Reducing the conductivity of the cage structure significantly improved wireless system performance, however, most RF-transparent materials are both much more expensive and less rugged than conventional metal cages. To avoid the spread of disease in animal care facilities, the animal cages must be frequently autoclaved and/or cleaned with reactive chemicals like bleach, both of which rapidly degrade RF-transparent plastics.

Other research has explored how antenna diversity at the external system and/or backscatter radio (e.g. in a MIMO

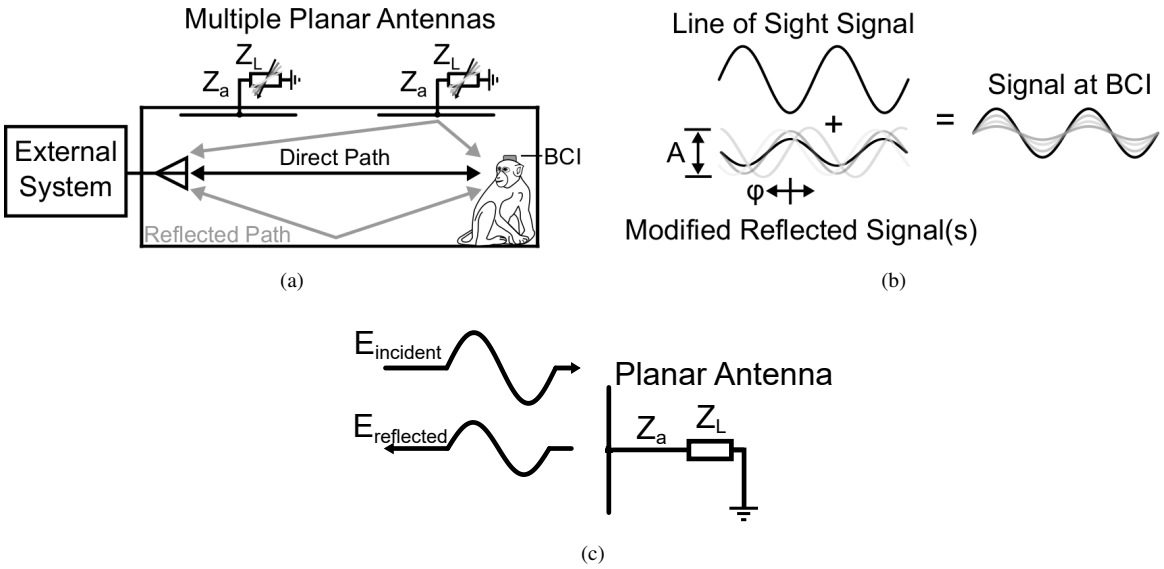

Figure 6.1: (a) Overview of the proposed electronic mode stirring technique, (b) Multipath produces destructive interference in certain locations throughout the animal cage. (c) Electronic mode stirring dynamically alters the amplitude and phase of reflection by controlling the impedance presented to a planar antenna.

system) can mitigate the effects of nulls [84–88]. These schemes depend on multiple antennas separated by one or more wavelengths to provide spatial diversity. However, diversity and MIMO approaches are often not suitable for biomedical applications where the device dimensions (typically 1-3 cm^3) are physically small relative to the operating wavelength of the wireless system. For small implantable devices in particular, the device size is so small that, even if multiple antennas were implemented, they would exhibit very high mutual coupling which would negate any advantage from a MIMO approach.

In this chapter, we present a different approach for mitigating multipath fading in a metal NHP cage via mode stirring. By altering the electromagnetic boundary conditions of the cage, nulls in the CTF can be reduced and a more favorable link budget achieved (Fig. 6.1(a)). Mode stirring is often used to improve the statistical uniformity of the electric field within reverberant cavities for electromagnetic compatibility and interference (EMI/EMC) testing [89]. It can be achieved via mechanical and electronic means, though mechanical mode stirring would be impractical for in-cage animal experiments because a reflector must be mechanically displaced, potentially interfering with the NHP. In contrast, electronic mode stirring using low profile antennas could enable control of the CTF without requiring intrusive structures. Electronic mode stirring has shown promising results for EMI/EMC applications, e.g. in [90], where reactively-loaded conical antennas were placed around the cavity to improve the field isotropy and homogeneity. The loads presented to the antennas were changed to modify the amplitude, A, and phase, ϕ, of the reflected electric

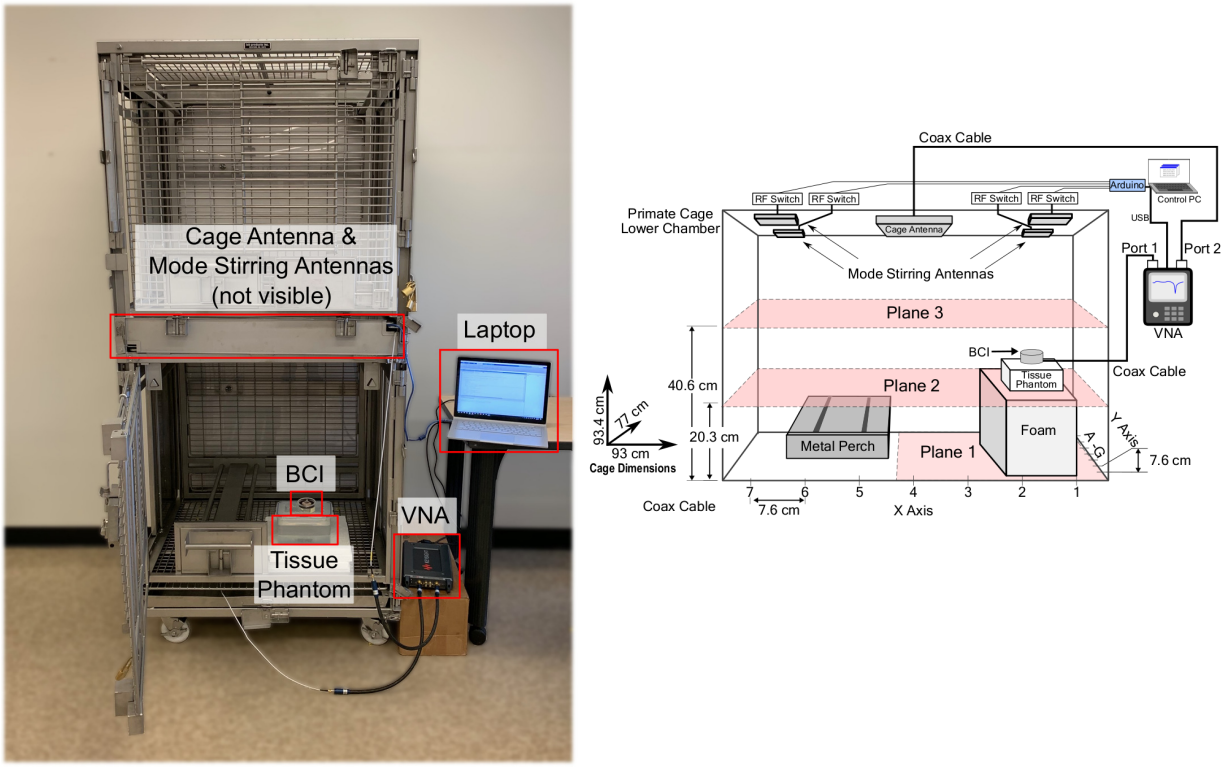

(a) (b)

Figure 6.2: (a) Photo and (b) Block diagram of the measurement setup for characterizing the the 915 MHz and 2.4 GHz ISM-band wireless channel inside the NHP cage with electronic mode stirring.

field (Fig. 6.1(b)). Similar approaches have seen success using switched parasitic antennas (SPAs) for beamforming to improve the received signal strength of sensor nodes using backscatter communication [91–94], though to the best of our knowledge, this work is the first to propose using low-profile SPAs to implement electronic mode stirring inside the reverberant cavity of an animal cage.

Our experimental results demonstrate that electronic mode stirring using SPAs can significantly reduce the worst-case insertion loss within a cage. We present comparisons of the CTF within a NHP cage taken with and without mode stirring in the 915 MHz and 2.4 GHz ISM bands. These findings represent a unique contribution to the field of applied electromagnetics:

- **Suitability for biomedical device applications:** The electronic mode stirring approach imparts no additional hardware or software complexity on the size- and energy- constrained biomedical device, and it can be im-

plemented in standard metal animal cages. Unlike MIMO methods requiring multiple antennas with minimal mutual coupling, which is difficult to implement on a size constrained device, the mode stirring approach can leverage a single antenna on the biomedical device. Future iterations could be tractably adapted for more complex applications, including closed-loop CTF control to adapt the mode stirring configuration to the movement of the research animal within the cage.

- **Platform Flexibility:** The benefits of the electronic mode stirring architecture could enable higher data rates and lower power consumption for both backscatter and conventional radios. The results from this chapter can be generalized to other arenas of varying size and geometry.

- **Dynamic Control:** The electronic mode stirring configurations can be controlled quickly (nanoseconds) without obtrusive mechanical assemblies, enabling the mode stirring configuration to be changed as the NHP moves inside the cage. Dynamic control opens the door for future interdisciplinary work integrating communication theory, control theory, and experimental neuroscience.

In this chapter, Section 6.2 presents a description of the experimental setup, the NeuroDisc BCI and the mode stirring architecture. Section 6.3 presents the experimental methods, results, and a discussion of the findings. Lastly, Section 6.4 provides conclusions and ideas for future research.

6.2 Channel Transfer Function Measurements

6.2.1 Experimental Environment

Metal Non-Human Primate (NHP) Cage

Measurements were conducted in the lower chamber of a standard double-height NHP cage provided by the Washington National Primate Research Center (Fig. 6.2). This work was conducted with tissue phantoms instead of live animals, so no animal use authorization was required. The lower chamber has external dimensions of 93.4 cm $\times$ 93 cm $\times$ 77 cm (height $\times$ width $\times$ length). All six cage sides are made of a metal mesh with a mean grid spacing of 2.5 cm. The ceiling of the lower chamber is additionally under the solid metal bed pan of the upper chamber. A 60.7 cm $\times$ 23.4 cm polycarbonate window is inset into one cage wall, and inside the cage there is an 18 cm $\times$ 15 cm metal seat for the NHP. The mean grid spacing of the mesh is more than 10$\times$ smaller than the shortest wavelength of the 915 MHz ISM band ($\lambda \approx 32.3$ cm) and 6$\times$ smaller than the shortest wavelength of the 2.4 GHz ISM band ($\lambda \approx 12$ cm).

A total of 126 measurements were made at locations across three measurement planes: 28 locations on Plane 1, 49 locations on Plane 2, and 49 locations on Plane 3. The vertical spacing between measurement planes was 20.3 cm. Each measurement plane was subdivided into a grid with 7.6 cm spacing, with the X axis labelled *A* through *G* and the Y axis labelled *1* through *7*. Measurements were conducted in the center of the grid squares, as shown in in Fig. 6.2(b).

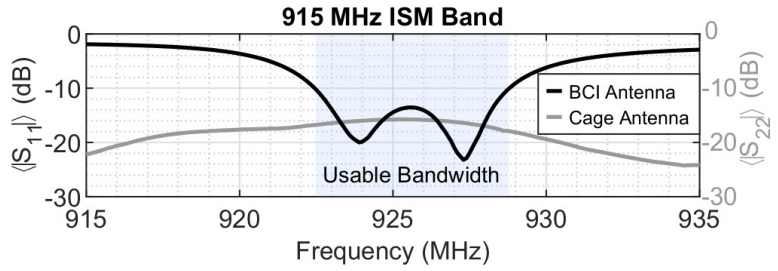

(a)

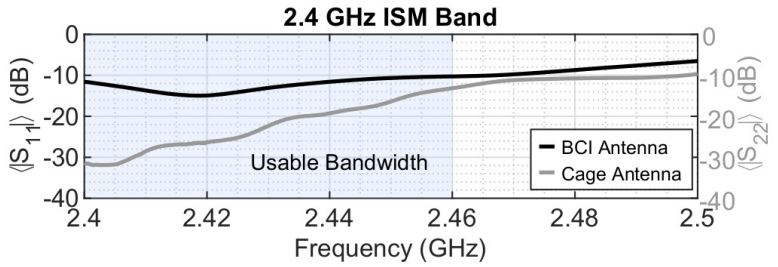

(b)

Figure 6.3: Return loss ensemble average for the BCI antenna, $\langle S_{11} \rangle$, and the cage antenna, $\langle S_{22} \rangle$ without mode stirring antennas for the (top) 915 MHz ISM band and (bottom) 2.4 GHz ISM band. The usable bandwidth (shaded region) was determined by the BCI antenna's performance.

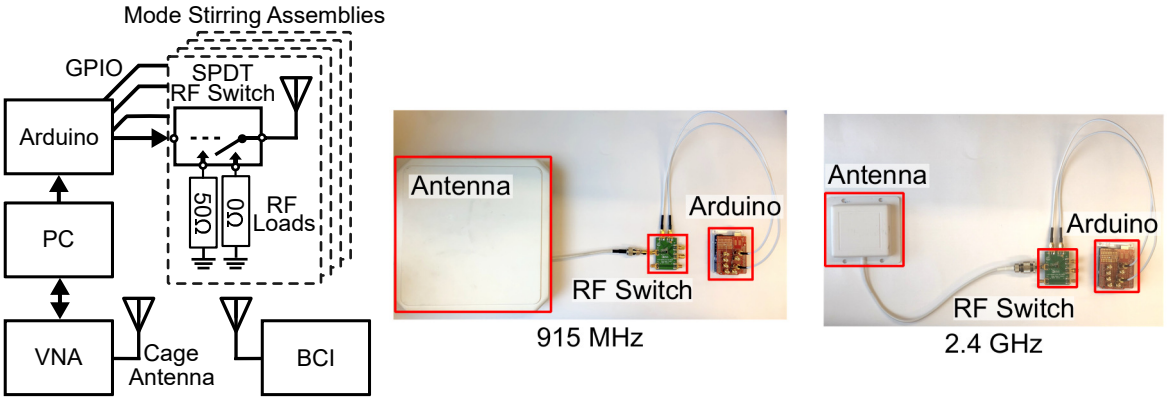

(a) (b) (c)

Figure 6.4: Block diagram (a) and photos of a single mode stirring assembly used for 915 MHz (b) and 2.4 GHz (c).

Columns 5-7 on the bottom measurement plane (Plane 1) were inaccessible due to the height of the metal NHP perch. In this index scheme, position D4 corresponds to the center of the cage.

6.2.2 Experimental Equipment

Vector Network Analyzer

S-parameter measurements were made using a two-port Keysight P9375A Vector Network Analyzer (VNA) controlled by a laptop (Fig. 6.2). Prior to the measurements, a two-port VNA calibration was performed to set the measurement reference plane at the BCI and external antenna ports. At each measurement point, the cables were dressed to the cage walls to minimize their influence on the measurements.

Tissue Phantom

A tissue phantom that approximates the dielectric effects of a typical juvenile male rhesus macaque was used for all measurements. The tissue phantom consists of a 19.5 cm $\times$ 12.0 cm $\times$ 11.0 cm plastic container filled with 2.5 liters of tissue-equivalent saline solution (0.91 g NaCl per liter of distilled water).

NeuroDisc Brain-Computer Interface (BCI)

The NeuroDisc was configured for each frequency band by connecting the appropriate BCI antenna. A semi-custom antenna was used, made from an off-the-shelf ceramic antenna element and a custom PCB. The same PCB was used for both frequency bands, and it consisted of a circular, 5.5 cm diameter, two-layer FR-4 PCB with 1.6 mm dielectric thickness and 30μ copper trace thickness. The top side of the BCI antenna PCB contained a centered, circularly shaped ground plane and a ceramic patch antenna. For the 915 MHz band, an Abracon APAE915R2540ABDB1-T antenna with dimensions 2.5 cm $\times$ 2.5 cm $\times$ 0.4 cm is used; for the 2.4 GHz band, a Tagolas Inc. WLP.2450 antenna with dimensions 2.5 cm $\times$ 2.5 cm $\times$ 0.4 cm is used. The bottom of the PCB had a UMCC coaxial connector, allowing the antenna to connect to the Comms FPGA board via a 5 cm UMCC-to-UMCC coaxial cable.

The average measured reflection coefficients of the BCI antennas and the cage antenna are plotted in Fig. 6.3 for the 915 MHz (top) and 2.4 GHz (bottom) bands. The BCI antenna was connected to port 1 of the VNA with a coaxial cable and placed on top of a tissue phantom inside the cage; the cage antenna was connected to port 2 of the VNA. The measurements in Fig. 6.3 show the average S_{11} (for the BCI antenna) and S_{22} (for the cage antenna) across all positions in the cage. To determine the usable bandwidth of each BCI antenna on each frequency band, the ensemble average of S_i was taken across all positions,

$$\langle |S_i(f)| \rangle = \frac{1}{N} \sum_{k=1}^{N} |S_i^{(k)}(f)| \tag{6.1}$$

where N is the total number of measurement positions in the cage and $|S_i^{(k)}(f)|$ is the magnitude of the measured reflection coefficient at position k across the entire frequency band for port i of the VNA. For $N = 126$ and measuring at 1000 frequency points from 850-950 MHz and 2.400-2.500 GHz, the usable 10 dB impedance bandwidth was found to be 922.5-928.8 MHz (6.3 MHz) for the 915 MHz ISM band and 2.4000-2.4648 GHz (64.8 MHz) for the 2.4 GHz

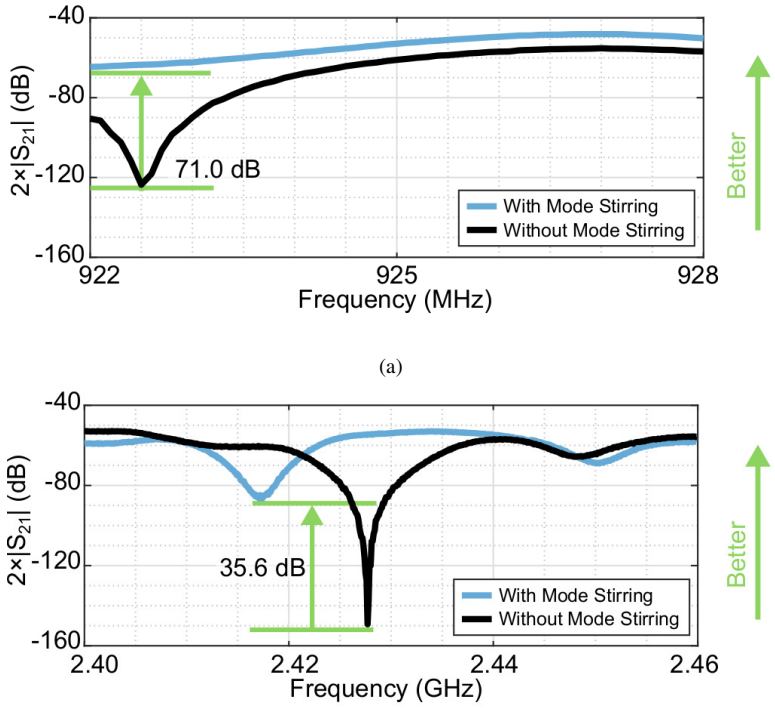

Figure 6.5: Plots comparing the worst-case insertion loss $|S_{21}|$ across all positions with and without electronic mode stirring for (a) the 915 MHz ISM band at plane 1, row 2, column G (best mode stirring configuration: 16); and (b) 2.4 GHz ISM band at plane 1, row 3, column C (best mode stirring configuration: 16).

ISM band (Fig. 6.3).

Cage Antenna

A cage antenna representing a monostatic backscatter communication antenna [44] was affixed on the inside of the mesh wall separating the upper and lower chambers of the NHP cage, as shown in Fig. 6.2(b). For measurements in the 915 MHz band, a Laird Technologies S9028PCR right-hand circularly polarized, air dielectric patch antenna was used; for the 2.4 GHz band, an L-Com Inc. 2.4 GHz 8 dBi RHCP antenna was used. The average measured reflection coefficient of the antenna for each frequency band is plotted in Fig. 6.3.

Mode Stirring Assemblies

For the mode stirring measurements in each frequency band, we installed a band-specific mode stirring assembly into the NHP cage. The assembly was comprised of several components (Fig. 6.4): four mode stirring antennas

selected for the particular frequency band; four Analog Devices ADG918 single-pole dual throw (SPDT) RF switch evaluation boards (one for each mode stirring antenna) with 50Ω and short circuit terminations; and one Arduino UNO with a daughter board for routing 3.3V power and digital control signals to the RF switches. A PC controlled the Arduino UNO using MATLAB (MathWorks) to digitally actuate the four RF switches. With four mode-stirring antennas each having two possible impedance states, 16 total mode stirring configurations were possible (e.g. all four shorted, three shorted and one with a 50Ω load, etc). For the 915 MHz band measurements, L-Com HG8909P linearly polarized antennas with 9 dBi of gain were used; for the 2.4 GHz band measurements, L-Com HG2408P linearly polarized antennas with 8 dBi of gain were used. Note that the mode stirring assemblies were entirely removed from the cage for the measurements designated as *without mode stirring*.

6.3 Experimental Methods & Results

6.3.1 Measuring the Channel Transfer Function

For each ISM frequency band, two sets of measurements were taken: one set *without* mode stirring (baseline) and one set *with* mode stirring (experimental). The mode stirring assemblies were not installed in the cage during the baseline measurements. After completing the baseline measurements, the cage antenna was left in the same position, and the mode stirring assemblies were installed. Each mode stirring antenna was mounted in a corner of the steel mesh ceiling with the same orientation with respect to the antennas' polarization. The mode stirring antennas were connected to the RF switches and Arduino, which all sat outside of the testing volume to minimize interference. A graphical depiction of the test setup is shown in Fig. 6.2.

The measurements were conducted by first positioning the BCI and tissue phantom at the center of the desired position in the cage. For the baseline measurements, the two-port S-parameters were measured using the VNA. At each measurement position, a MATLAB script was used to sequentially change the mode stirring configuration and measure the two-port S-parameters until all 16 mode stirring configurations had been measured. The BCI and tissue phantom were then moved to the next position, and the process was repeated until baseline and experimental measurements were made at all 126 positions in the cage. The BCI antenna orientation was maintained constant at each measurement points, and the cables were dressed to the cage walls at each position to minimize their influence on the measurements. Measurements for both frequency bands were taken using 100 kHz steps in the frequency domain.

6.3.2 Characterizing the Channel Transfer Function

Knowledge of the insertion loss throughout the cage provides insight into the link margin and reliability of communication systems. For a backscatter communication system, the link margin can be calculated as

$$P_R = P_{\text{CW}} - IL_{\text{two-way}} + M - L_{\text{sys}} \tag{6.2}$$

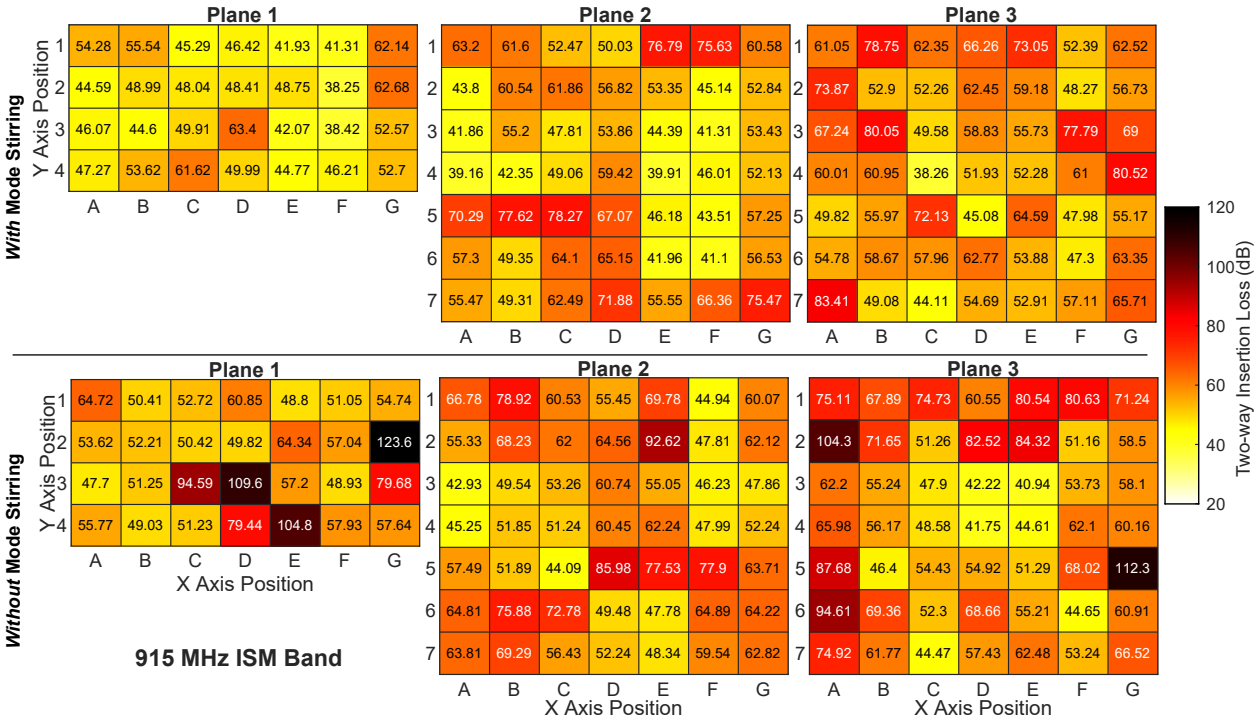

Figure 6.6: Experimental results for the 915 MHz ISM band comparing the highest two-way insertion loss at each measurement point. In all heatmaps, lighter colors indicate lower insertion loss and thus better performance.

where P_R is the received power at the cage antenna in dBm, P_{CW} is the power of the RF carrier wave presented to the cage antenna in dBm, IL is the insertion loss in dB, M is the modulation factor that arises from the symbol-dependent change in impedance at a backscatter modulator (due to its differential radar cross-section), and L_{sys} represents additional system losses in the full-duplex monostatic backscatter receiver [19, 44]. The worst-case insertion loss at a position in the cage will determine the backscatter link margin and the uplink reliability for a given receiver sensitivity and system parameters in Eq. 6.2.

The CTF of the cage was thus characterized using frequency domain power ratio measurements to determine the insertion loss at each position. With the VNA, the transmission coefficient S_{21} was measured at each position in 100 kHz steps over the BCI antenna's average -10 dB bandwidth (Sec. 6.2.2), then converted to two-way insertion loss in decibels

$$IL_{\text{two-way}}(f,k) = 2 \times \big(-20 \times \log_{10}(|S_{21}(f,k)|) \big) \tag{6.3}$$

where f is frequency and k is the measurement position. For brevity, we refer to $IL_{\text{two-way}}$ as IL for the remaining equations.

To determine how electronic mode stirring affected the cage CTF, we compared the worst-case insertion loss at

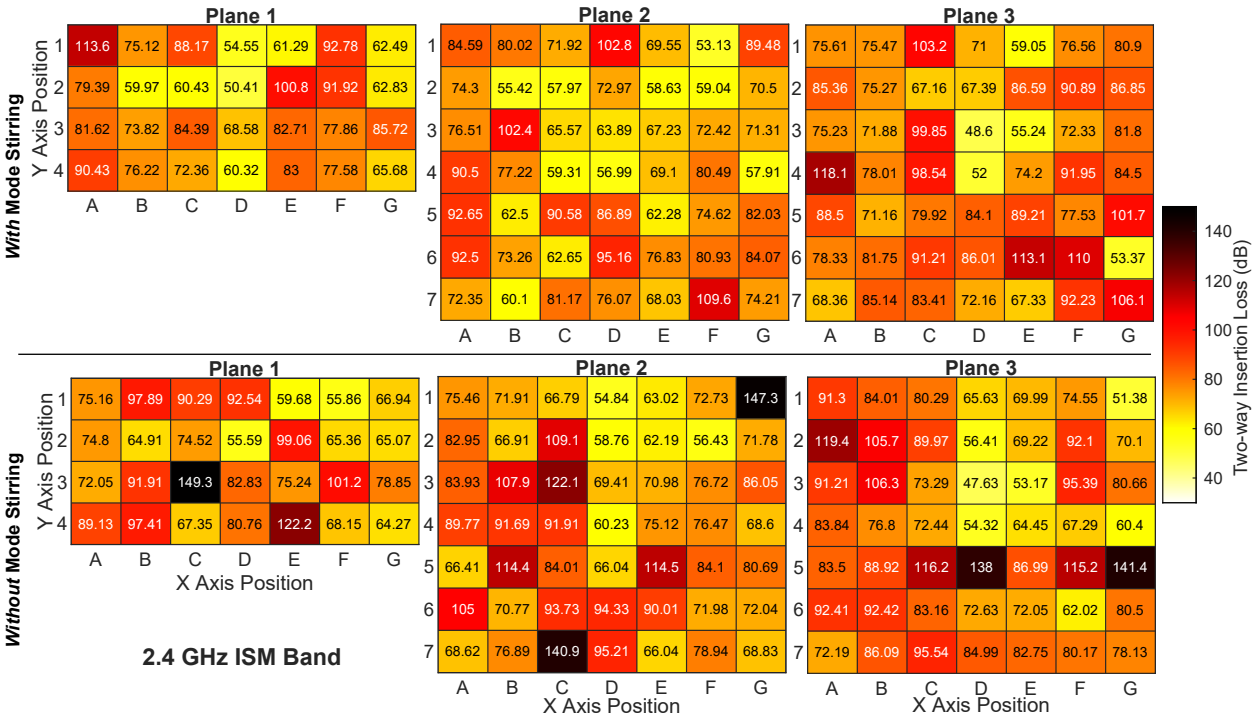

Figure 6.7: Experimental results for the 2.4 GHz ISM band comparing the highest two-way insertion loss at each measurement point. In all heatmaps, lighter colors indicate lower insertion loss and thus better performance.

each position without mode stirring, to the worst-case insertion loss from the mode stirring configuration having the lowest insertion loss. In the baseline case without mode stirring, the worst-case insertion loss corresponded to the maximum insertion loss value across all frequency points:

$$IL_{\text{worst-case}} = \max(IL). \tag{6.4}$$

In the experimental case using mode stirring, the worst-case insertion loss was a function of the mode stirring configuration, indexed by i. We first calculated the worst-case insertion loss for each mode stirring configuration at a specific point, resulting in a 16 element vector, $IL_{\text{worst-case}}(i)$. The argument that minimized the vector corresponded to the best mode stirring configuration for that position:

$$\text{Best Config.} = \arg\min(IL_{\text{worst-case}}(i)). \tag{6.5}$$

Plots of the worst-case measured insertion loss $|S_{21}|$ for the 915 MHz and 2.4 GHz bands are shown in Fig. 6.5(a) and (b), respectively. These plots show how mode stirring improves the worst-case insertion loss for a single point in each frequency band.

To compare how the worst-case insertion loss compared across all BCI positions for the baseline and experimental measurements, heatmaps of the measurements were compiled showing the results for the 915 MHz band in Fig. 6.6 and for the 2.4 GHz band in Fig. 6.7. In these figures, lighter colors represent a lower insertion loss, and thus more favorable channel loss characteristics. Histograms of the worst-case insertion loss for both frequency bands are shown in Fig. 6.8.

Additional statistics were calculated and compiled in Table 6.1 for the 915 MHz band and in Table 6.2 for the 2.4 GHz band. The mean two-way IL (dB) across a plane, $\overline{IL}(p)$, was calculated as

$$\overline{IL}(p) = \sum_{x,y} \frac{\overline{IL}(p,x,y)}{n(x)n(y)} \tag{6.6}$$

where $n(\cdot)$ represents the number of elements in the set, p represents the measurement plane, x represents the column, y represents the row, and $\overline{IL}(p,x,y)$ is the mean two-way IL at a specific position

$$\overline{IL}(p,x,y) = \sum_{f} \frac{IL(f,p,x,y)}{n(f)}. \tag{6.7}$$

The average standard deviation of the insertion loss, $\bar{\sigma}(p)$, for each plane was calculated as

$$\bar{\sigma}(p) = \sum_{x,y} \frac{\sigma(p,x,y)}{n(x)n(y)} \tag{6.8}$$

where

$$\sigma(p,x,y) = \sqrt{\frac{\sum_f \left| IL(f,p,x,y) - \overline{IL}(p,x,y) \right|}{n(f)-1}}. \tag{6.9}$$

6.3.3 Results & Discussion

From the heatmaps of Fig 6.6 and Fig. 6.7 and the statistics in Table 6.1 and Table 6.2, mode stirring is seen to reduce the overall severity and prevalence of deep nulls in the cage CTF.

915 MHz ISM Band

Across all 126 measurement positions, 86 (68.25%) exhibited a reduction of the worst-case insertion loss when mode stirring was used. The worst-case insertion loss across the entire cage improved by 30.10 dB, while the mean insertion loss improved by 3.68 dB across Plane 1, improved by 0.87 dB across Plane 2, and worsened by 1.37 dB across Plane 3. Of the 86 positions that showed an improvement in worst-case insertion loss, 60 positions (47.62% of all positions) had a reduction >6 dB. The average standard deviation of the insertion loss between measurement locations was reduced between 0.29-1.23 dB across all planes, indicating increased uniformity in the insertion loss. The insertion loss at 40 measurement positions (31.75%) worsened with mode stirring enabled, with 26 positions (20.63% of all positions) increasing by more than 6 dB, and the worst-case increase being 34.2 dB.

Table 6.1: 915 MHz two-way channel transfer function measurement summary

	Plane 1			Plane 2			Plane 3		
	Without MS	**With MS**	**Change**	**Without MS**	**With MS**	**Change**	**Without MS**	**With MS**	**Change**
Mean IL (dB)	50.74	43.38	-7.36	50.26	48.52	-1.74	50.54	53.28	+2.74
Worst-Case IL (dB)	123.6	63.4	-60.20	92.62	78.28	-14.34	112.28	83.42	-28.86
IL Std. Dev. (dB)	5.18	2.72	-2.46	4.34	3.76	-0.58	5.18	4.42	-0.76

2.4 GHz ISM Band

Across all 126 measurement positions, 67 (53.17%) exhibited a reduction of the worst-case insertion loss when mode stirring was used. The worst-case insertion loss across the entire cage decreased by 17.81 dB. The mean insertion loss increased by 0.41 dB across Plane 1 and by 0.58 dB across Plane 2; across Plane 3 it decreased by 0.35 dB. Of the 67 positions that showed a reduction in worst-case insertion loss, 51 positions (40.48% of all positions) had a reduction $>$6 dB. The average standard deviation of the insertion loss between measurement locations showed minor changes, reducing between 0.14-0.26 dB across Planes 1 and 2, and increasing by 0.07 dB across Plane 3. The insertion loss at 59 of the positions (46.83%) exhibited increased worst-case insertion losses, with 35 positions (27.78% of all positions) increasing by more than 6 dB and the maximum increase being 48.02 dB.

Overall Results and Implications

The measurements in Fig. 6.6 and Fig. 6.7 revealed the dense multipath interference present inside the NHP cage. Despite an open air space inside the cage, with 1 meter or less distance between the cage antenna and the BCI, very deep nulls appeared due to reverberation within the cage.

The measurements using mode stirring demonstrated an observable reduction of the worst-case insertion loss within the cage. The heatmaps in Fig. 6.6 and Fig. 6.7 show that, generally, the magnitude of deep nulls in the CTF decrease when electronic mode stirring is used. These observations are supported by the statistics in Table 6.1 and Table 6.2, where we observe that the worst-case mean two-way insertion loss was reduced by more than 7 dB in the 915 MHz ISM band and by more than 11.63 dB in the 2.4 GHz band. These changes to the CTF in both frequency bands can be seen by the histograms of Fig. 6.8. We observe that the grouping of worst-case two-way insertion loss counts is shifted to lower values when mode stirring is introduced. Further, the high insertion loss values from measurements without mode stirring disappear as well. The improved insertion loss statistics throughout the cage suggests that electronic mode stirring can be used to increase the channel capacity of the NHP cage and bolster the reliability and/or data rates of wireless communication systems in the cage.

Table 6.2: 2.4 GHz two-way channel transfer function measurement summary

	Plane 1			Plane 2			Plane 3		
	Without MS	**With MS**	**Change**	**Without MS**	**With MS**	**Change**	**Without MS**	**With MS**	**Change**
Mean IL (dB)	56.88	57.70	+0.82	58.30	59.46	+1.16	59.82	59.12	-0.70
Worst-Case IL (dB)	149.26	113.64	-35.62	147.30	109.58	-37.72	141.38	118.12	-23.26
IL Std. Dev. (dB)	7.78	7.50	-0.28	7.84	7.32	-0.52	8.22	8.36	+0.14

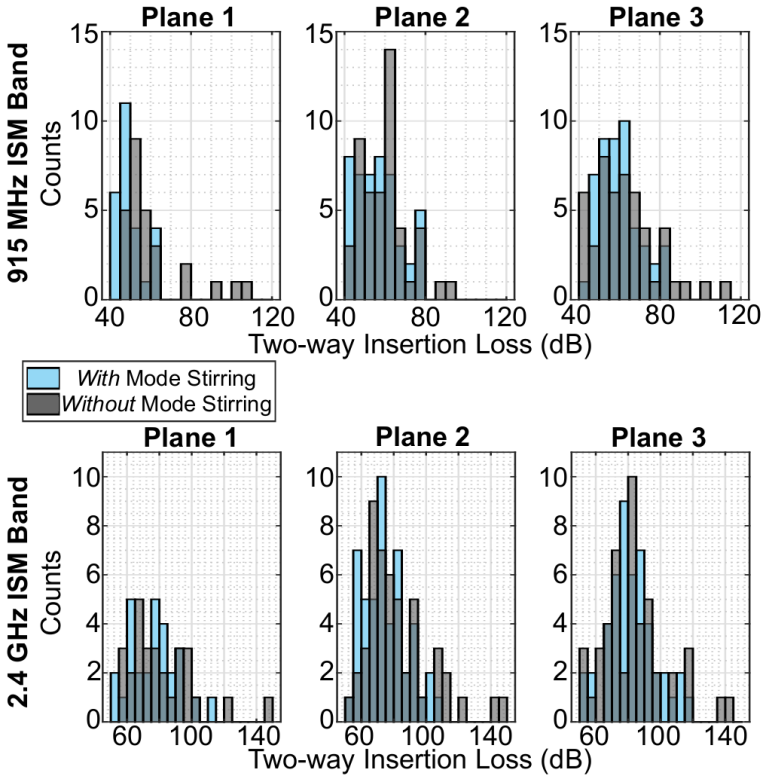

Figure 6.8: Histogram of highest insertion loss for each measurement point in the 915 MHz ISM band (top) and 2.4 GHz ISM band (bottom), comparing results with and without electronic mode stirring.

6.4 Chapter Conclusions

In this chapter, we presented a novel implementation of electronic mode stirring in a non-human primate (NHP) cage. Using switched parasitic antennas (SPAs) mounted to the ceiling of the cage and measuring the power ratio between a BCI antenna and a ceiling-mounted cage antenna, we found that electronic mode stirring can create a more favorable communication channel in both the 915 MHz and 2.4 GHz ISM bands. We specifically observed that the use of SPAs

improved the worst-case insertion loss by up to 60.20 dB in the 915 MHz band and by up to 35.62 dB in the 2.4 GHz band. These reductions in insertion loss increase the channel link margin and thus the overall channel capacity for wireless uplinks.

The results suggest that electronic mode stirring is a promising technique to improve the performance of ultra-low power backscatter wireless uplinks for BCIs. Further work is required to continuously optimize the mode stirring configuration given changes in the cage environment as the NHP moves throughout the cage. To implement real-time mode stirring optimization, a closed-loop optimization approach could be implemented where the mode stirring configuration is selectively changed to maximize the received backscatter signal power as the NHP moves around the cage.

Chapter 7

ORTHOGONAL FREQUENCY DIVISION MULTIPLEXING (OFDM) BACKSCATTER COMMUNICATION

Key point: OFDM modulation achieves reliable communication in dense multipath environments by spreading a signal's energy across orthogonal subcarrier frequencies. In this chapter, we present three all-digital architectures for OFDM backscatter communication that use RF switches and discrete loads to implement digitally controlled single-sideband OFDM backscatter modulators. We provide design, analysis, and measurements of a selected architecture using five subcarriers with binary phase shift keying (BPSK) modulation for a throughput of 1.25 Mbit/s and an RF modulator energy efficiency of 160 pJ/bit. We additionally present over-the-air validation of an implementation with 195 kbps throughput.

This chapter is based on work in [47].

7.1 Introduction

The potential for energy efficiency offered by backscatter communication has resulted in numerous practical applications, primarily with different single-carrier modulation schemes. Researchers have demonstrated analog modulation [95] and digital modulation schemes such as amplitude-shift keying [96, 97], phase-shift keying [17, 64, 98], frequency shift keying [41, 46, 78], quadrature phase-shift keying [16], and 16-quadrature-amplitude modulation modulation [40] with data rates as high as 96 Mbits/s and up.

A drawback of single-carrier modulation is decreased reliability in channels with time varying multipath. Conventional active radio standards, such as IEEE 802.11 WLAN, have used multi-carrier orthogonal frequency division multiplexing (OFDM) to overcome narrowband interference. Traditionally, OFDM is implemented using the real and imaginary outputs of an inverse Fast Fourier Transform (IFFT) to control two voltage digital-to-analog converters (DACs) which in turn drive a vector modulator, as shown in Fig. 7.1(top). This implementation is relatively power hungry due to the need to run the DACs at a sampling rate sufficient to Nyquist sample the entire OFDM signal bandwidth.

Several recent works have developed building blocks for OFDM backscatter communication, but each still requires the use of digital-to-analog converters (DACs) and high speed lookup tables to compensate for the non-linear impedance-vs.-voltage curves of typical modulators. For example, in [63] pulse-shaping for backscatter communication was explored by using a DAC to control a voltage-variable impedance, such as a field-effect transistor (FET), connected to the backscatter device's antenna. The impedance of such a single-FET modulator is a non-linear func-

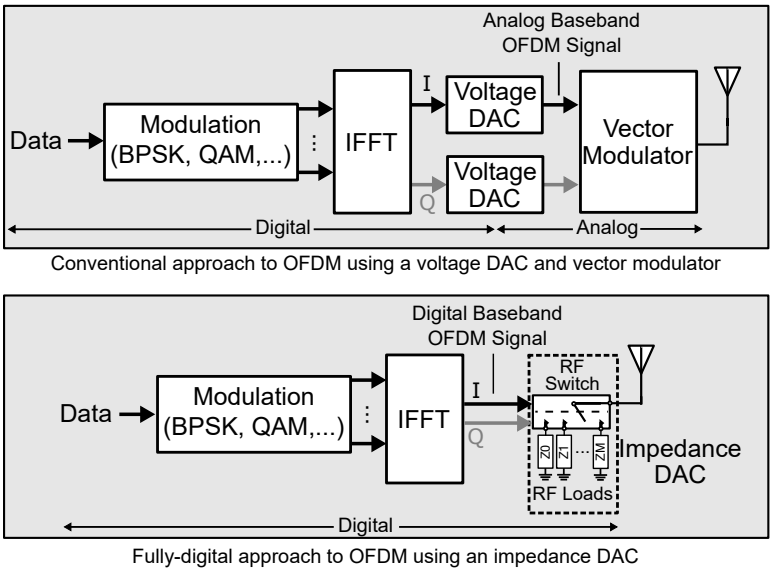

Figure 7.1: Comparison of (top) a traditional OFDM architecture using I/Q voltage DACs and a vector modulator and (bottom) the proposed all-digital backscatter OFDM architecture using an RF switch and discrete loads to form a discrete-valued impedance DAC.

tion of the applied control voltage and is also strongly influenced by the incident carrier wave (CW) power. In [99], an amplitude-frequency-shift keying (AFSK) OFDM backscatter integrated circuit (IC) was developed. The IC uses direct digital frequency synthesizers to generate distinct subcarrier signals driving R2R DACs that in turn provide gate bias for an array of modulating FETs. OFDM-like backscatter signals were demonstrated in [100], but this work also relied on DACs, FET-based modulators, and tuned RF structures. In these prior works, achieving incident-power-independent impedance states is challenging due to the modulator FET's non-linear dependence on incident power and gate bias voltage. Further, high speed DACs generally have high power consumption, on the order of tens of milliwatts or greater, making them an unfavorable choice for highly energy-constrained wireless devices.

In this chapter, we present three all-digital architectures for OFDM backscatter communication that can be realized using digital CMOS RF switches as the backscatter modulator elements (Fig. 7.1 (bottom)). We provide design analysis on a selected architecture, with FPGA-based digital logic driving a custom backscatter modulator printed circuit board (PCB) (Fig. 7.2) described in [101]. The modulator leverages digitally tuned capacitors (DTCs) to achieve a reconfigurable inductor-free modulator that facilitates prototyping for future application specific integrated circuits (ASICs). This chapter provides a significant contribution to the field of low power wireless sensing and backscatter communication in the following ways:

- Design and Performance Repeatability: The all-digital architecture produces repeatable impedances across a far broader range of incident carrier wave power than DAC-driven FET modulator architectures.

- Platform Flexibility: The three proposed OFDM backscatter architectures can be implemented in any conventional digital logic device, including field-programmable gate arrays (FPGAs), complex programmable logic devices (CPLDs), microcontroller units (MCUs), and CMOS ASICs. The design analysis of this chapter provides an understanding of how the design architecture affects digital resource utilization and wireless link performance.

- Protocol Configurability: The proposed OFDM backscatter architectures allow for easy configurability of the physical and link layer communication parameters, such as the number, frequency, and modulation of the subcarriers as well as the desired sideband relative to the incident carrier wave. Well-known OFDM packet structures to mitigate inter-symbol and inter-carrier interference can be easily added.

The outline of this chapter is as follows: Section 7.2 presents an overview of the proposed OFDM backscatter architectures. Section 7.3 presents simulation results for a selected architecture based on an IFFT lookup table (LUT). Section 7.4 presents a comparison between simulated and measured results and an over-the-air validation of this architecture. Finally, Section 7.5 presents conclusions and ideas for future work.

7.2 Architectures for OFDM Backscatter Communication

7.2.1 Impedance DAC

In this work, we chose to use a digitally-controlled CMOS RF switch to control the impedance presented to the antenna. Using a switched modulator has several benefits over voltage-controlled variable impedances. The first is that the switch FETs are biased as digitally controlled RF switches that connect externally provided impedances to the antenna, so fluctuations in the incident RF carrier power do not disrupt the modulator impedance. This is a key limitation of previously-described modulators using the FET itself as a variable impedance. Switch based implementations provide backscatter modulators that can achieve consistent, reliable operation over a wider range of incident carrier wave power. Secondly, the switch is controlled using all-digital logic that is widely available across low-cost MCUs, CPLDs, FPGAs, and ASICs. Once the impedances connected to the switch are determined, there is no need for calibration to achieve repeatable operation. Lastly, CMOS RF switches can achieve data rates of on the order of tens of megabits per second due to their fast switching times [40, 102]. A disadvantage to using CMOS RF switches is that the two-way insertion loss can often be $>$3 dB, however this can often be improved given careful attention to the switching FET device and process.

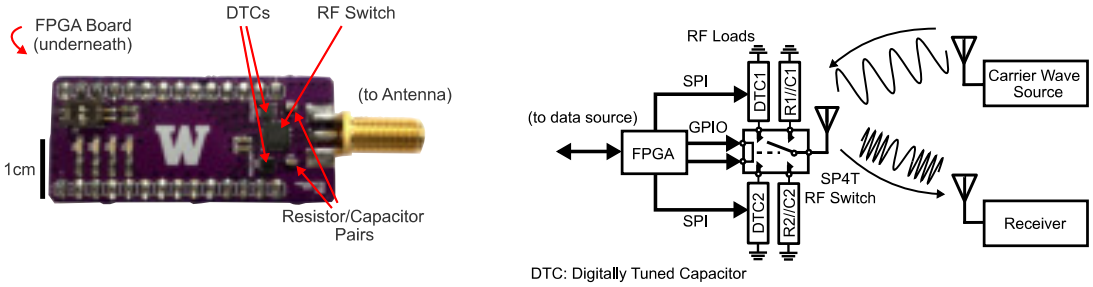

(a) (b)

Figure 7.2: OFDM backscatter was implemented on an off-the-shelf FPGA and a custom switched-impedance backscatter modulator using digitally-tuned capacitors (DTC) described in [101]. (a) Photo of the backscatter modulator, (b) Block diagram of the backscatter modulator.

An RF switch used to switch between different discrete impedance states can be viewed as an impedance DAC. For example, a single pole-single throw (SPST) switch can be seen as providing 1-bit of impedance resolution. At a constant switching rate, a SPST switch can achieve ON-OFF keying (OOK) or binary phase-shift keying (BPSK) modulations. However, if the switching rate of the SPST is modulated such that one of M different switching rates is selected for each symbol period, then M-ary frequency shift keying (FSK) modulation can be implemented, such as in [46].

A key insight in this work is that multiple simultaneous carrier frequencies can be generated by using multi-tone symbol sequences to actuate the RF switch. These symbol sequences correspond to the digital baseband OFDM signal of Fig. 7.1(bottom). Using such symbol sequences can enable even a one-bit impedance DAC, e.g. an SPST switch, to generate orthogonal subcarriers.

7.2.2 OFDM Backscatter Architectures

A challenge when implementing OFDM is balancing the desire for a fast, high-resolution IFFT with the limited hardware resources and power available in embedded systems. An IFFT block has many different design parameters, including the number of bins, the bit width and fractional length for data and twiddle factors, and the radix of the butterfly modules. With each of these parameters comes trade-offs in computational speed and resource utilization. There has been significant research in hardware efficient algorithms designed for use in OFDM [103]. For example, in applications that have unused bins in the IFFT, "pruning" can be used to reduce the complexity of the IFFT block [104]. Additionally, for low resolution applications, smaller bit widths and fractional parameters can be used to reduce the number of logic elements and memory needed for a particular design. To better understand the resources required for implementing OFDM backscatter, we present three architectures for generating the requisite digital baseband OFDM

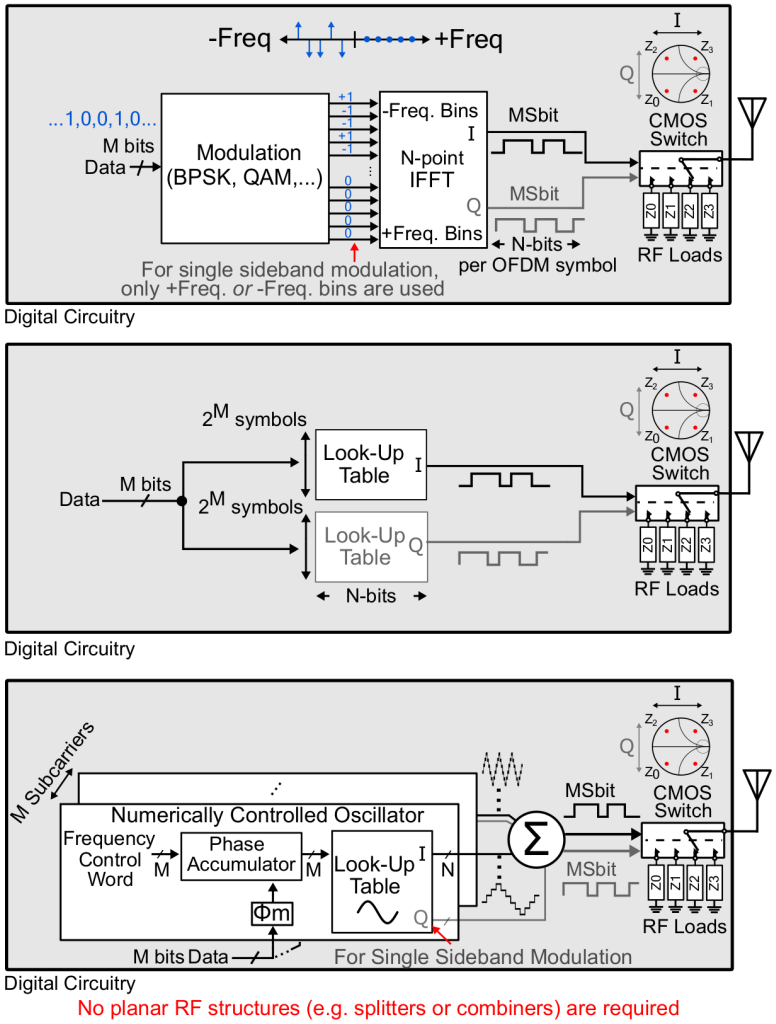

Figure 7.3: Three candidate architectures for implementing OFDM backscatter communication with a switched impedance modulator. OFDM subcarriers can be generated using (top) on-the-fly Inverse Fast Fourier Transform (IFFT), (middle) IFFT lookup tables (LUTs), and (bottom) numerically controlled oscillators based on a sine look-up table (LUT).

signals: an on-the-fly inverse Fast Fourier Transform (IFFT) architecture, a IFFT Look-Up Table (LUT) architecture, and a numerically controlled oscillator (NCO) architecture, as shown in Fig. 7.3.

IFFT-based Architecture

OFDM backscatter communication can be generated using the on-the-fly IFFT-based architecture shown in Fig. 7.3 (top). This architecture closely resembles a traditional OFDM implementation, except it replaces the voltage DACs

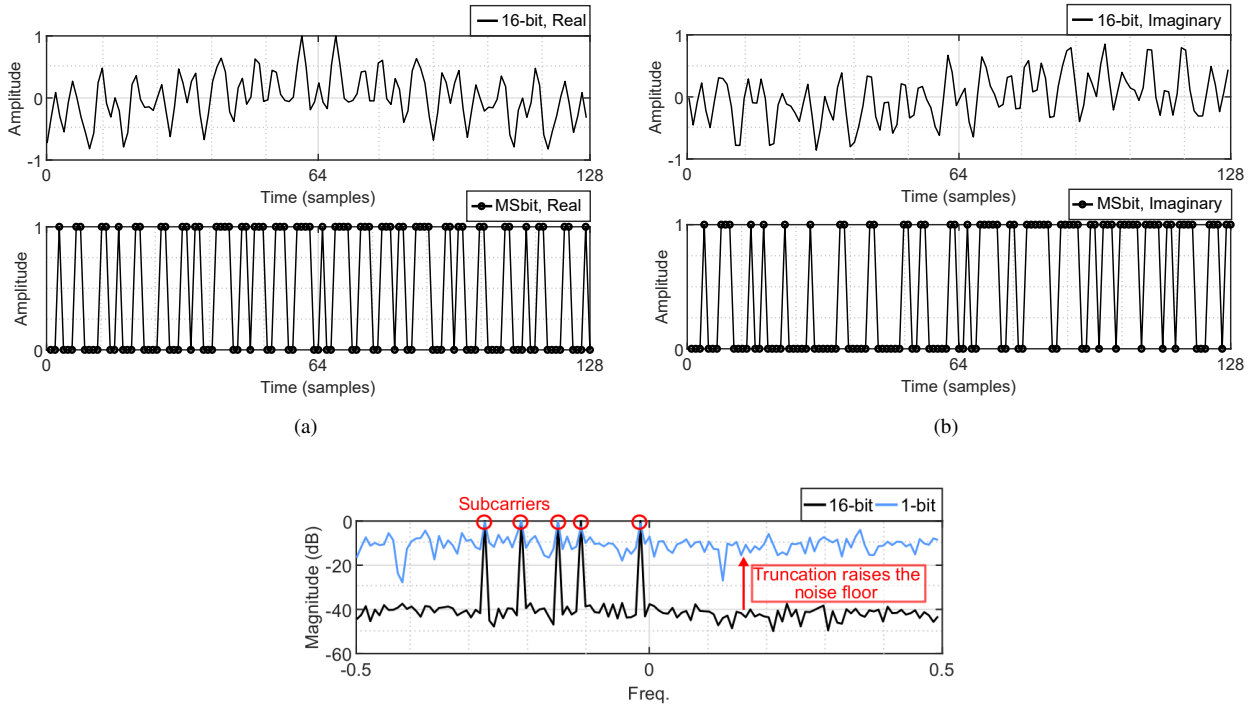

Figure 7.4: Simulation of the baseband signals showing the output of a 128-bit IFFT with 16-bit resolution and the same signal truncated to the most significant bit (MSb): (a) real parts; (b) imaginary parts; (c) Fourier transform of the complex IFFT output comparing a 16-bit resolution signal to the 1-bit truncated signal.

Table 7.1: Resource Allocation for Example OFDM Backscatter Architectures Employing Five Subcarriers

Architecture	**Logic Elements**	**Multipliers**	**Block RAM (Bytes)**
128-Point Buffered Burst IFFT	3,556	24	1,985
128-Point IFFT LUT	505	0	0
NCO (Full Sine LUT, 2048-point)	1600/subc.	0	0
NCO ($\frac{1}{4}$-wave Sine LUTs, 2048-point)	500/subc.	0	0
NCO (Full Sine LUT, 128-point)	120/subc.	0	0
NCO ($\frac{1}{4}$-wave Sine LUTs, 128-point)	50/subc.	0	0
NCO (Small RAM)	81/subc.	0	60

Values are reported from the Intel Quartus Prime *Analysis & Synthesis* report summary.

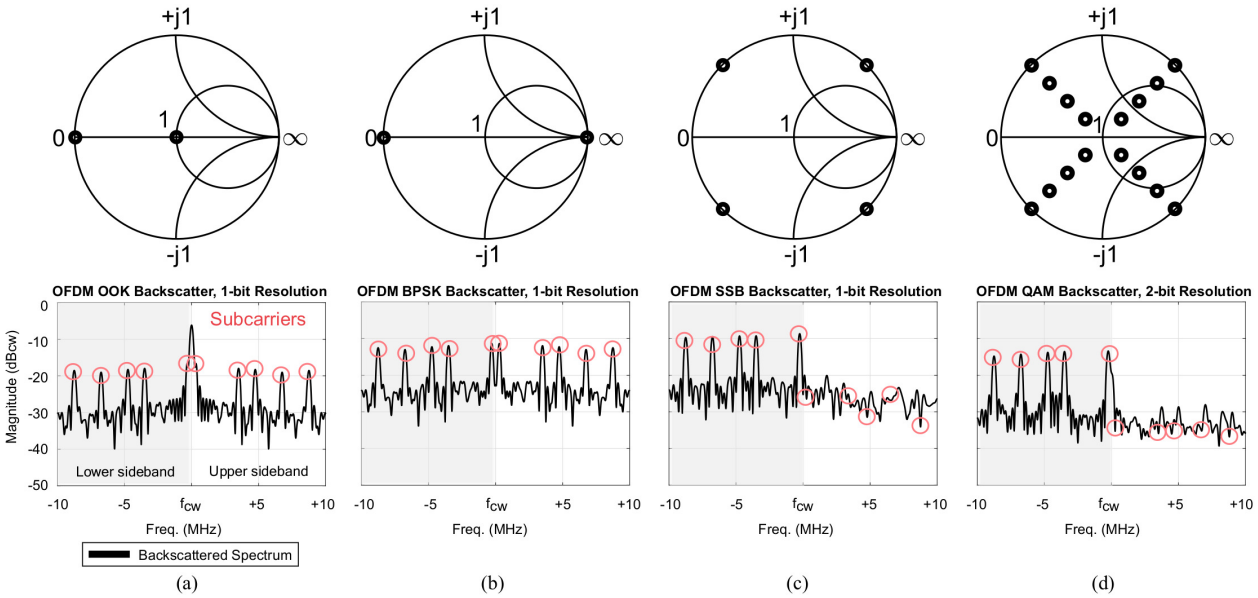

Figure 7.5: Simulation of OFDM backscatter spectral power using five subcarriers and different impedance configurations: (a) two real-valued impedances that are absorptive and reflective, (b) two real-valued reflective impedances that are 180 degrees out of phase, (c) four complex-valued reflective impedances that are 90 degrees out of phase, enabling single sideband modulation, and (d) sixteen complex-valued reflective impedances. (a)-(b) can be implemented with a two-throw switch, (c) with a four-throw switch, and (d) with a sixteen-throw switch. Spectral plots are in units of power relative to the incident carrier wave (abbreviated as dBcw).

and vector modulator by an RF switch and two or more discrete RF loads. In this configuration, data bits are passed through a modulation block that maps bits to M complex-valued symbols. The symbols are then arranged in parallel and input into the desired subcarrier frequency bins of an N-point IFFT, while the undesired subcarrier frequency bins are set to zero. If the input to the IFFT is symmetric, with the same inputs being applied to the corresponding positive and negative frequency bins, then the frequency spectrum will be double sideband (DSB) and the IFFT output will be a real-valued time domain signal that is N samples long. If the input to the IFFT is asymmetric with inputs only applied to the positive or negative frequency bins, then a single sideband (SSB) frequency spectrum will be generated. The IFFT output in this case will be complex, composed of a real (I) and imaginary (Q) component that are each N samples long. Each sample will have its amplitude coded in one or more bits.

For an RF switch with S switch states, $c = \log_2(S)$ control signals are required. The amplitude of the IFFT output can be truncated such that c total bits are obtained. For example, a single pole-four throw (SP4T) switch requires two control bits. In this case, the most-significant bit (MSB) from each of the I and Q signals can be used to actuate the switch among its four possible states. The digital baseband signals for this example are shown in Fig. 7.4. As a result

of the I and Q signals being truncated in resolution, the wideband noise floor is elevated relative to an implementation having more switch states.

Simplified IFFT LUT Architecture

Implementing an on-the-fly IFFT block in a device allows for significant flexibility, but it comes at the cost of hardware complexity and additional power consumption. IFFT implementations in digital logic generally require multipliers and block memory for storing intermediate calculations as well as LUTs for the complex exponential roots of unity, also known as twiddle factors. For example, a 128-point Radix-2 Buffered-Burst IFFT generated using the Intel Quartus Prime FPGA design software uses 24 multipliers, nearly 2,000 Bytes of RAM and over 3,000 logic elements (TABLE 7.1). Certain low cost, low power digital devices like the Lattice Semiconductor iCE40 FPGA [105] and MachXO2 [106] are appealing platforms for backscatter communication due to their low static power consumption, but they lack dedicated multiplier blocks and requisite number of logic elements to compute the IFFT. These hardware constraints can be overcome though by pre-calculating OFDM backscatter symbols and storing them in LUTs, reducing resources at the cost of real-time configurability. A block diagram of this implementation is shown in Fig. 7.3 (middle). In this implementation, the incoming data bits are used to select the corresponding OFDM symbol from the pre-generated LUT. As TABLE 7.1 shows, this implementation requires only 17% of the logic elements of an IFFT and no multiplier or block RAM.

NCO Architecture

An alternative to IFFT-based architectures is to use a dedicated NCO for each subcarrier, as shown in Fig. 7.3 (bottom). In this approach, the outputs of each NCO are added together in a digital adder, after accounting for potential bit growth. The c MSbits are then used to actuate the RF switch. For applications that require real-time configurability for a small number of subcarriers, this is an appealing choice. Each NCO is characterized by its phase resolution, i.e. number of samples per sinusoidal period N_{NCO}, and the amplitude resolution, i.e. number of bits per sample. The output frequency is then controlled by a frequency control word, f_{ctl}, such that the output frequency is $f_{\text{out}} = \frac{f_{\text{ctl}}}{N_{\text{NCO}}} * f_{\text{s}}$, where f_{s} is the sample rate.

In the simplest implementation where an NCO is built using a full sinusoidal LUT with, for example, 11-bit phase resolution and 16-bit amplitude resolution, each subcarrier requires approximately 1600 logic elements. By exploiting the symmetry in a sinusoidal signal, however, it is possible to generate the same signal using a $\frac{1}{4}$-wave LUT with significant complexity savings. Other implementations exist for NCOs that trade off between logic elements, multipliers, and block RAM [107]. TABLE 7.1 outlines the observed resource utilization for three different NCO architectures.

7.3 Simulating OFDM Backscatter Communication

7.3.1 Effects of the Impedance Constellation on OFDM Backscatter Spectrum

In all of the OFDM Backscatter architectures, the choice of the RF switch and the impedances connected to it will impact the backscattered frequency spectrum. Numerical simulations were performed to explore the effects that number of RF switching throws and impedance values would have. Simulations were performed in MATLAB R2018a software (MathWorks, Inc.). In the simulations, the simplified IFFT LUT architecture was used based on a 128-point IFFT. The simulations used a symbol rate of 250 kHz, a sample rate of 32 MHz, and five subcarriers (250 kHz, 3.5 MHz, 4.75 MHz, 6.75 MHz, and 8.75 MHz). Each subcarrier was modulated using BPSK modulation, leading to 32 possible OFDM symbols.

Four different RF switch configurations were simulated, as shown in Fig 7.5. The first two simulation cases used single pole-single throw (SPST) RF switches, with one simulation using absorptive and reflective impedance states and other using two reflective states 180 degrees out of phase. For these two simulations, only the in-phase (I) signal was used to actuate the RF switch, yielding an impedance DAC resolution of one-bit. The third simulation case represented a single pole-four throw (SP4T) RF switch and used four reflective impedance states that were 90 degrees out of phase relative to adjacent states. This situation simulated single sideband backscatter modulation. Both the in-phase (I) and quadrature (Q) control signals were used, each with one-bit resolution, as shown in Fig. 7.4. The fourth simulation case simulated a single pole-sixteen throw (SP16T) RF switch. The impedance values were chosen to implement single sideband modulation using the in-phase (I) and quadrature (Q) control signals with two-bit resolution each.

The backscatter power spectrum was estimated for each simulation case to compare performance of the different switch and impedance configurations. The power spectra were estimated by calculating the power spectral density (PSD), $S(f) = \mathscr{F}[\bar{R}(\tau)]$ and multiplying it by the estimated noise bandwidth of the window, where $\mathscr{F}[]$ denotes the Fourier Transform and $\bar{R}(\tau)$ denotes the average auto-correlation of the OFDM time-series samples.

From the power spectrum plots of Fig. 7.5, we can make a few key observations. Firstly, single sideband (SSB) backscatter modulation in (c) had the strongest subcarrier power levels with a maximum of -14.7 dB relative to the incident carrier wave (abbreviated as dBcw). BPSK backscatter modulation in case (b) had the second highest subcarrier power at -17.3 dBcw, while 16-QAM in case (d) was -18 dBcw and OOK in case (a) was -21 dBcw. Given that the reflected power is a function of the vector distance between impedance states, these results are as expected.

Secondly, we can examine the subcarrier interference ratio (SIR) by comparing the worst-case relative power levels of spurious tones between subcarriers to the power levels of the subcarriers. The SIR is found to be -6.7 dB, -8.4 dB, -10.2 dB, and -11.1 dB for cases (a)-(d), respectively. This result demonstrates that SIR appears to improve based on two factors: (1) as the minimum distance between reflection states, $|\delta\Gamma_{\text{min}}|$, increases, and (2) as the resolution of the impedance DAC increases from one bit in cases (a) and (b) to two bits in case (c) and to four bits in case (d).

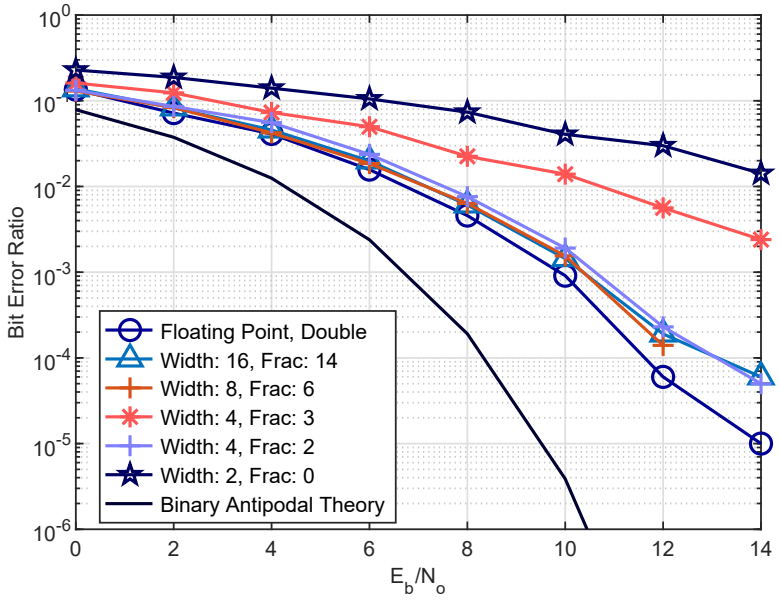

Figure 7.6: Plot of the simulated OFDM backscatter BER versus $\frac{E_b}{N_0}$ for different IFFT fixed-point bit resolutions in terms of width and fractional length.

Thirdly, for cases (c) and (d) we can calculate the sideband rejection ratio (SRR) by comparing to the DSB modulation from case (b). SRR is calculated as the ratio of gain in the desired sideband relative to the attenuation in the undesired sideband at a given subcarrier offset frequency:

$$SRR_{\text{dB}} = \frac{\text{Subcarrier Gain (dB)}}{\text{Subcarrier Attenuation (dB)}} \tag{7.1}$$

We find that SSB backscatter modulation in case (c) achieves an SRR of 17.7 dB while 16-QAM backscatter modulation in case (d) achieves an SRR of 21.5 dB. The SRR does not tell the entire story though. Despite case (d) achieving a higher SRR, the subcarrier gain in the desired sideband is actually negative, decreasing from a maximum of -17.3 dBcw in case (b) to a maximum of -18 dBcw in case (d). This can likely be attributed to the greater $|\delta\Gamma_{\text{min}}|$ in case (b) [44]. Interestingly, the attenuation of the subcarriers in the upper sideband is 30 dB in the worst case for case (d) while it is 25.4 dB in the worst case for (c), yielding a difference of 4.6 dB.

7.3.2 Bit Error Ratio Simulations

Bit error ratio (BER) simulations were performed to investigate how resolution in the IFFT affects data transmission. The simulations used the on-the-fly IFFT architecture of Fig. 7.3 (top). The IFFT was implemented in Matlab as a 128-point Radix-2 IFFT algorithm using fixed-point data. The fixed-point data was defined by the total bit width and the fractional length. These parameters were applied to the data as well as the twiddle factors, which are pre-calculated

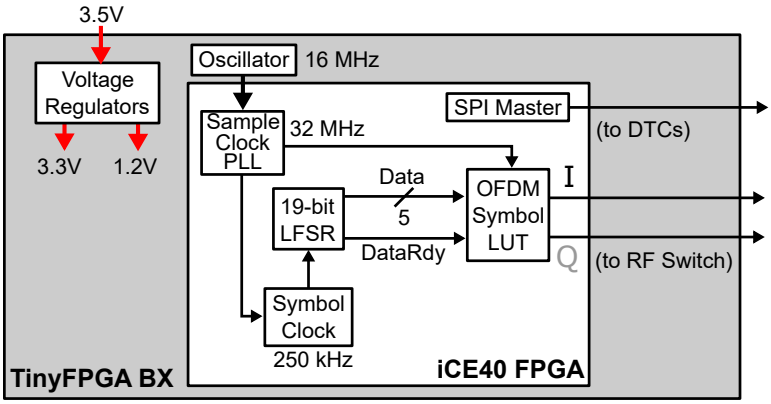

Figure 7.7: Block diagram of the FPGA implementation of the IFFT LUT architecture for OFDM backscatter communication. A 16-bit linear feedback shift register (LFSR) was used to produce pseudo-random data for transmission.

values of a unity magnitude complex exponential at different phase angles that are needed to calculate the IFFT. For transmitting data, five subcarriers with BPSK modulation were used, and four ideal reflective states were assumed for the backscatter modulator, as in the simulation of Fig. 7.5(c). The data was passed through an additive white Gaussian noise channel, and the received symbols were processed using a coherent receiver assuming perfect synchronization. For each value of the energy-per-bit-to-noise-ratio, $\frac{E_b}{N_0}$, either 10^6 bits were transmitted or 200 bit errors accumulated, whichever came first. A plot of simulation results is shown in Fig. 7.6. In this simulation framework, OFDM backscatter in general performs approximately 4.5 dB worse than the theoretical binary antipodal modulation for independent subcarriers in a non-fading channel. This decrease in performance is likely due to the non-linear bit truncation occurring between the IFFT and the backscatter modulation, which generates residual wideband noise, harmonics and inter-modulation distortion. Among the backscatter signals simulated, the case using data and twiddle factors of type floating-point double performed the best, as expected, given that it provides the highest resolution of the signal.

Surprisingly, comparable BER performance is achieved for bit resolutions as low as four total bits with two fractional bits. BER performance then severely degrades for the cases of four total bits with three fractional bits ("Width: 4, Frac: 3") and two total bits with zero fractional bits ("Width: 2, Frac: 0"). These results suggest an interesting opportunity for OFDM backscatter implementations to leverage significantly reduced IFFT implementations. Not only can the data and twiddle word sizes be reduced, but many of the arithmetic cycles can be eliminated since in a single sideband implementation with relatively few carriers, many of the IFFT calculations result in zeros or near-zero values.

7.4 OFDM Measurements & Results

Measurements were performed to validate the power spectrum and wireless uplink capabilities of an OFDM backscatter design. The measurements were performed by implementing the simplified IFFT LUT architecture previously men-

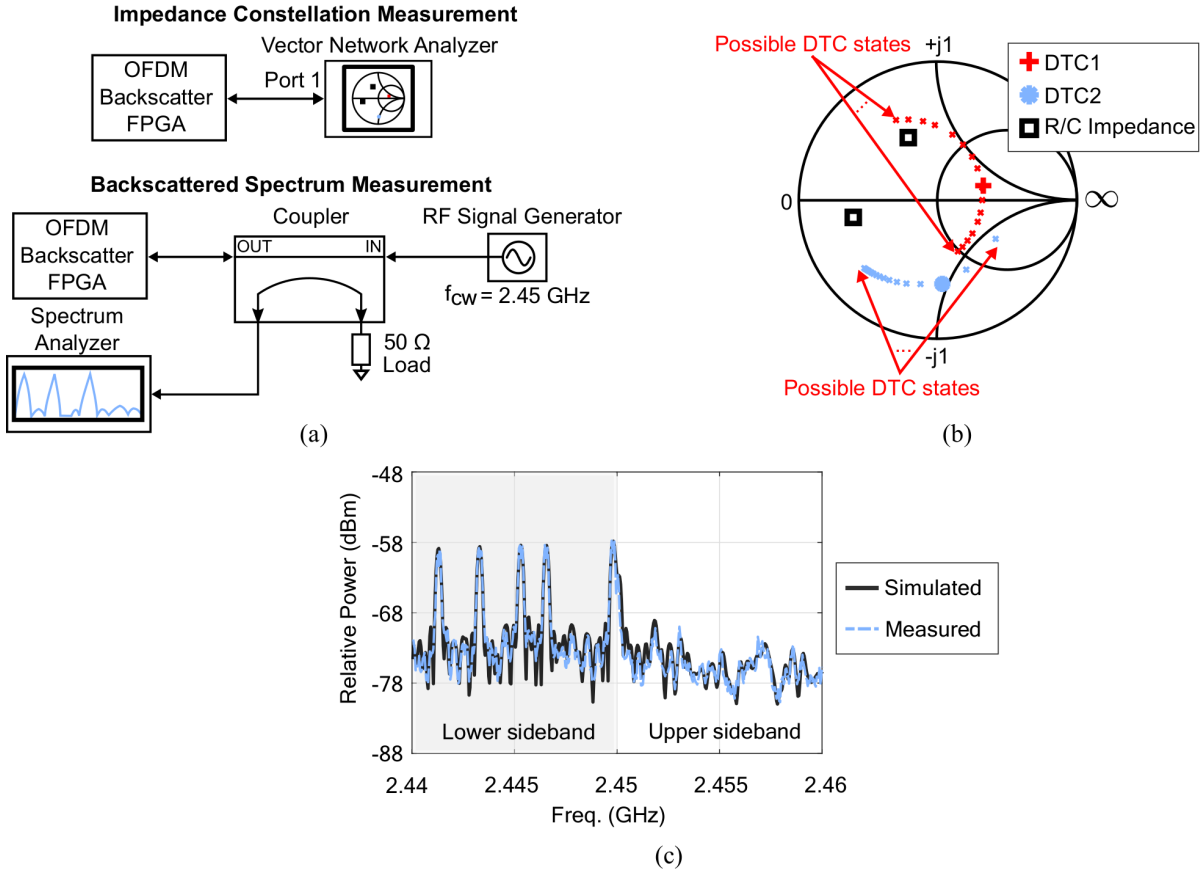

Figure 7.8: Measurement setup and results using four complex-valued impedances for SSB OFDM backscatter: (a) Diagram of the cabled setup used to measure the impedance constellation (top) and backscattered spectrum (bottom) of the OFDM backscatter FPGA, (b) Smith chart showing the measured impedances of the backscatter modulator normalized to 50 Ω.The impedances used for the measurement are shown with larger dots or crosses, while the possible DTC states are shown with smaller dots or crosses. (c) Comparison of the simulated backscatter spectrum using the measured impedance values and the measured spectrum from the OFDM backscatter FPGA.

tioned on a TinyFPGA BX [108], an open source hardware platform that uses a Lattice Semiconductor iCE40 FPGA. A block diagram of the digital design is shown in Fig. 7.7. The digital design was written in the Verilog hardware definition language and was comprised of a 19-bit linear feedback shift register (LFSR) to generate a pseudo-random data stream, a Symbol Clock generator set to trigger each new symbol at a 250 kHz symbol rate, and an OFDM Symbol LUT. The LUT was generated from 128-point IFFT and contains 64 total symbols each consisting of 128 samples. 32 of the symbols corresponding to the in-phase (I) output and 32 correspond to the quadrature (Q) output. Additionally, a serial peripheral interface (SPI) driver is used to initialize the backscatter modulator's DTCs on power-up.

7.4.1 Backscatter Modulator Design

A custom PCB was designed to interface the backscatter modulator to the FPGA. The backscatter modulator is implemented using a CMOS SP4T RF switch (Analog Devices ADG904 [102]) controlled by the FPGA, as shown in Fig. 7.2(b). The RF switch connects one of four impedances to the antenna. The impedances are implemented using two CMOS DTCs (Peregrine Semiconductor PE64101 and PE64909 [109]), and two fixed resistor-capacitor pairs. DTCs were used to achieve a reconfigurable inductor-free modulator that facilitates prototyping and design for future application specific integrated circuits (ASICs). The reflection coefficient of each impedance was measured at the reference plane of the antenna connector (Fig. 7.2(a)) using a calibrated Agilent N5222A vector network analyzer (VNA) (Fig. 7.5(a)). The tuning word for each DTC was iteratively reprogrammed until the reflection coefficients approximated the ideal SSB backscatter constellation in Fig. 7.5(c). A summary of the specific impedance values and DTC tuning words is presented in Table 7.2 and the measurement setup and Smith chart of the measured modulator impedance values at 2.45 GHz is shown in Fig. 7.8(a) and (b), respectively.

7.4.2 Modulator Power Consumption

The power consumption of the total OFDM Backscatter FPGA was measured with a precision Keithley power supply. The total power consumption (static + dynamic) of both the FPGA board and backscatter modulator PCB was $<$33.6 mW from a 3.5 V supply. Of the total power 33.0 mW (98.2%) is due to digital logic in the FPGA (Fig. 7.7), and only 600 μW (1.8%) is consumed by the backscatter modulator. Within the backscatter modulator PCB, the ADG904 RF switch consumed 200 μW while the DTCs together consumed 400 μW of power.

7.4.3 Measured Backscattered Spectrum

The OFDM backscatter spectrum was measured using the setup shown in Fig. 7.8(a). The OFDM backscatter FPGA assembly was connected to the output port of a Mini-Circuits ZABDC20-252H-S+ coupler using a coaxial cable. An Agilent N5181A RF signal generator was connected to the input port of the coupler and configured to generate a pure

Table 7.2: Backscatter modulator impedances used for the 2.4 GHz ISM band

	Impedance States			**DTC**
Z	**R Value**	**C Value**	**Γ** (Cartesian & Polar)	**Word**
Z_0	-	2.5 pF	0.02 - j0.70 (0.70$\angle$272°)	0x02
Z_1	-	1.45 pF	0.41 + j0.10 (0.42$\angle$13°)	0x08
Z_2	131 Ω	0.5 pF	-0.21 + j0.46 (0.51$\angle$115°)	-
Z_3	19.1 Ω	0.5 pF	0.61 + j0.12 (0.62$\angle$191°)	-

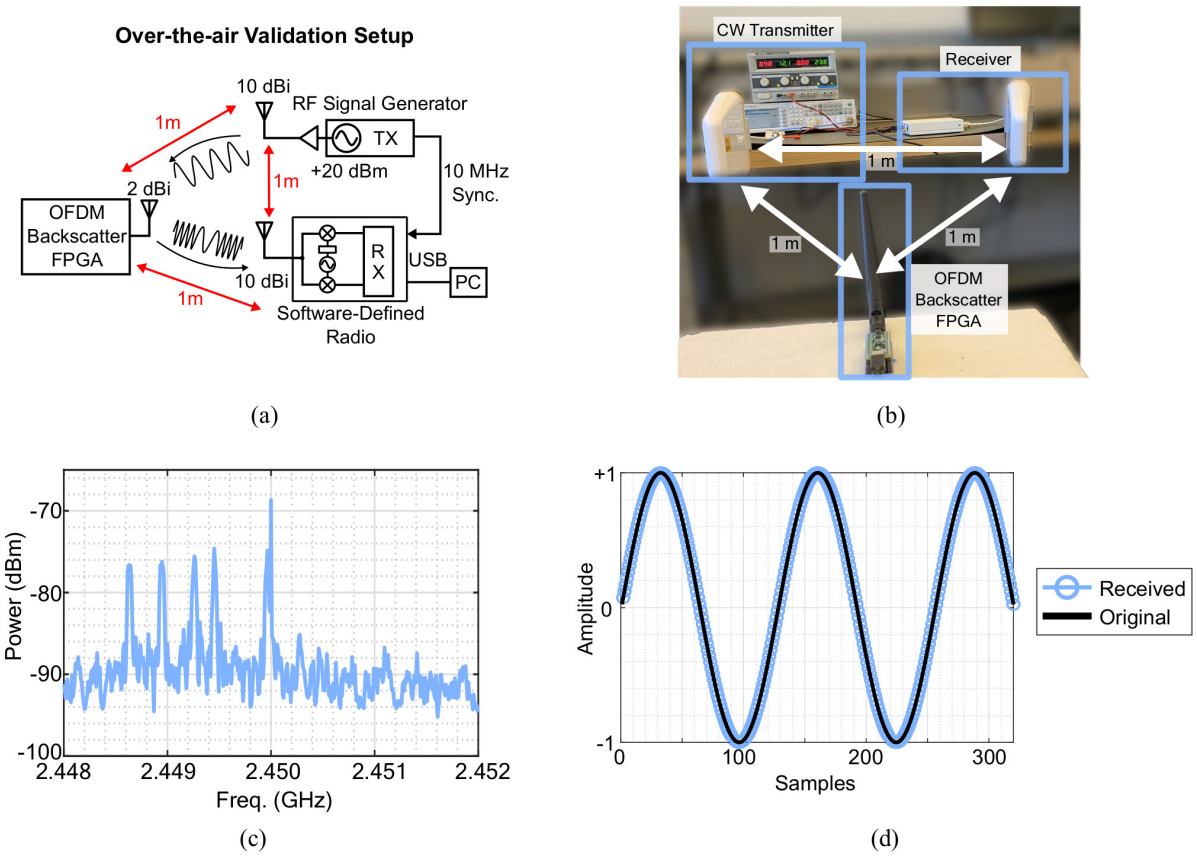

Figure 7.9: Measurement setup and results of over-the-air testing: (a) Diagram of the wireless test setup used to uplink data, (b) Photo of the test setup in a lab environment, (c) Measured over-the-air OFDM backscatter spectrum, (d) Measured over-the-air vs. original sampled-sine test data payload showing good agreement. No bit errors were observed in this data set.

carrier wave tone at 2.45 GHz and -20 dBm RF power. The output coupled port of the coupler was connected to an Agilent N9320B spectrum analyzer, with attenuation set to 0 dB and a resolution bandwidth of 100 kHz. The input coupled port of the coupler was terminated with a 50 Ω load. With the signal generator turned on, a pseudo-random sequence of OFDM symbols was generated using the 19-bit LFSR on the FPGA. A plot of the measured backscattered spectrum is shown in Fig 7.8(c). Overlaid on the plot is the simulated spectrum using the measured impedances shown in (b). As the plot shows, the measured spectrum shows good agreement with the simulation.

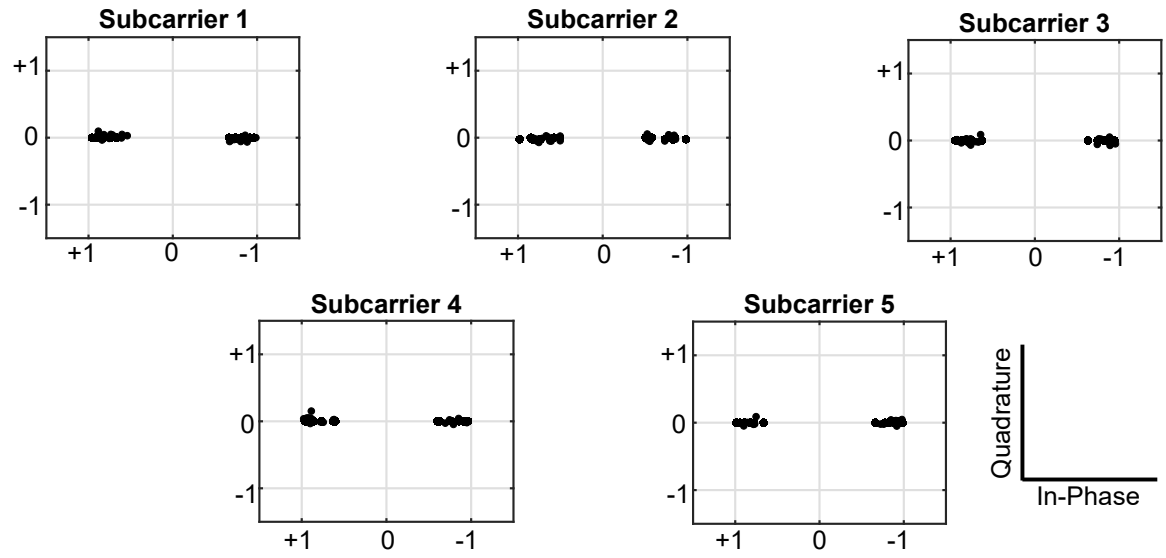

Figure 7.10: Subcarrier BPSK constellations from the over-the-air validation.

7.4.4 Over-the-air Validation

A wireless over-the-air measurement was performed to validate that OFDM backscatter symbols can be successfully demodulated. For the measurement, a bi-static backscatter communication setup with 1 meter spacing was used, as depicted in the block diagram and photo of Fig. 7.9(a) and (b), respectively. The external carrier wave (CW) was generated at 2.45 GHz using an Agilent N5181A RF signal generator with 0 dBm output power, a Mini Circuits ZRL-3500+ RF amplifier with a specified gain of 20 dB, and an L-Com HG72710LP-NF log periodic antenna with a specified gain of 10 dBi. The receiver was implemented using an Ettus Research USRP B210 software-defined radio (SDR), and an L-Com HG72710LP-NF log periodic antenna. The internal clock of the SDR was synchronized to the RF signal generator via a 10 MHz synchronization signal. A desktop PC running GNU Radio Companion ran the SDR and performed down conversion, I/Q balancing, sample and symbol synchronization, and decoding with a sample rate of 20 MSps. The OFDM backscatter FPGA was programmed using the design from Fig. 7.7 with two modifications: (1) the sample clock PLL frequency was reduced to 5 MHz in order to accommodate the maximum reliable sampling rate of the SDR and PC, and (2) the LFSR was replaced with a sinewave LUT (15-bit amplitude resolution, 128-bit phase resolution) to provide a realistic sensor-data-like payload. The sinewave LUT contained all 32 possible OFDM backscatter symbols and could thus be used to determine whether a receiver could distinguish each unique symbol. The measured over-the-air power spectrum is shown in Fig. 7.9(c) showing the OFDM backscatter subcarriers. The spectrum was measured using an Agilent N9320B spectrum analyzer with a resolution bandwidth of 1 kHz, the maximum hold function enabled, and averaging enabled over 10 sweeps. Several seconds of wireless data were captured, and a plot of the received samples is shown in Fig. 7.9(d) overlaid with the original samples. Plots of

Table 7.3: Comparison of State-of-the-Art OFDM Backscatter Designs

	Kimionis et al., 2016 [63][a]	Tang et al., 2018 [99]	Correia et al., 2018 [100]	**This Work, 2020**
Backscatter Modulator	FET/PIN Diode	FET	FET	**CMOS Switch**
Modulator Control Signal	Analog	Analog	Analog	**Digital**
Voltage DACs Required	Yes	Yes	Yes	**No**
No. of Subcarriers Demonstrated	N/A	4	4	**5**
Subcarrier Modulation	N/A	AFSK	4-QAM	**BPSK**
Demonstrated Operating Frequency	915 MHz	5.8 GHz	2.4 GHz	**2.4 GHz**

[a]Did not explicitly demonstrate OFDM backscatter.

the individual subcarrier BPSK constellations are shown in Fig. 7.10. Good agreement can be observed between the received and original samples, and no bit errors were detected, validating the feasibility of using OFDM backscatter to wirelessly uplink data.

7.5 Chapter Conclusions

This chapter introduces three all-digital architectures for OFDM backscatter modulation, as well as design analysis, simulations, and measurements for a hardware-efficient IFFT LUT architecture using five subcarriers with BPSK modulation to obtain a throughput of 250 kSymbols/s (1.25 Mbits/s). The hardware implementation uses a low-cost, open-source FPGA platform and a backscatter modulator on a custom PCB. The digital design requires 505 logic elements with no multipliers nor any block RAM. Measurements found that the total power consumption of the device was less than 33.6 mW, dominated by FPGA static power consumption, with a backscatter modulator power consumption of only 200 μW, yielding a modulator energy consumption of 160 pJ/bit. RF measurements using a cabled backscatter setup found good agreement between the physical design and simulated backscattered spectrum.

Wireless over-the-air measurements validated that data can be successfully recovered without error from the OFDM backscatter symbols.

Simulations of different backscatter modulator configurations were performed to determine the impact of impedance DAC resolution on the backscattered OFDM spectrum. In general, it was found that the highest backscattered subcarrier power is achieved using single sideband backscatter modulation with > 2 modulator states and the greatest possible distance between impedance states. As the number of modulator states is increased, the impedance DAC resolution increases and the subcarrier interference ratio (SIR) and sideband rejection ratio (SRR) similarly increase. Interestingly, as the number of modulator states increases from four to sixteen, the average distance between impedance states decreases, decreasing the total backscattered power. This suggests that one should carefully consider the increased cost and power consumption required to implement e.g. a 16-state backscatter modulator for OFDM implementations.

Additionally the OFDM backscatter BER performance was simulated using different fixed-point word resolutions in the IFFT. These simulations revealed that comparable performance (within approximately 1 dB for BER of 10^{-4}) can be achieved between bit lengths of 4 to 16 bits. This suggests that optimal IFFT architectures can be developed for backscatter radios that could further reduce resource utilization and power consumption.

The designs and analysis in this chapter point the way toward low-complexity, low power wireless sensor nodes leveraging OFDM backscatter. Future work will explore physical and link layer schemes using the architectures presented here. With control of the subcarrier placement and modulation, multi-carrier, multi-protocol backscatter uplinks could be implemented to improve data throughput, multiple access, resilience to interference, and compatibility with custom and off-the-shelf receivers. Additionally, based on our findings that OFDM backscatter can operate with a low-resolution IFFT, optimizations can be investigated to further reduce resource utilization and quantify performance in non-ideal channels. Such a low-resource IFFT could greatly expand the applicability of low power, highly configurable OFDM backscatter based wireless sensors.

Chapter 8

CONCLUSIONS & FUTURE WORK

8.1 Conclusions

In this dissertation, we presented the NeuroDisc, a new research platform for wirelessly streaming neural data. The NeuroDisc leverages an energy efficient, low SWaP, backscatter-based wireless uplink architecture to address the challenge of wirelessly streaming high resolution neural telemetry from an implanted electrode array. The NeuroDisc was validated through *in vivo* wireless neural measurements with an anesthetized pigtail macaque. In working towards the goal of enhancing neural recording and stimulation devices, we have contributed new designs, techniques, analysis, and technology demonstrations to the fields of low power wireless sensing and backscatter communication. These contributions improve the energy efficiency, data throughput, platform flexibility, and reliability of backscatter communication, and open new avenues for innovation in biomedical engineering, as well as other SWaP-constrained wireless sensing applications.

For high resolution sampling applications, we presented an approach using quadrature backscatter modulation to

Table 8.1: Summary of Contributions

Chapter	**Modulation Control Signal**	**Modulation Scheme**	**Data Rate**	**Data protocol**	**Energy per bit**
2	All-digital	DQPSK	25 Mbps	Custom	12.4 pJ/bit
3	All-digital	FSK Dual Sideband	1 Mbps	BLE	158 pJ/bit
3	All-digital	FSK Single Sideband	1 Mbps	BLE	198 pJ/bit
4	All-digital	Dual-Mode FSK & DQPSK	1 Mbps & 6.25 Mbps	BLE & Custom	198 & 12.4 pJ/bit
7	All-digital	OFDM	1.25 Mbps	Custom	160 pJ/bit

improve the wireless throughput of a BCI while maintaining high energy efficiency. This technique was demonstrated *in vivo* to stream 16 channels of neural data at 25 Mbps from the primary motor cortex of anesthetized rhesus macaque using the 915 MHz industrial, scientific, and medical (ISM) band at a distance of 35 cm. The per-bit energy efficiency of the backscatter modulator was measured to be 12.4 pJ/bit, which is nearly 100X lower than comparable off-the-shelf solutions (e.g. WiFi, Bluetooth) achieving similar data rates.

A wireless neural recorder should ideally minimize the cost and effort for researchers to collect data. The DQPSK backscatter uplink required a semi-custom receiver that could increase the cost and logistical complexity for experimenters unfamiliar with RF systems. To improve the usability of the backscatter uplink, we presented the first fully-digital Bluetooth Low Energy (BLE) backscatter uplink for streaming wireless telemetry to any BLE-compatible device (e.g. smartphones, laptops, tablets, etc), achieving per-bit energy efficiencies between 158-198 pJ/bit (Table 8.1). We provided a design and simulation framework for implementing single sideband (SSB) BLE backscatter modulation using the digital phasing method. Within this framework, we provided analysis for how non-idealities in the modulator impedances affect opposite sideband suppression. Despite non-idealities, our off-the-shelf design achieved a desired sideband gain of 2.4 dB and a sideband rejection ratio of 12 dB while consuming 198 pJ/bit, representing a significant RF performance improvement over existing double sideband modulation for only a small increase in per-bit energy consumption. We presented an end-to-end laboratory validation of this system demonstrating wireless over-the-air streaming of pre-recorded neural data.

The BLE backscatter uplink had a data rate of 1.0 Mbps, which is adequate for capturing multiple channels of local field potentials but not for higher resolution action potentials. To provide the benefits of both the high rate 915 MHz DQPSK uplink and the 2.4 GHz BLE-compatible 1.0 Mbps uplink, we demonstrated a time division multiplexed approach to simultaneous BLE and DQPSK operation that required no hardware modifications to the NeuroDisc. The system leveraged the wideband operation of the NeuroDisc's RF switch-based modulator to stream telemetry in two unlicensed frequency bands. This system demonstrated the flexibility of backscatter communication systems to operate across wide frequency bands with multiple protocols, an advantage that is often overlooked in the literature and which could provide added benefits to end users.

A drawback to backscatter uplinks is the less favorable link budget, particularly in multipath environments. The dense multipath interference observed inside metal non-human primate cages can significantly reduce the reliability of backscatter uplinks for wireless neural recorders. In addition to providing measurements of the channel transfer function (CTF) in the 915 MHz and 2.4 GHz bands within a metal NHP cage, we presented two novel mitigation strategies. One approach for reducing nulls in the CTF was to modify the electromagnetic environment using electronic mode stirring. By electronically actuating planar switched parasitic antennas (SPAs) installed along the cage ceiling, we demonstrated for both the 915 MHz and 2.4 GHz ISM bands that it is possible to favorably alter the electromagnetic boundary conditions of the cage, improving the CTF and yielding a more favorable link budget.

The other approach was to design a wideband modulation scheme that reduces sensitivity to time varying multipath interference. We presented three all-digital architectures for generating orthogonal frequency division multiplexing (OFDM) backscatter modulation. A key innovation presented was to use an RF switch as a low-resolution impedance digital-to-analog converter (DAC), providing significant energy and complexity savings compared to the voltage DACs commonly used for OFDM modulation. Even with one bit of resolution provided by a single pole-single throw (SPST) switch, we demonstrated that it is possible to generate multi-tone OFDM backscatter signals. We provided the design, analysis, simulations, and over-the-air validation for an inverse Fast Fourier Transform (IFFT)-based architecture, pointing the way towards low power, low complexity backscatter uplinks with improved resilience to multipath interference.

8.2 Future Work

This dissertation has presented new approaches for backscatter communication that could enable next-generation wireless uplinks for neural prosthetics and other SWaP-constrained devices. Building off this work, there are several interesting avenues to explore.

8.2.1 Migrating from an FPGA to an Application Specific Integrated Circuit (ASIC)

A key step for harnessing the SWaP advantages of backscatter communication will be to integrate the digital designs onto a single chip. The DQPSK, BLE-compatible FSK, and OFDM modulations presented were all implemented as digital devices using commercial off-the-shelf FPGAs. The Verilog HDL code used to implement these designs could be synthesized as part of a neural recording ASIC, and we expect that total power consumption of the backscatter uplink would consume on the order of 100s of microwatts or less, including backscatter modulation and digital packet handling. Further size reduction could be achieved by using inductor free impedance constellations explored in [61, 101]. Paired with advancements in conformable electronics, a single chip solution could enable high resolution monitoring of neural systems in stable, minimally invasive packages.

8.2.2 Combinging Conventional and Backscatter Wireless Uplinks in a Hybrid Design

The less favorable link budget of backscatter communication uplinks limits their achievable range. A dual-mode device that dynamically changes between conventional and backscatter communication, such as the design in [98], could improve reliability at long distances while improving energy savings at short ranges. By combining conventional and backscatter uplinks, greater versatility could be achieved when long ranges are required.

8.2.3 Improving Receiver Sensitivity by Reducing CW Interference

A key approach to improving the reliability of backscatter communication systems is to reduce the interference caused by the external carrier wave (CW) at the receiver. Whether the CW is in-band as with the DQPSK NeuroDisc uplink in Chapter 2, or out of band as the BLE NeuroDisc uplink in Chapter 3, reducing the strength of the unmodulated CW can improve receiver sensitivity and packet success rate [67, 70, 79]. The sensitivity of the DQPSK backscatter receiver presented in Chapter 2 could be improved by modifying the self-jammer canceller. Steps could include integrating the components onto a single PCB to reduce parasitic losses and improve isolation from radiated noise, e.g. from digital electronics and mains power. The self-jammer canceller could also be used for BLE and OFDM backscatter modulations to increase receiver sensitivity.

8.2.4 Support for Multiple Devices Streaming Simultaneously via Multiple Access Protocols

Future deployments of backscatter communication will need to support multiple devices sharing the same wireless channel. The all-digital OFDM architectures presented in Chapter 7 could be used to explore physical- and link-layer multiple access protocols. With control of the subcarrier placement and modulation, frequency and code division multiplexing could be explored as methods to allow simultaneous communication from multiple devices.

8.2.5 Dynamic Mode Stirring for Freely Moving Experiments

To implement real-time mode stirring optimization, a closed-loop optimization approach could be implemented where the mode stirring configuration is selectively changed to maximize the received backscatter signal power as the NHP moves around the cage.

Other intriguing permutations of the switched parasitic antennas (SPAs) and mode stirring assemblies could be explored in future research. For example, additional SPAs could be placed on the back wall of the cage (along row A, Fig. 6.2) in addition to the cage ceiling to determine whether electronic mode stirring could reduce sensitivity to BCI orientation. Future work could also explore whether improved performance might be achieved with the use of additional impedance states, e.g. using a single-pole-four-throw switch such as the Analog Devices ADG904 to yield a finer granularity of the phase of reflection at each SPA. Rather than using CMOS RF switch technologies with relatively high insertion loss ($>$1 dB), gallium arsenide (GaAs) RF switches with lower two-way insertion loss ($<$1 dB) could be explored as well.

8.2.6 Increased Reliability via Channel Equalization

With the integration of a low power receiver, such as the one proposed in [70], the OFDM backscatter communication architecture in Chapter 7 could be modified to compensate for dynamic phase and amplitude changes in the wireless

channel. Channel compensation could enable higher data rate communications in multipath environments, opening up new applications for backscatter communication in wireless sensing.

8.2.7 Size and Power Reduction via Efficient Digital Hardware

Based on our findings presented in Chapter 7 that OFDM backscatter can operate with a low-resolution IFFT, optimizations can be investigated to further reduce resource utilization and quantify performance in non-ideal channels. Such a low-resource IFFT could greatly expand the applicability of low power, highly configurable OFDM backscatter based wireless sensors.

8.3 List of Relevant Publications

Publications Under Review

1. **J. Rosenthal**, A. Pike, S. Reyes, and M.S. Reynolds, "Electronic Mode Stirring for Improved Backscatter Communication Link Margin in a Reverberant Cavity Animal Cage Environment," submitted to *IEEE Transactions on Antennas and Propagation* in Jan. 2021, in revision.

Peer-reviewed Journal Publications

4. **J. Rosenthal** and M.S. Reynolds, "Hardware-Efficient All-Digital Architectures for OFDM Backscatter Modulators," in *IEEE Transactions on Microwave Theory and Techniques*, vol. 69, no. 1, pp. 803-811, Jan. 2021.

3. **J. Rosenthal** and M. S. Reynolds, "A 1.0-Mb/s 198-pJ/bit Bluetooth Low-Energy Compatible Single Sideband Backscatter Uplink for the NeuroDisc Brain-Computer Interface," in *IEEE Transactions on Microwave Theory and Techniques*, vol. 67, no. 10, pp. 4015-4022, Oct. 2019.

2. **J. Rosenthal**, A. Sharma, E. Kampianakis and M. S. Reynolds, "A 25 Mbps, 12.4 pJ/bit DQPSK Backscatter Data Uplink for the NeuroDisc Brain Computer Interface," in *IEEE Transactions on Biomedical Circuits and Systems*, vol. 13, no. 5, pp. 858-867, Oct. 2019.

1. A. Sharma, E. Kampianakis, **J. Rosenthal**, A. Pike, A. Dadkhah and M. S. Reynolds, "Wideband UHF DQPSK Backscatter Communication in Reverberant Cavity Animal Cage Environments," in *IEEE Transactions on Antennas and Propagation*, vol. 67, no. 8, pp. 5002-5011, Aug. 2019.

Peer-reviewed Conference Publications

9. **J. Rosenthal** and M.S. Reynolds, "On-the-fly Adaptation of Backscatter Modulator Impedances Using Digitally-Tuned Capacitors," *2021 IEEE Topical Conference on Wireless Sensors and Sensor Networks (WiSNet)*, Virtual, 2021, pp. 5-7.

8. T. Petrie, **J. Rosenthal**, and M.S. Reynolds, "A Low-Cost 1 Mbps Frequency Shift Keying Backscatter Receiver and Carrier Wave Generator System for Wireless Neural Recording," *2020 IEEE International Conference on RFID (RFID)*, Virtual, 2020, pp. 1-5.

7. **J. Rosenthal** and M.S. Reynolds, "A Dual-Band Shared-Hardware 900 MHz 6.25 Mbps DQPSK and 2.4 GHz 1.0 Mbps Bluetooth Low Energy (BLE) Backscatter Uplink for Wireless Brain-Computer Interfaces," *IEEE Conference on RFID*, Virtual, 2020, pp. 1-6.

6. **J. Rosenthal** and M.S. Reynolds, "All-Digital Single Sideband (SSB) Bluetooth Low Energy (BLE) Backscatter with an Inductor-free, Digitally-Tuned Capacitance Modulator," *IEEE International Microwave Symposium*, Virtual, 2020, pp. 468-471.

5. L. Arjona, **J. Rosenthal**, J.R. Smith, and C.T. Moritz, "High Performance Flexible Protocol for Backscattered-based Neural Implants," in *2019 IEEE-APS Topical Conference on Antennas and Propagation in Wireless Communications (APWC)*, 2019, pp. 276-280.

4. **J. Rosenthal**, A. Pike and M. S. Reynolds, "A 1 Mbps 158 pJ/bit Bluetooth Low Energy (BLE) Compatible Backscatter Communication Uplink for Wireless Neural Recording in an Animal Cage Environment," *2019 IEEE International Conference on RFID (RFID)*, Phoenix, AZ, USA, 2019, pp. 1-6.

3. **J. Rosenthal** and M. S. Reynolds, "A 158 pJ/bit 1.0 Mbps Bluetooth Low Energy (BLE) Compatible Backscatter Communication System for Wireless Sensing," *2019 IEEE Topical Conference on Wireless Sensors and Sensor Networks (WiSNet)*, Orlando, FL, USA, 2019, pp. 1-3.

2. A. Dadkhah, **J. Rosenthal**, and M. S. Reynolds, "ZeroScatter: Zero-Added-Component Backscatter Communication Using Existing Digital I/O Pins," *2019 IEEE Topical Conference on Wireless Sensors and Sensor Networks (WiSNet)*, Orlando, FL, USA, 2019, pp. 1-3.

1. **J. Rosenthal**, E. Kampianakis, A. Sharma and M. S. Reynolds, "A 6.25 Mbps, 12.4 pJ/bit DQPSK Backscatter Wireless Uplink for the NeuroDisc Brain-Computer Interface," *2018 IEEE Biomedical Circuits and Systems Conference (BioCAS)*, Cleveland, OH, 2018, pp. 1-4.

BIBLIOGRAPHY

[1] American Institute for Medical and Biological Engineering. Medical and biological engineering in the next 20 years: The promise and the challenges. *IEEE Transactions on Biomedical Engineering*, 60(7):1767–1775, 2013.

[2] J. C. Kao, S. D. Stavisky, D. Sussillo, P. Nuyujukian, and K. V. Shenoy. Information systems opportunities in brainmachine interface decoders. *Proceedings of the IEEE*, 102(5):666–682, 2014.

[3] G. Anumanchipalli, J. Chartier, and E. Chang. Speech synthesis from neural decoding of spoken sentences. *Nature*, 568:493–498, 04 2019.

[4] F. B. Wagner et al. Targeted neurotechnology restores walking in humans with spinal cord injury. *Nature*, 563(7729):65–71, 2018.

[5] F. Inanici, S. Samejima, P. Gad, V. R. Edgerton, C. P. Hofstetter, and C. T. Moritz. Transcutaneous electrical spinal stimulation promotes long-term recovery of upper extremity function in chronic tetraplegia. *IEEE Transactions on Neural Systems and Rehabilitation Engineering*, 26(6):1272–1278, 2018.

[6] J.L. Abelson, G.C. Curtis, O. Sagher, R.C. Albucher, M. Harrigan, S.F. Taylor, B. Martis, and B. Giordani. Deep brain stimulation for refractory obsessive-compulsive disorder. *Biological Psychiatry*, 57(5):510–6, 2005.

[7] European Research Council. EU brain research. *EU support for research and innovation in the area of the brain*, Jul 2020.

[8] Defense Advanced Research Projects Agency (DARPA). DARPA awards contracts for work on spinal cord injury treatment. *DARPA News*, Nov 2020.

[9] T. Bjorninen, R. Muller, P. Ledochowitsch, L. Sydanheimo, L. Ukkonen, M. M. Maharbiz, and J. M. Rabaey. Design of wireless links to implanted brainmachine interface microelectronic systems. *IEEE Antennas and Wireless Propagation Letters*, 11:1663–1666, 2012.

[10] A. Sharma, E. Kampianakis, and M. S. Reynolds. A dual-band HF and UHF antenna system for implanted neural recording and stimulation devices. *IEEE Antennas and Wireless Propagation Letters*, 16:493–496, 2017.

[11] C. Pandarinath et al. High performance communication by people with paralysis using an intracortical brain-computer interface. *eLife*, 6:e18554, Feb 2017.

[12] A. Jackson, J. Mavoori, and E. E. Fetz. Correlations between the same motor cortex cells and arm muscles during a trained task, free behavior, and natural sleep in the macaque monkey. *Physiology*, 97(1):360–374, Jan. 2007.

[13] A. Burton, S. N. Obaid, A. Vázquez-Guardado, M. B. Schmit, T. Stuart, L. Cai, Z. Chen, I. Kandela, C. R. Haney, E. A. Waters, H. Cai, J. A. Rogers, L. Lu, and P. Gutruf. Wireless, battery-free subdermally implantable photometry systems for chronic recording of neural dynamics. *Proceedings of the National Academy of Sciences of the United States of America*, 117(6):2835–2845, 2020.

[14] T. Ibrahim, D. Abraham, and R. Rennaker. Electromagnetic power absorption and temperature changes due to brain machine interface operation. *Annals of Biomedical Engineering*, 35:825–834, 2007.

[15] P. D. Wolf. *Indwelling Neural Implants: Strategies for Contending with the In Vivo Environment*. CRC Press/Taylor & Francis, Boca Raton, FL, 2008.

[16] J. Rosenthal, A. Sharma, E. Kampianakis, and M. S. Reynolds. A 25 Mbps, 12.4 pJ/b DQPSK backscatter data uplink for the NeuroDisc brain-computer interface. *IEEE Transactions on Biomedical Circuits and Systems*, 13(5):858–867, Oct. 2019.

[17] S. J. Thomas, R. R. Harrison, A. Leonardo, and M. S. Reynolds. A battery-free multichannel digital neural/EMG telemetry system for flying insects. *IEEE Transactions on Biomedical Circuits and Systems*, 6(5):424–436, Oct 2012.

[18] S. Naderiparizi, A. N. Parks, Z. Kapetanovic, B. Ransford, and J. R. Smith. Wispcam: A battery-free RFID camera. In *Proceedings of the 2015 IEEE International Conference on RFID*, pages 166–173, 2015.

[19] A. Sharma, E. Kampianakis, J. Rosenthal, A. Pike, A. Dadkhah, and M. S. Reynolds. Wideband UHF DQPSK backscatter communication in reverberant cavity animal cage environments. *IEEE Transaction on Antennas and Propagation*, 67(8):5002–5011, Feb. 2019.

[20] E. V. Evarts. Temporal patterns of discharge of pyramidal tract neurons during sleep and waking in the monkey. *Physiology*, 27(2):152–171, Mar. 1964.

[21] G. Corder, B. Ahanonu, B. F. Grewe, D. Wang, M. J. Schnitzer, and G. Scherrer. An amygdalar neural ensemble that encodes the unpleasantness of pain. *Science*, 363(6424):276–281, 2019.

[22] W. Taube, M. Mouthon, C. Leukel, H. Hoogewoud, J. Annoni, and M. Keller. Brain activity during observation and motor imagery of different balance tasks: An fMRI study. *Cortex*, 64:102–114, 2015.

[23] T. Deffieux, C. Demene, M. Pernot, and M. Tanter. Functional ultrasound neuroimaging: a review of the preclinical and clinical state of the art. *Current Opinion in Neurobiology*, 50:128–135, 2018. Neurotechnologies.

[24] A. P. Georgopoulos, J. F. Kalaska, R. Caminiti, and J. T. Massey. On the relations between the direction of two-dimensional arm movements and cell discharge in primate motor cortex. *Journal of Neuroscience*, 2(11):1527–1537, 1982.

[25] P. D. Cheney and E. E. Fetz. Functional classes of primate corticomotorneuronal cells and their relation to active force. *Journal of Neurophysiology*, 44(4):773–791, 1980.

[26] T. N. Aflalo and M. S. A. Graziano. Partial tuning of motor cortex neurons to final posture in a free-moving paradigm. *Proceedings of the National Academy of Sciences of the United States of America*, 103(8):2909–2914, Feb. 2006.

[27] L. R. Hochberg, D. Bacher, B. Jarosiewics, N. Y. Masse, J. D. Simeral, J. Vogel, S. Haddadin, J. Liu, S. S. Cash, P. Van der Smagt, and J. P. Donoghue. Reach and grasp by people with tetraplegia using a neurally controlled robotic arm. *Nature*, 485:372–375, May 2012.

[28] J. L. Collinger, B. Wodlinger, J. E. Downey, W. Wang, E. C. Tyler-Kabara, D. J. Weber, A. J. C. McMorland, M. Velliste, M. L. Boninger, and A. B. Schwartz. High-performance neuroprosthetic control by an individual with tetraplegia. *The Lancet*, 381(9866):557–564, 2013.

[29] N. C. Swann, C. de Hemptinne, M. C. Thompson, et al. Adaptive deep brain stimulation for Parkinson's disease using motor cortex sensing. *Journal of Neural Engineering*, 15(4), 2018.

[30] Defense Advanced Research Projects Agency. DARPA and the Brain Initiative, 2019. https://www.darpa.mil/program/our-research/darpa-and-the-brain-initiative.

[31] C. A. Chestek, V. Gilja, P. Nuyujukian, R. J. Kier, F. Solzbacher, S. I. Ryu, R. R. Harrison, and K. V. Shenoy. Hermesc: Low-power wireless neural recording system for freely moving primates. *IEEE Transactions on Neural Systems and Rehabilitation Engineering*, 17(4):330–338, 2009.

[32] S. Zanos, A. G. Richardson, L. Shupe, F. P. Miles, and E. E. Fetz. The Neurochip-2: An autonomous head-fixed computer for recording and stimulating in freely behaving monkeys. *IEEE Transactions on Neural Systems and Rehabilitation Engineering*, 19(4):427–435, 2011.

[33] M. Yin et al. Wireless neurosensor for full-spectrum electrophysiology recordings during free behavior. *Neuron*, 84(6):1170–1182, Dec 2014.

[34] R. Muller, H. Le, W. Li, P. Ledochowitsch, S. Gambini, T. Bjorninen, A. Koralek, J. M. Carmena, M. M. Maharbiz, W. Alon, and J. M. Rabaey. A minimally invasive 64-channel wireless μECoG implant. *IEEE Journal of Solid-State Circuits*, 50(1):344–359, 2015.

[35] X. Liu, M. Zhang, A. G. Richardson, T. H. Lucas, and J. Van der Spiegel. Design of a closed-loop, bidirectional brain machine interface system with energy efficient neural feature extraction and PID control. *IEEE Transactions on Biomedical Circuits and Systems*, 11(4):729–742, Aug 2017.

[36] San Disk Corporation. San disk microSD: OEM Product Manual, Section 2.1.1 Typical Card Power Requirements, 2010. https://www.alliedelec.com/m/d/04db416b291011446889dbd6129e2644.pdf.

[37] J. A. Fernandez-Leon, A. Parajuli, R. Franklin, M. Sorenson, D. J. Felleman, B. J. Hansen, M. Hu, and V. Dragoi. A wireless transmission neural interface system for unconstrained non-human primates. *J. Neural Eng*, 12(5):056005, Oct 2015.

[38] R. Matthes. ICNIRP Guidelines for limiting exposure to time-varying electric, magnetic and electromagnetic fields (up to 300 GHz). *Health Physics*, 4:494–522, 1998.

[39] P.J. Dimbylow and S.M. Mann. SAR calculations in an anatomically realistic model of the head for mobile communication transceivers at 900 MHz and 1.8 GHz. *Physics in Medicine and Biology*, 39(10):1537, 1994.

[40] S. J. Thomas and M. S. Reynolds. A 96 Mbit/sec, 15.5 pJ/bit 16-QAM modulator for UHF backscatter communication. In *Proceedings of the 2012 IEEE International Conference on RFID*, pages 185–190, Apr 2012.

[41] J. F. Ensworth and M. S. Reynolds. Every smart phone is a backscatter reader: Modulated backscatter compatibility with Bluetooth 4.0 Low Energy (BLE) devices. In *Proceedings of the 2015 IEEE International Conference on RFID*, 2015.

[42] A. Ebrazeh and P. Mohseni. 30 pJ/b, 67 Mbps, centimeter-to-meter range data telemetry with an IR-UWB wireless link. *IEEE Transactions on Biomedical Circuits and Systems*, 9(3):362–369, June 2015.

[43] D. Kim, M. A. Ingram, and W. W. Smith. Measurements of small-scale fading and path loss for long range RF tags. *IEEE Transactions on Antennas and Propagation*, 51(8):1740–1749, 2003.

[44] J. D. Griffin and G. D. Durgin. Complete link budgets for backscatter-radio and RFID systems. *IEEE Antennas and Propagation Magazine*, 51(2):11–25, Apr 2009.

[45] J. Rosenthal and M. S. Reynolds. A 158 pJ/bit 1.0 Mbps Bluetooth Low Energy (BLE) compatible backscatter communication system for wireless sensing. In *Proceedings of the 2019 IEEE Topical Conference on Wireless Sensors and Sensor Networks (WiSNet)*, pages 1–3, Jan 2019.

[46] J. Rosenthal and M. S. Reynolds. A 1.0-Mb/s 198-pJ/bit Bluetooth Low-Energy compatible single sideband backscatter uplink for the NeuroDisc braincomputer interface. *IEEE Transactions on Microwave Theory and Techniques*, 67(10):4015–4022, Oct. 2019.

[47] J. Rosenthal and M. S. Reynolds. Hardware-efficient all-digital architectures for OFDM backscatter modulators. *IEEE Transactions on Microwave Theory and Techniques*, 69(1):803–811, Dec. 2020.

[48] Intan Technologies, LLC. RHS2000 series digital stimulator and amplifier chips, 2019. http://intantech.com/.

[49] D.A. Schwarz, M.A. Lebedev, T.L. Hanson, D.F. Dimitrov, G. Lehew, J. Meloy, S. Rajangam, V. Subramanian, P.J. Ifft, Z. Li, et al. Chronic, wireless recordings of large-scale brain activity in freely moving rhesus monkeys. *Nature Methods*, 11(6):670, 2014.

[50] H. Ando, K. Takizawa, T. Yoshida, K. Matsushita, M. Hirata, and T. Suzuki. Wireless multichannel neural recording with a 128-Mbps UWB transmitter for an implantable brain-machine interfaces. *IEEE Transactions on Biomedical Circuits and Systems*, 10(6):1068–1078, Dec 2016.

[51] K. Teng, T. Wu, X. Liu, Z. Yang, and C. Heng. A 400 MHz wireless neural signal processing IC with 625 $\times$ on-chip data reduction and reconfigurable BFSK/QPSK transmitter based on sequential injection locking. *IEEE Transaction on Biomedical Circuits and Systems*, 11(3):547–557, June 2017.

[52] J. Xu, A. T. Nguyen, W. Zhao, H. Guo, T. Wu, H. Wiggins, E. W. Keefer, H. Lim, and Z. Yang. A low-noise, wireless, frequency-shaping neural recorder. *IEEE Transactions on Emerging and Selected Topics in Circuits and Systems*, 8(2):187–200, June 2018.

[53] J. Rosenthal, A. Pike, and M. S. Reynolds. A 1 Mbps 158 pJ/bit Bluetooth Low Energy (BLE) compatible backscatter communication uplink for wireless neural recording in an animal cage environment. In *Proceedings of the 2019 IEEE International Conference on RFID*, pages 1–6, 2019.

[54] J. Rosenthal, E. Kampianakis, A. Sharma, and M. S. Reynolds. A 6.25 Mbps, 12.4 pJ/bit DQPSK backscatter wireless uplink for the NeuroDisc brain-computer interface. In *Proceedings of the 2018 IEEE Biomedical Circuits and Systems Conference (BioCAS)*, Oct 2018.

[55] A. Shirane, H. Tan, Y. Fang, T. Ibe, H. Ito, N. Ishihara, and K. Masu. A 5.8 GHz RF-powered transceiver with a 113 μW 32-QAM transmitter employing the IF-based quadrature backscattering technique. In *Proceedings of the 2015 IEEE International Solid-State Circuits Conference - (ISSCC) Digest of Technical Papers*, pages 1–3, Feb 2015.

[56] Fetz Lab. NeuroChip3, 2019. depts.washington.edu/fetzweb/neurochip3.html.

[57] A. Sharma. *Dual-band power and communication antennas for wireless brain-computer interfaces*. PhD thesis, University of Washington, 2019.

[58] CST. CST Microwave Studio, 2019. cst.com/products/cstmws.

[59] Intel. Intel MAX10 FPGA, 2019. intel.com/content/www/us/en/products/programmable.html.

[60] R. W. Hamming. Error detecting and error correcting codes. *The Bell System Technical Journal*, 29(2):147–160, Apr 1950.

[61] S. J. Thomas, E. Wheeler, J. Teizer, and M. S. Reynolds. Quadrature amplitude modulated backscatter in passive and semipassive UHF RFID systems. *IEEE Transactions on Microwave Theory and Techniques*, 60(4):1175–1182, Apr 2012.

[62] R. Correia, A. Boaventura, and N. Borges Carvalho. Quadrature amplitude backscatter modulator for passive wireless sensors in IoT applications. *IEEE Transactions on Microwave Theory and Techniques*, 65(4):1103–1110, Apr 2017.

[63] J. Kimionis and M. M. Tentzeris. Pulse shaping: The missing piece of backscatter radio and RFID. *IEEE Transactions on Microwave Theory and Techniques*, 64(12):4774–4788, Dec 2016.

[64] A. Dadkhah, J. Rosenthal, and M. S. Reynolds. ZeroScatter: Zero-added-component backscatter communication using existing digital I/O pins. In *Proceedings of the 2019 IEEE Topical Conference on Wireless Sensors and Sensor Networks (WiSNet)*, pages 1–3, Jan. 2019.

[65] K. Kurokawa. Power waves and the scattering matrix. *IEEE Transactions on Microwave Theory and Techniques*, 13(2):194–202, Mar 1965.

[66] P. V. Nikitin, K. V. S. Rao, and R. D. Martinez. Differential RCS of RFID tag. *Electronics Letters*, 43(8):431–432, 2007.

[67] E. Kampianakis. *High data-rate ultra low-power backscatter wireless communication systems for brain-computer interfaces*. PhD thesis, University of Washington, 2019.

[68] S. Thomas and M. S. Reynolds. QAM backscatter for passive UHF RFID tags. In *Proceedings of the 2010 IEEE International Conference on RFID*, pages 210–214, Apr 2010.

[69] F. J. Chaure, H. G. Rey, and R. Quian Quiroga. A novel and fully automatic spike-sorting implementation with variable number of features. *Journal of Neurophysiology*, 120(4):1859–1871, 2018.

[70] J. F. Ensworth. *Ultra-low-power Bluetooth Low Energy (BLE) compatible backscatter communication and energy harvesting for battery-free wearable devices*. PhD thesis, University of Washington, December 2016.

[71] V. Iyer, V. Talla, B. Kellogg, S. Gollakota, and J. Smith. Inter-technology backscatter: Towards internet connectivity for implanted devices. In *Proceedings of the 2016 ACM SIGCOMM Conference*, SIGCOMM '16, pages 356–369, New York, NY, USA, 2016. ACM.

[72] V. Talla, M. Hessar, B. Kellogg, A. Najafi, J.R. Smith, and S. Gollakota. LoRa backscatter: Enabling the vision of ubiquitous connectivity. *Proceedings of the ACM Interactive, Mobile, Wearable, and Ubiquitous Technology (IMWUT) Conference*, 1(3):105:1–105:24, September 2017.

[73] D. E. Norgaard. The phase-shift method of single-sideband signal generation. *Proceedings of the IRE*, 44(12):1718–1735, Dec 1956.

[74] S. Gronemeyer and A. McBride. MSK and Offset QPSK modulation. *IEEE Transactions on Communications*, 24(8):809–820, Aug 1976.

[75] J. G. Proakis and M. Salehi. *Fundamentals of Communication Systems–2nd Ed.* Pearson, Essex, 2014.

[76] Bluetooth Special Interest Group. Bluetooth core specification v5.0, Dec 2016.

[77] David M. Pozar. *Microwave Engineering–4th Ed.* John Wiley & Sons, Inc., Hoboken, 2012.

[78] J. Kimionis, A. Bletsas, and J. N. Sahalos. Increased range bistatic scatter radio. *IEEE Transactions on Communications*, 62(3):1091–1104, Mar 2014.

[79] J. F. Ensworth, A. T. Hoang, T. Q. Phu, and M. S. Reynolds. Full-duplex Bluetooth Low Energy (BLE) compatible backscatter communication system for mobile devices. In *Proceedings of the 2017 IEEE Topical Conference on Wireless Sensors and Sensor Networks (WiSNet)*, pages 45–48, Jan 2017.

[80] J. Rosenthal and M. S. Reynolds. A dual-band shared-hardware 900 MHz 6.25 Mbps DQPSK and 2.4 GHz 1.0 Mbps Bluetooth Low Energy (BLE) backscatter uplink for wireless brain-computer interfaces. In *Proceedings of the 2020 IEEE International Conference on RFID*, pages 1–6, 2020.

[81] R. Correia and N. B. Carvalho. Dual-band high order modulation ambient backscatter. In *Proceedings of the 2018 IEEE/MTT-S International Microwave Symposium (IMS)*, pages 270–273, June 2018.

[82] J. T. Prothro, G. D. Durgin, and J. D. Griffin. The effects of a metal ground plane on RFID tag antennas. In *Proceedings of the 2006 IEEE Antennas and Propagation Society International Symposium*, pages 3241–3244, Jul 2006.

[83] M. P. Powell, W. R. Britz, J. S. Harper, and D. A. Borton. An engineered home environment for untethered data telemetry from nonhuman primates. *J. Neuroscience Methods*, 288:72 – 81, 2017.

[84] M. Ingram, M. Demirkol, and D. Kim. Transmit diversity and spatial multiplexing for RF links using modulated backscatter. In *Proceedings of the 2001 International Symposium on Signals, Systems, and Electronics*, pages 24–27, 08 2001.

[85] J. D. Griffin and G. D. Durgin. Gains for RF tags using multiple antennas. *IEEE Transactions on Antennas and Propagation*, 56(2):563–570, 2008.

[86] M. S. Trotter, C. R. Valenta, G. A. Koo, B. R. Marshall, and G. D. Durgin. Multi-antenna techniques for enabling passive RFID tags and sensors at microwave frequencies. In *Proceedings of the 2012 IEEE International Conference on RFID*, pages 1–7, 2012.

[87] M. Yin et al. Wireless neurosensor for full-spectrum electrophysiology recordings during free behavior. *Neuron*, 84(6):1170 – 1182, 2014.

[88] C. He, S. Chen, H. Luan, X. Chen, and Z. J. Wang. Monostatic MIMO backscatter communications. *IEEE Journal on Selected Areas in Communications*, 38(8):1896–1909, 2020.

[89] R. Serra, A. C. Marvin, F. Moglie, V. M. Primiani, A. Cozza, L. R. Arnaut, Y. Huang, M. O. Hatfield, M. Klingler, and F. Leferink. Reverberation chambers a la carte: An overview of the different mode-stirring techniques. *IEEE Electromagnetic Compatibility Magazine*, 6(1):63–78, 2017.

[90] E. Voges, T. Eisenburger, and D. Peier. Electrical mode stirring by reactively loaded antennas in reverberating chambers for EMC. In *Proceedings of the 2007 18th International Zurich Symposium on Electromagnetic Compatibility*, pages 465–468, 2007.

[91] Y. Liang, R. Long, Q. Zhang, J. Chen, H. V. Cheng, and H. Guo. Large intelligent surface/antennas (lisa): Making reflective radios smart. *Journal of Communication and Information Networks*, 4(2):40–50, 2019.

[92] W. Zhao, G. Wang, S. Atapattu, T. A. Tsiftsis, and X. Ma. Performance analysis of large intelligent surface aided backscatter communication systems. *IEEE Wireless Communications Letters*, 9(7):962–966, 2020.

[93] G. Vougioukas, A. Bletsas, and J. N. Sahalos. Instantaneous, zero-feedback fading mitigation with simple backscatter radio tags. *IEEE Journal on Radio Frequency Identification (RFID)*, pages 1–1, 2020.

[94] O. Yurduseven, S. D. Assimonis, and M. Matthaiou. Intelligent reflecting surfaces with spatial modulation: An electromagnetic perspective. *IEEE Open Journal of the Communications Society*, 1:1256–1266, 2020.

[95] V. Ranganathan, S. Gupta, J. Lester, J. R. Smith, and D. Tan. RF Bandaid: A fully-analog and passive wireless interface for wearable sensors. *Proceedings of the 2018 ACM Interactive and Mobile Wearable Ubiquitous Technology Conference*, 2(2), July 2018.

[96] R. Muller et al. A minimally invasive 64-channel wireless μECoG implant. *IEEE Journal of Solid-State Circuits*, 50(1):344–359, 2015.

[97] GS1. EPC compliant class-1 generation-2 UHF RFID devices conformance requirements. https://www.gs1.org/docs/epc/.

[98] M. S. Reynolds. A 2.4-GHz, hybrid 10-Mb/s BPSK backscatter and 1-Mb/s FSK Bluetooth TX with hardware reuse. *IEEE Microwave and Wireless Components Letters*, 27(12):1155–1157, Dec. 2017.

[99] A. Tang, Y. Kim, G. Virbila, and M. F. Chang. A 5.8 GHz 1.77mW AFSK-OFDM CMOS backscatter transmitter for low power IoT applications. In *Proceedings of the 2018 IEEE/MTT-S International Microwave Symposium (IMS)*, pages 259–261, June 2018.

[100] R. Correia and N. B. Carvalho. OFDM-like high order backscatter modulation. In *2018 IEEE MTT-S Internationa Microwave Workshop Series on 5G Hardware and Systems Technology (IMWS-5G)*, pages 1–3, Aug 2018.

[101] J. Rosenthal and M. S. Reynolds. All-digital single sideband (SSB) Bluetooth Low Energy (BLE) backscatter with an inductor-free, digitally-tuned capacitance modulator. In *Proceedings of the 2020 IEEE/MTT-S International Microwave Symposium (IMS)*, pages 468–471, Aug 2020.

[102] Analog Devices, Inc. ADG904 RF switch. https://www.analog.com/media/en/technical-documentation/data-sheets/ADG904.pdf (accessed July 20, 2020).

[103] Q. Zhang, A. B. J. Kokkeler, and G. J. M. Smit. An efficient FFT for OFDM based cognitive radio on a reconfigurable architecture. In *Proceedings of the 2007 IEEE Internationa Conference on Communications*, pages 6522–6526, 2007.

[104] L. Wang, X. Zhou, G. E. Sobelman, and R. Liu. Generic mixed-radix FFT pruning. *IEEE Signal Processing Letters*, 19(3):167–170, Jan. 2012.

[105] Lattice Semiconductor. iCE40 LP/HX/LM - low-power, high-performance FPGA. https://www.latticesemi.com/Products/FPGAandCPLD/iCE40 (accessed July 20, 2020).

[106] Lattice Semiconductor. MachXO2 flexible interface bridging FPGA. http://www.latticesemi.com/Products/FPGAandCPLD/MachXO (accessed July 20, 2020).

[107] Intel Corporation. NCO IP core - user guide. https://www.intel.com/content/dam/www/programmable/ (accessed July 20, 2020).

[108] Tiny FPGA. TinyFPGA BX boards. https://tinyfpga.com/ (accessed July 20, 2020).

[109] Peregrine Semiconductor. Digitally Tunable Capacitors. https://www.psemi.com/products/digitally-tunable-capacitors-dtc (accessed July 20, 2020).

VITA

James Rosenthal received the B.S. degree in Electrical Engineering from the University of Minnesota, Minneapolis, MN, USA in 2013 and the M.S. degree in Electrical Engineering from the University of Washington in 2018.

From 2013 to 2016 he was an electrical engineer at NASA Langley Research Center where he designed avionics systems for aerospace research projects. Since 2016 he has been a Ph.D. student in the Department of Electrical & Computer Engineering at University of Washington in Seattle, WA, USA. His research is focused on the design of ultra-low-power backscatter communication systems for biomedical applications.